Università degli Studi di Cassino e del Lazio Meridionale
Corso di Dottorato in Metodi, Modelli e Tecnologie per l'Ingegneria
Dipartimento di Ingegneria Elettrica e dell'Informazione



Resilience of the Italian electricity grid: objectives and future challenges

Giuseppe Berrettoni

giuseppe.berrettoni@unicas.it

In Partial Fulfillment of the Requirements for the Degree of
Philosophiae Doctor in
Electrical and Information Engineering

18/07/2024

TUTOR
Prof. Luigi Ferrigno

COORDINATOR
Prof. Fabrizio Marignetti

UNIVERSITÀ DEGLI STUDI DI CASSINO E DEL LAZIO MERIDIONALE

CORSO DI DOTTORATO IN METODI, MODELLI E TECNOLOGIE PER L'INGEGNERIA

Date: **18/07/2024**

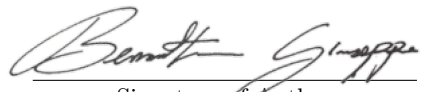
Author: **Giuseppe Berrettoni**

Title: **The Italian electricity grid of the future: objectives and challenges towards a modern and resilient grid**

Department: **Dipartimento di Ingegneria Elettrica e dell'Informazione**

Degree: **Philosophiae Doctor**

Permission is herewith granted to university to circulate and to have copied for non-commercial purposes, at its discretion, the above title upon the request of individuals or institutions.



Signature of Author

THE AUTHOR RESERVES OTHER PUBLICATION RIGHTS, AND NEITHER THE THESIS NOR EXTENSIVE EXTRACTS FROM IT MAY BE PRINTED OR OTHERWISE REPRODUCED WITHOUT THE AUTHOR'S WRITTEN PERMISSION.

THE AUTHOR ATTESTS THAT PERMISSION HAS BEEN OBTAINED FOR THE USE OF ANY COPYRIGHTED MATERIAL APPEARING IN THIS THESIS (OTHER THAN BRIEF EXCERPTS REQUIRING ONLY PROPER ACKNOWLEDGEMENT IN SCHOLARLY WRITING) AND THAT ALL SUCH USE IS CLEARLY ACKNOWLEDGED.

A mia madre, a mio padre, per esserci e sostenermi sempre,
sia quando la vita ti sorride che non.

Ad Ilaria, colonna portante della mia vita,
senza il quale questo traguardo sarebbe stato
ancor più arduo da raggiungere.

A me stesso, per tutti i sacrifici fatti
che mi hanno portato ad essere quello che sono.

"Non cercare di diventare una persona di successo,
tenta di diventare una persona di valore."
A.Einstein

Acknowledgements

For the research carried out on the electricity transmission grid, we thank Terna S.p.A. and RSE. In particular, part of the work developed by RSE was financed by the Research Fund for the Italian Electricity System within the framework of the Three-Year Research Plan 2022-2024 (DM MITE no. 337 of 15.09.2022), in accordance with the Decree of 16 April 2018."

For the research carried out on the electricity distribution network, we thank Tesmec Energy Automation. In particular, part of the work developed in collaboration with Tesmec was financed by the Lazio Region within the framework of the Operational Program of the Lazio Region European Social Fund Programming 2014-2020.

Contents

Acknowledgements **iv**

List of figures **viii**

List of tables **xi**

Acronyms **xiii**

1 Introduction **1**

2 Planning Resilience in the Electricity Transmission Grid **5**

2.1 New methodology for risk-based resilience assessment in the Italian power system 5

2.1.1 The proposed methodology 6

2.1.2 Climate maps 7

2.1.3 Vulnerability assessment 10

2.1.4 Evaluating the RP of the overall OHL 14

2.1.5 Validating the models 15

2.1.6 Efficient enumeration of multiple contingencies and power system response simulation 16

2.1.7 Case study 20

2.1.8 Conclusions 24

2.2 Tree interference mapping with LiDar for overhead lines 25

2.2.1 Availability of dataset for vegetation mapping in resilience assessment analyses . . . 26
2.2.2 The proposed advanced model for indirect effects of wind and wet snow . . . 29
2.2.3 Case study . . . 35
2.2.4 Conclusions . . . 36
2.3 Interphase spacers to increase power system resilience against wet snow . . . 37
2.3.1 The proposed model . . . 37
2.3.2 Case study . . . 44
2.3.3 Conclusions . . . 49

3 Operational Resilience in the Electricity Distribution Grid 50
3.1 Measurement problems in MV/LV cabin . . . 50
3.1.1 Rogowski coil . . . 51
3.1.2 Simulation setup . . . 57
3.1.3 Results . . . 62
3.1.4 Conclusions . . . 64
3.2 Impact of measurement uncertainty on distributed voltage control . 66
3.2.1 Distributed Online Voltage Control . . . 66
3.2.2 Simulation Setup . . . 68
3.2.3 Results . . . 72
3.2.4 Conclusions . . . 75

4 Resilience in Smart Utility Applications 76
4.1 Preliminary Sensitivity Analysis of Combinatorial Optimization (CO) for NILM Applications: Effect of the Meter Accuracy . . . 76
4.1.1 Notes on the problem of energy disaggregation . . . 77
4.1.2 Combinatorial optimization . . . 78
4.1.3 Simulation setup . . . 79
4.1.4 Results . . . 82

4.1.5 Conclusions 86
4.2 eLAMI - An Innovative Simulated Dataset of Electrical Loads for Advanced Smart Energy Applications 87
4.2.1 Available electrical energy dataset 88
4.2.2 Design of dataset generation 92
4.2.3 Results 101
4.2.4 Conclusions 111

Conclusions and future developments **112**

Bibliography **114**

List of Figures

1.1 Examples of resilience problems in the electricity grid 4

2.1 Architecture of the resilience assessment methodology 7
2.2 (a) Forecast maps to 2030, with 4x4km resolution, for wind, considering different thresholds of probability of exceeding the expected wind speed from 40 km/h to 140 km/h. (b) Forecast maps to 2030, with 4x4km resolution, for snow, considering different thresholds of probability of exceeding the expected sleeve load from 1kg/m to 18 kg/m. 9
2.3 Scheme of wind and snow induced forces on OHL and interfering vegetation 13
2.4 (a) Top view of the LiDar survey reconstruction. In red the parts that are critical. (b) View of the conductor section. In red the vegetation to be cut. 14
2.5 One line diagram of the portion of the grid vulnerable to weather events. The black arrows represent the connections to the rest of the HV grid 21
2.6 Example of overlapping between CORINE DB tree coverage maps and the route of two lines 27
2.7 Analysis of vegetation type on two Italian regions with CORINE DB 27
2.8 LiDar mapping of tree interference around the line route 28
2.9 (a) Overlap between CORINE tree coverage map and line route. (b) LiDar information about actual interfering cells along the line routes 36
2.10 Installation of IS devices on a triple of phase conductors 39
2.11 Scheme of the forces acting on a single interphase spacer 42
2.12 Maximum number of IS devices allowable over the spans of the three OHLs under test 46
2.13 Comparison of failure RPs for the spans before (x axis) and after (y-axis) of the deployment of IS devices 47

2.14 Number of AT devices installable on the spans of line 3 according to the VULLINE model 48
2.15 Comparison of maximum jump heights of the lowest phase after wet snow sleeve shedding on the spans of line 1, at 6 kg/m 49

3.1 Example of RC with operational amplifier 52
3.2 Equivalent circuit of an RC integrator using a single turn 53
3.3 (a) Operational Amplifier. (b) Frequency Characteristic 54
3.4 Schematic diagram of a RC with digital integration 55
3.5 Recursive filter of T-PMR 56
3.6 Position of primary conductor according to position factor PF 58
3.7 Measurement setup block diagram 58
3.8 Block diagram of signal processing 61
3.9 Harmonic coefficient for RC under test at PF0 65
3.10 Structure of the CPS system 67
3.11 Activation of the new *Client* 68
3.12 Simulation grid 69
3.13 PV Active Power Generation 69
3.14 Absorption Profile of the Electrical Load at Node 6 70
3.15 Total Reactive Power at each PMUs accuracy level 73
3.16 Total Reactive Power at each fps 73
3.17 Reactive Power (node 6) at each accuracy level 74
3.18 Reactive Power (node 6) at each fps 74

4.1 CO Flow chart 79
4.2 Dataset Structure 81
4.3 Multi–class Classification Accuracy in case of 3 loads to disaggregate 83
4.4 Multi–class Classification Accuracy in case of 5 loads to disaggregate 83
4.5 Multi–class Classification Accuracy in case of 7 loads to disagregate 84
4.6 Binary Classification Accuracy in case of 3 loads to disaggregate . . 84
4.7 Binary Classification Accuracy in case of 5 loads to disaggregate . . 85
4.8 Binary Classification Accuracy in case of 7 loads to disaggregate . . 85
4.9 House scheme and electrical loads distribution. The blue zone represents the *"Partial 1"* with 7 electric loads; the pink zone represents the *"Partial 2"* with 10 electric loads; the green zone represents the *"Partial 3"* with 19 electric loads 96
4.10 Block diagram of data acquisition setup 96
4.11 Emulated Voltage profiles with load and without load 98
4.12 Percentage harmonic coefficients normalized with respect to the fundamental frequency 98

4.13 Block diagram of the simulator composed of three sections: Input, Processing and Output 99
4.14 Saving eLAMI structure 102
4.15 Comparison between WT3000 and eLAMI for devices: *Fan*, *Fan Heater*, *Smart TV* and *Aggregate*. Comparison made in terms of features: (a) Voltage RMS (b) Current RMS (c) Active Power (d) Apparent Power 103
4.16 Average monthly active energy consumption profiles of the aggregate load 105
4.17 Aggregate active energy load curve per months 106
4.18 Seasonality example of some different electrical loads 107
4.19 Example of load profiling application for desk lamp - (a) Power consumption per state (b) Active power as a function of power factor at 50 Hz (c) Phase of 5th voltage harmonic group as a function of active power (d) Phase of 5th voltage harmonic group as a function of power factor at 50 Hz 108
4.20 Active power in time: (a) Aggregate (b) Single Loads 109
4.21 Current harmonics of 6th group in time: (a) Aggregate (b) Single Loads 109
4.22 Example of forecasting for electric consumption with eLAMI 110

List of Tables

2.1 Event table for lines L1 and L2 17
2.2 The correlation sub-matrix corresponding to the set of lines L1, L2, L3, L4 22
2.3 Loads at primary substations in an average loading condition of the grid 22
2.4 Return Period of the four lines of the case study 22
2.5 List of analyzed contingencies for increasing RP values 23
2.6 Contributions of contingencies affecting PS1 substation to annual EENS 23
2.7 Values of distances for deferrable and urgent criticality 29
2.8 Comparison of the line failure RP's for vegetation interference between original model (using exclusively CORINE DB) and the advanced vulnerability model integrating LiDar map 35
2.9 List of described simulation cases 44
2.10 Failure RPs for the OHLs set without IS application 45
2.11 Failure RPs for the OHLs set with IS application 46

3.1 Error limits for RC 57
3.2 Test currents and multiples 59
3.3 Percentage harmonic coefficients for distorted current 60
3.4 Percentage amplitude error limits for accuracy levels expressed by the standard 62
3.5 Percentage amplitude errors for sinusoidal current as a function of: position, integration technique and current level 63
3.6 Percentage amplitude errors for distorted current as a function of: position, integration technique and current level 64
3.7 THD for distorted current as a function of: position, integration technique and current level 64
3.8 Electrical Parameters of the Simulated Grid 69

3.9 Main Features of Some Commercial PMUs 70
3.10 Simulation Parameters 71

4.1 Loads electrical signature 80
4.2 Loads electrical signature 80
4.3 Main characteristics of some public dataset based on real data . . . 89
4.4 Main characteristics of some public dataset based on simulated data 91
4.5 Electrical loads specifications. Returns the appliance identifier (ID), the name of the loads (Appliance), the number of states tested (N_S) and and the maximum active power that each load can absorb (P_{Nom}) 95
4.6 Comparison of some characteristics of the voltages: Acquired Main Voltage, Emulated Voltage With Load and Emulated Voltage Without Load 97
4.7 Sampling characteristics used for the acquisition of electrical load profiles 99
4.8 Comparison of mean and standard deviation values obtained from WT3000 and eLAMI for the electrical load *Fan*. Considered features: V_{rms}, I_{rms}, P and S 104

Acronyms

Acc_V	Voltage Accuracy.
ARERA	Autorità per la Regolamentazione per l'Energia, Reti e Ambiente.
AT	Antitorsional.
C	Probability of the Copula.
CBA	Cost Benefit Analysis.
CCDF	Complementary Cumulative Distribution Function.
CDF	Cumulative Distribution Function.
CEI	Italian Electrotechnical Committee.
CESM-LENS	Community Earth System Model - Large Ensemble Project.
CO	Combinatorial Optimization.
CORINE	COoRdination of Information on the Environment.
CPS	Cyber-Physical System.
DB	Database.
DG	Distribution Generation.
DMS	Distribution Management Systems.
DMU	Data Management.
DSSE	Distribution System State Estimation.
EENS	Expected Energy Not Served.
$EENS_h$	Expected Energy Not Served of a generic *h-th* contingency.
$EENS_{ps,post}$	Expected Energy Not Served Post-Intervention.
$EENS_{ps,pre}$	Expected Energy Not Served Pre-Intervention.
EHV	Italian Extra High Voltage.

eLAMI	electrical Loads Acquisition for Monitoring Instruments.
FHMM	Factorial Hidden Markov Model.
FN	False Negative.
FP	False Positive.
fps	Reporting rate.
GIS	Geographical Information System.
GSP	Graph Signal Processing.
HMM	Hidden Markov Model.
HS	High-Stemmed.
HTTP	HyperText Transfer Protocol.
HV	High Voltage.
I	Current.
I_1	Fundamental value of the current.
I_h	Value of the h-th harmonic of the current.
I_{pr}	Test current.
IEC	International Electrotechnical Commission.
IS	Interphase Spacers.
ISPRA	Superior Institute for Environmental Protection and Research.
LiDar	Light Detection and Ranging.
LS	Low-Stemmed.
MERIDA	MEteorological Reanalysis Italian DAtaset.
MOO	Multi-Objective Optimization.
MQTT	Message Queuing Telemetry Transport.
MV	Medium Voltage.
NILM	Non Intrusive Load Monitoring.
NTG	National Transmission Grid.
OHL	Over Head Lines.
p.u.	Per Unit.
P_{GEN}	Power Generation.
PMU	Phasor Measurements Units.
PS	Primary Substation.
PV	Photovoltaic Panel.

Q	Reactive Power.
R	Linear Correlation Matrix.
R	Resistance.
RC	Rogowski Coil.
ROW	Right of Way.
RP	Return Period.
RP_{post}	Return Period Post-Intervention.
RP_{pre}	Return Period Pre-Intervention.
$RP_{ps,post}$	Return Period of Primary Substation Post-Intervention.
$RP_{ps,pre}$	Return Period of Primary Substation Pre-Intervention.
RSE	Ricerca Sistema Energetico.
RTS	Rated Tensile Strength.
THD	Total Harmonic Distortion.
TN	True Negative.
TP	True Positive.
TSO	Transmission System Operator.
VAr	VoltAmpere reactive.
VULLINE	Vulnerability assessment tool.
X	Reactance.

Chapter 1

Introduction

The activity conducted in the period from 15/03/2022 to 15/03/2024 was carried out in collaboration between the University of Cassino and Lazio Meridionale, Tesmec Energy Automation and Terna S.p.A. In particular, studies were conducted on the resilience of the Italian electricity grid of the future, in terms of objectives and challenges, both for operational resilience (short-term) and planning resilience (long-term).

Climate change has been on going since the end of the 1800s, the average temperature on Earth has increased by 1.1 ° C since the end of the 1800s. Increased climate-altering emissions make this more likely:

- greater variability of future temperatures;
- an increase in severe phenomena.

In order to be able to combat climate change, the national electricity grid, and grids around the world, are undergoing a major change due to the large presence of renewable resources and new electrical loads such as charging stations for electric vehicles, heat pumps, etc. The combination of these new resources and electrical loads is called Distribution Generation (DG). This evolution has led to the definition of the distribution network as a smart grid. The smart grid is a combination of computer networks and electricity distribution networks. It is called 'smart' because it optimises the distribution of electricity, decentralises power plants and minimises overloads and voltage fluctuations. Thus, we move from a system of large power plants to a green economy and renewable energy sources. One of the fundamental pillars of smart grids is electricity grid resilience. Electricity grid resilience, as defined by CIGRE WG C4.47, refers to the ability of an electrical system to limit the magnitude, severity and duration of its degradation. Specifically, resilience is

the ability of a system to absorb and withstand stresses that exceed the resilience limits of the system itself and to return to its normal operating state, quickly and efficiently, possibly through temporary interventions, including the preservation, restoration or improvement of essential system structures and functions. Some examples of issues that the evolution of the electricity grid is facing, in order to become increasingly resilient, are shown in Figure 1.1, where a distinction is made between issues related to the operational resilience of the grid (for example voltage stability and diagnostics) and others related to planning resilience (i.e. perspective maps for high wind or snow and hydrogelogical hazards).

In order to be able to increase network resilience, it is important to gather adequate information from the field that reflects the true state of the electricity grid. The information gathered from the field, however, can often be affected by measurement errors, which can mislead the end user. For this reason, in the initial phase of this study, measurement problems in the MV/LV cabin were addressed. This measurement is carried out using Rogowski coils, very ductile, inexpensive and easy-to-use current sensors, which, however, do not have a high measurement resolution and their measurements can often be affected by errors related to their installation or by adjacent magnetic fields that interfere with the main magnetic field to be measured. In particular, the Rogowski coil prototypes, owned by Tesmec, were tested through the use of a measuring instrument that is the T-PMR, also owned by Tesmec and found in most MV/LV transformer substations.

The increasing presence of DG within the electricity grid means that voltage quality, understood as the maintenance of technical parameters characterising voltages within defined limits, may suffer. This is due to the fact that the gradual decrease of conventional generation plants in the grid leads to a significant decrease in short-circuit power. This condition leads to:

- increased extension of the areas affected by the voltage reduction resulting from a short circuit;
- less fault selectivity by the protection systems;
- reduction in the ability to attenuate harmonic voltage distortion.

In this case too, as seen for current measurements, it is crucial to have a measurement that is as accurate as possible. For this reason, between 01/10/2022 and 15/02/2023, studies were carried out at the E-ON Research Centre of the RWTH in Aachen, Germany, on the impact of the measurement error of the phasor units on the distributed control of online voltage. One of the possible future developments of this research, therefore, is to increase the number of measurements used in the

network, also using those of the T-PMR, a device already present in the cabin and which would save on the number of PMUs installed in the network.

Resilience is evaluated not only on the transmission and distribution grid, but also on the user side. For example, an industrial plant aims to have an automated network of production devices that is as resilient as possible. For this reason, predictive maintenance and load disaggregation techniques have been investigated during the period from 15/03/2021 to 01/10/2022, which can increase the resilience of a household or industrial plant and also reduce the costs associated with the installation of smart meters. In particular, load disaggregation by means of non-intrusive load monitoring (NILM) allows artificial intelligence algorithms to derive the electrical behaviour of a load from the aggregated data of all the electrical loads in a household, from which it is possible to make diagnoses on the health of these loads. To this end, the accuracy of an optimal combinatorial disaggregation technique was studied, which aims to understand how the algorithm behaves as the type of electrical characteristic analysed, the number of loads to be disaggregated and the accuracy of the meters vary. However, given the scarcity of household electrical datasets in the literature that take into account different types of electrical characteristics, a simulated dataset of electrical loads was created from real electrical profiles. Specifically, it consists of 36 different electrical loads and a complete electrical load signature, which can be used for various applications in the field of smart energy to test and improve artificial intelligence algorithms useful for predictive diagnostics.

Climate change is increasingly becoming a threat to the world, with serious consequences that can also be caused to the electricity transmission system, a key infrastructure for modern society. The main objective of TSOs is to make the grid increasingly resilient to such phenomena. The main critical weather threats include wet snow, strong winds and hydrogeological phenomena, i.e. floods and landslides due to high levels of precipitation. For this reason, during the period between 01/03/2023 and 15/03/2024, the research carried out focused on issues related to grid resilience in the face of climate change, thanks to the work done with Terna S.p.A.

The following thesis was structured following a top-down electrical approach, i.e. starting at the highest voltage level where planning resilience will be analysed, and then moving on to the MV/LV distribution level, where operational resilience will be addressed. In particular, in Chapter 2 the electrical HV grid resilience to climate change will be addressed. The new methodology for risk-based resilience assessment in the Italian power system is described in Chapter 2.1, the tree interference mapping for overhead lines is described in Chapter 2.2 and finally a interphase spacers to increase power system resilience against wet snow is described in Chapter

2.3. The Chapter 3 refers to the electrical distribution network, in which Chapter 3.1 analyses the measurement problems that exist in MV/LV transformer cabin and Chapter 3.2 analyses the impact that measurement error has on distributed voltage control. Finally, in Chapter 4 are discussed some short-term resilience for diagnosis application, such as Combinatorial Optimization technique for NILM in Chapter 4.1 and a new simulated dataset of electrical loads in Chapter 4.2.



Figure 1.1: Examples of resilience problems in the electricity grid

Chapter 2

Planning Resilience in the Electricity Transmission Grid

2.1 New methodology for risk-based resilience assessment in the Italian power system

The climate change underway means that extreme atmospheric phenomena and the consequent risk of damage to the infrastructure dedicated to the transport of electricity are increasingly frequent. For this reason, the challenges facing Transmission System Operator (TSO) related to climate change are increasingly urgent and entail two objectives:

- to assess the risk of multiple employee disruptions;
- to develop preventive or corrective countermeasures aimed at absorbing the effects of destructive events and rapid recovery, i.e. an increase in the resilience of the system [1].

The adaptation of the decision-making process at every level will be fundamental, in terms of resilience both in the operational and planning phases, reviewing analyses, methodologies, thus assessing the risk and comparing it with an acceptable threshold [2]. In the planning process, the transition from an *N-1* security criterion towards an *N-1* criterion, thus including the analysis of multiple contingencies and the evaluation of potential cascading effects, represents an innovative approach to adequately evaluate the level of resilience of the electricity system in the

event of extreme weather events. In order to plan future interventions to increase grid resilience, a risk-based methodology was developed through the collaboration between Terna and Ricerca Sistema Energetico (RSE). The methodology is aimed at using prospective climate scenarios, to be scalable and replicable and to be used to analyse multiple weather threats. At present the methodology has been applied for the phenomena of strong wind and ice-snow threats which represent the two major causes of load disruptions in the Italian system. Moreover, the methodology also makes it possible to assess, on a quantitative and objective basis, the investments that can lead to an increase in the resilience of the electricity grid, quantifying the technical benefits such as the reduction of:

- probability of power asset outage;
- risk indicators such as Expected Energy Not Served (EENS) [3];

2.1.1 The proposed methodology

The methodology for resilience assessment of the electrical transmission grid in Italy is developed by TERNA and RSE [3] and it can be applied to both wind and ice/snow threats, on the entire Italian electricity transmission grid. It is composed by 8 main steps:

1. Calculate the probability of occurrence of meteorological phenomena in the future, as a function of predefined intensity thresholds, using a climatological model;
2. Quantify the vulnerability of the grid components as a function of the intensity of the meteorological event considered, through the development of vulnerability curves applied to a georeferenced grid model;
3. Combine the probabilistic model of the weather event (derived from1) with the vulnerability curve (derived from 2) of the grid components, specifically lines, which leads to the Return Period (RP) of the outages of the components in Return Period Pre-Intervention (RP_{pre}) i.e. in the initial grid conditions;
4. Determine the $RP_{ps,pre}$ of the outages of the Primary Substation (PS) and the corresponding value of Expected Energy Not Served Pre-Intervention ($EENS_{ps,pre}$) by applying a cascading outage simulator;
5. Identify possible interventions aimed at increasing resilience, based on the meteorological phenomena under analysis, the characteristics of the reference area, and the relevant lines, with reference to the critical PS in terms of outage RP and of load disruptions;

6. Evaluate the impact of the interventions identified in the previous step 5, measured in terms of increase in the RP of the lines Return Period Post-Intervention (RP_{post}) with respect to the previous value RP_{pre};

7. Determine Return Period of Primary Substation Post-Intervention ($RP_{ps,post}$) of the PS and the corresponding value of Expected Energy Not Served Post-Intervention ($EENS_{ps,post}$) assuming that the interventions have been implemented, by applying a cascading outage simulator;

8. Calculate the resilience benefit associated with each identified intervention and perform the relevant economic evaluation. Currently the Cost Benefit Analysis (CBA) of the TSO is based on the economic valorization of EENS reduction, which is used to quantify the benefit of a specific intervention on the grid.

The presented methodology has been approved by Autorità per la Regolamentazione per l'Energia, Reti e Ambiente (ARERA) [4], and is now part of Terna Grid code. Figure 2.1 shows a flow chart that summarizes the main phases of the methodology.

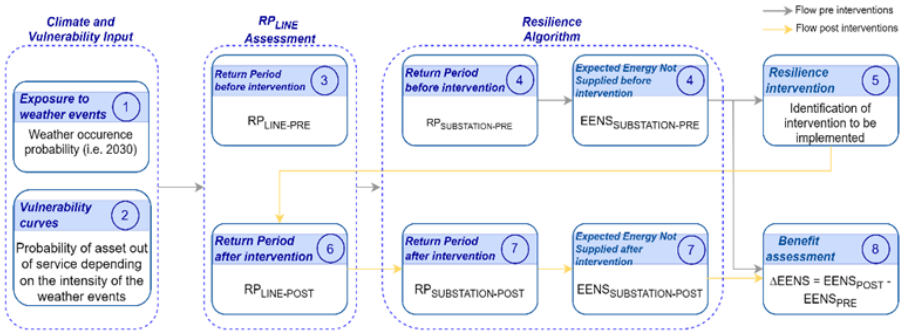


Figure 2.1: Architecture of the resilience assessment methodology

2.1.2 Climate maps

In the first step of the methodology, as reported in 2.1.1 climate models [5] [6] [7] are used to identify the exposure of the National Transmission Grid (NTG) to severe weather events expected in the coming decades. Climate scenarios allow estimating future climate hazard at different levels of detail, calculating the probability that a phenomenon of a given intensity will occur in each area, over a certain period

of time. The climate projections are reproduced over the entire national territory with 4km x 4km resolution which not only provide an overview of the expected evolution of the weather hazards, but also allow quantifying the risk to the NTG. This risk is evaluated by identifying its infrastructures with the highest probability of exposure to future severe weather events. Climate projections are determined for different time horizons, up to 2050 at 5-year intervals for wind and 10-year intervals for snow, as the annual probability of exceeding specific intensity thresholds of the considered weather threat.

The development of climate models involves four main steps:

1. Declining global historical climate data on a local scale: starting from model reconstructions of past climate, it is possible to "downscale" to the national level, obtaining local climate features with higher resolution. In the case of wind, 40 realizations of theCommunity Earth System Model - Large Ensemble Project (CESM-LENS) climate model [6] were used; in the case of the ice-snow phenomenon, Euro-CORDEX climate models [7] were used with the subsequent application of the Makkonen model for the estimation of the wet-snow sleeve phenomenon;

2. Bias correction: down scaled historical data require "bias-correction" where necessary to avoid systematic errors of underestimation or systematic overestimation of exposure thresholds. This correction is performed through data recorded at local weather stations or using meteorological reanalysis datasets. The correction of systematic model errors (e.g., over/underestimation with respect to observed local conditions) was made based on the provider's data availability: as far as wind is concerned, the correction was made through the ERA-5 database [5], while in case of the ice-snow threat the MEteorological Reanalysis Italian DAtaset (MERIDA) Optimal Interpolation [8] reanalysis dataset was used;

3. Processing of high-resolution climate projections: the results of climate models thus corrected are used to process future projections, re scaled to 4km x 4km resolution for each region of interest and for selected future periods;

4. Calculation of the characteristic parameters of the expected weather event analysed: from the results of the down scaled and bias-corrected climate models, the probabilities of exceeding the threshold values of the stress variable at given future horizons are obtained, as shown in Figure 2.2.

The verification of such climatological models poses significant challenges to the researchers in the field: the verification has consisted in comparing the values of some quantities recorded in recent events (e.g. sleeve thickness) with the

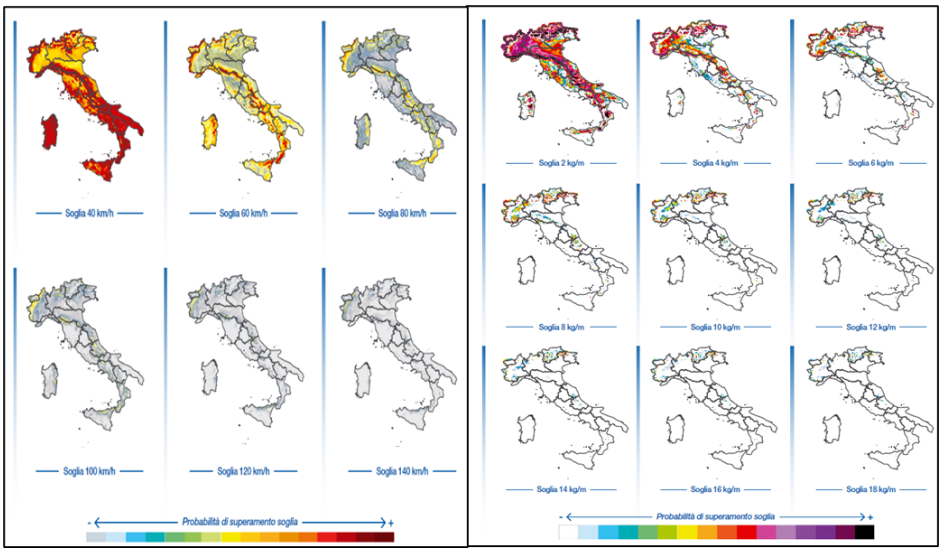


Figure 2.2: (a) Forecast maps to 2030, with 4x4km resolution, for wind, considering different thresholds of probability of exceeding the expected wind speed from 40 km/h to 140 km/h. (b) Forecast maps to 2030, with 4x4km resolution, for snow, considering different thresholds of probability of exceeding the expected sleeve load from 1kg/m to 18 kg/m.

values of the same quantities evaluated in the scenarios developed by climatological models. To estimate the exposure of the NTG with respect to the considered event, the results of climate projections are associated with the NTG, using the geo-referenced NTG asset map, so as to deduce, for each line and each span under analysis, the probability values of exceeding the intensity thresholds for the analysed threat in the identified horizon year. The adoption of climatological models allows to assess the effect of global warming on the trend of the main characteristics (severity and probability of occurrence) of weather events over the decades, also accounting for different emission scenario hypotheses. Starting from multiple thresholds of weather threat (snow or wind) intensity, the Complementary Cumulative Distribution Function (CCDF) and Cumulative Distribution Function (CDF) are calculated: these distributions combined with asset vulnerability models allow to calculate the failure return periods for Over Head Lines (OHL), as described in the sequel.

2.1.3 Vulnerability assessment

This section discusses the model proposed to quantify the vulnerability of OHLs to wet snow and wind threats. These models are characterised using real orographic and technical parameters of the NTG assets provided by the Italian TSO.

Vulnerability models of OHL spans against direct effects of wind and snow

The proposed approach, starting from CEI EN 50341-1 standard [9], expresses the vulnerability models as probabilities of component damage, in turn depending on two weather variables namely:

- wind speed [km/h] (w), evaluated as the average value over 10 minutes at 10 m height from the ground;
- wet snow linear mass [kg/m] (q) on reference conductors (22.8 mm and 31.5 mm diameters cover the large majority of existing conductors in the Italian transmission grid).

In particular, the model expresses the vulnerability of each span sub-component as a function of the actions due to strong wind and snow loads. In fact, each weather variable (w and q) is converted into specific actions that the wind and snow apply to the different sub-components of the OHL. Specific mechanical actions are associated with the above mentioned sub-components:

- tension on individual phase conductor (T_{pc} *[kN]*);
- tension on individual shield wire (T_{sw} *[kN]*);
- resulting forces acting on the tower (R_t *[kN]*), derived by combining the vertical loads (due to the weight of the conductors and of potential wet snow/ice sleeves on contiguous spans, as well as to the altimeter coefficient k for the specific tower) and the horizontal ones (due to wind pressure on conductors, tower structure, shield wires, insulators/support, and to line deviation angle δ)
- stress variable for the tower foundations, consisting either in the overturning moment of the tower (M_t *[kNm]*) in case of unique block foundations, or in the compression action on the ground [N/m2] for foundations with separate footings.

The vulnerability curves of the *i-th* sub-components (PV_i) to direct action is given in Equation 2.1.

$$PV_{\mathrm{i}}(w, q) = PV_{\mathrm{i}}(A_{\mathrm{i}}, \Theta_{\mathrm{i}}) \tag{2.1}$$

where:

- A_i = *G(r)*, expressed in terms of the two weather variables in vector r=(w, q);
- Θ_i (Parameters which characterizes the vulnerability of sub-component *i-th* to combined wind and snow actions).

Parameters Θ_i are given by the expected values of:

- Rated Tensile Strength (RTS) for phase conductors;
- Rated Tensile Strength (RTS) for shield wires;
- Breaking strength of supports [kN];
- Maximum overturning moment [kNm] or maximum compression of the ground [daN/cm2], according to the type of foundations and to the typical design criteria.

Functions PV_i of the sub-components of each individual line span represent the fragility curves of the sub-components to the above mentioned actions. These functions are given by log normal distributions of the action variables. To identify the parameters (mainly the maximum breaking strength) characterizing the vulnerability curves of the support, the following sources are exploited:

- the design criteria reported in Italian Electrotechnical Committee (CEI) 11.4 standard [10];
- the mechanical utilization curves of the towers: these are piecewise linear curves [*Cm*,δ] and [*Cm*, *K*] planes, where: *Cm* is the average value of the lengths of the two adjacent spans, *K* is the altimetric coefficient, and δ is the deviation angle of the line in correspondence of the specific mean span length *Cm*.

Once the vulnerability model of each sub-component i is available, then the vulnerability of each line span (PV_{span}) can be expressed as in Equation 2.2 because the failure of any sub-component of the span is assumed to cause the outage of the entire span.

$$PV_{\text{span}}(w, q) = 1 - \prod_i [1 - PV_{\text{i}}(w, q)] \tag{2.2}$$

The detailed equations of the forces acting on each sub-components (conductors, supports, shield wires, foundations, etc.) are reported in [11].

Vulnerability models of OHL spans against indirect effects of wind and snow: base model

This subsection describes the model developed to quantify the vulnerability of OHL spans against indirect effects of wind and snow (i.e. the potential interference due to vegetation along the OHL route).

The contact with trees is a frequent cause of failures in Medium Voltage (MV) and High Voltage (HV) grids, due to strong wind or snow. An analytical probabilistic model of the interactions between the line and the interfering vegetation in presence of wind and snow has been proposed by the authors in [12] and it accounts for:

- vertical contact due to trees in the Right of Way (ROW) (an unlikely event because the Italian TSO fulfils the prescriptions of CEI 11-4 [9]);
- lateral contact due to fall of trees from outside the ROW;
- lateral contact between the line catenary (inclined with respect to the vertical axis) and the trees at theROW boundaries (unlikely event, due to the strict prescriptions of the Italian standard CEI 11-4 [9]).

The main factors considered are: tree linear coverage density (no. of trees per km), clearance distance (horizontal distance between tree line and the closest phase conductor), tree species (trunk height, coniferous or broad leaf, maximum breaking strength, root-soil system features), orography (terrain slope), weather conditions (wind, snow, ice etc.).

The tree characteristics (mechanical properties e.g. the Young's modulus, the modulus of rupture, etc.) and the weather conditions affecting line sag (solar irradiation, wind speed) are treated as stochastic variables. Figure 3 indicates the scheme of wind and snow induced forces in the interaction tree-Over Head Lines (OHL). The main cause of tree fall is the strong wind, which applies a lateral force that can cause tree stem bending and rotation of the root system: this can increase the component of the overturning moment due to the vertical forces to which the snow load contributes. In the following, the analytical model described in [12] is extended to consider the effects of wet snow on the interaction between vegetation and lines.

The proposed vulnerability model is physics inspired and all the forces represented in Figure 2.3 (weights, wind and snow induced forces) are computed taking into account the above mentioned factors. More details on the model are reported in [11].

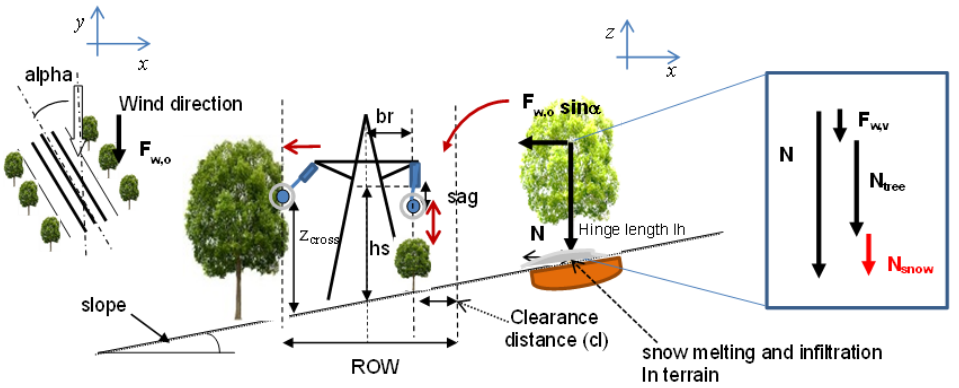


Figure 2.3: Scheme of wind and snow induced forces on OHL and interfering vegetation

Vulnerability models of OHL spans against indirect effects of wind and snow: advanced model

The base vulnerability model illustrated in the previous subsection employs the CORINE Land Cover database [13] to map the vegetation across Italy. Nonetheless, this database only provides average values for tree characteristics and does not offer precise insights into specific tree interference conditions along the OHL ROW. To address this limitation, an advanced vulnerability model has been defined to integrate the vegetation mapping based on Light Detection and Ranging (LiDar) systems [14] which are more accurate and updated compared to the CORINE approach. Terna employs its fleet of helicopters to conduct terrain mapping around the lines using LiDar, a remote sensing system that allows to measure the distance of an object or surface from power lines using a laser pulse. The primary goal of inspections is to accurately measure the actual distance between power lines and surrounding vegetation. This allows mapping potential tree interferences and planning preventive cutting actions. The LiDar mapping covers a 50-meter width on each side of the line, with spatial resolution up to 1 m x 1 m. This mapping provides an accurate reconstruction of orography, of the presence and height of vegetation along the lines (see Figure 2.4). This information is updated annually

through new surveys.

Within the data provided by LiDAR systems, the advanced model for OHL vulnerability to tree interference requires information about potential interactions between a cylindroid centred on the catenary of the wires (including conductors and shield wires) and potentially interference vegetation. These interactions are assessed both within and beyond the ROW, within each 1 m $\times$ 1 m cell along the path of each line span. Additional details are outlined in Chapter 2.2.

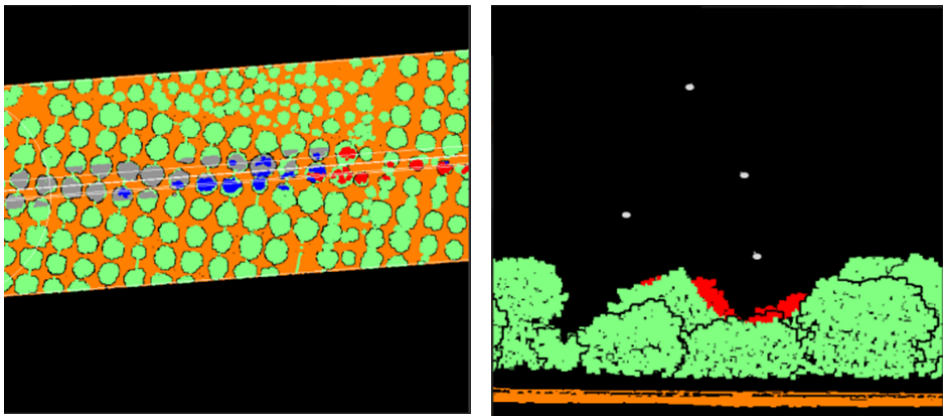


Figure 2.4: (a) Top view of the LiDar survey reconstruction. In red the parts that are critical. (b) View of the conductor section. In red the vegetation to be cut.

2.1.4 Evaluating the RP of the overall OHL

The evaluation of the RP of substation outages starts from the assessment of the failure RP of the lines which directly or indirectly connect the substation to the rest of the HV grid. The proposed resilience assessment methodology evaluates the return periods of the overhead line outages starting from the map of extreme values of the stress variables (snow loads and wind speeds) over different time horizons provided by climatological models [5] [15] as well as from the vulnerability models of the individual OHL spans. More specifically, the combination of the vulnerability curves of each OHL span against both direct and indirect effects of wind and snow with the known RP for specific values of the threat actions (e.g. wind and snow loads) allows to compute the RP of the outage of each OHL span due to direct and indirect effects of snow and wind. The flexibility of the modelling approach allows to separately consider the effects of wind and wet snow, thus computing two

separate RPs for each OHL span.

After that, given the indications of Std. International Electrotechnical Commission (IEC) 60826 [16] about the extension of the weather events, the line is divided into groups of N spans which are assumed to be simultaneously struck by the threat. The RP of each group is the minimum RP of the spans composing the group, while the RP of the line is obtained by computing the probability of the logical "OR" of the failure probabilities of each group.

2.1.5 Validating the models

The validation process aims to verify whether the outputs of the entire methodology align with statistics related to OHL outages caused by extreme weather events, as derived from the actual operation of the power grid. Specifically, the areas subject to validation are the OHL vulnerability models and the climatological models, especially concerning one of the major threats affecting the Italian Extra High Voltage (EHV) grid, which is wet snow. The validation process involves a comprehensive analysis of historical failure events that have occurred over the most recent 16-year observation period. From the complete failure database, the validation process selects only failures linked to direct or indirect impacts of a threat (such as wet snow) on the OHL components. Apart from ensuring the accuracy, completeness, and comprehensiveness of the available historical failure information related to OHLs, it is crucial to consider the history of infrastructure upgrades performed on these lines in recent years. Such upgrades lead to changes in vulnerability model parameters. Therefore, older failures might be due to higher vulnerability compared to what the methodology framework reconstructs based on the most current OHL parameters available in Terna databases. Hence, in the validation process, it is vital to filter out the lines whose behaviour with respect to the studied meteorological threat, evaluated using the methodology vs reconstructed through historical failure records presents a discrepancy resulting from infrastructure changes implemented during the observation period. For validation purposes, the benchmark comprises OHL failures caused by wet snow and documented during the observation period. The second comparison term consists of calculated outage return periods, which result from combining the OHL vulnerability model with a source of climatological or meteorological data, depending on the context of application. As the benchmark pertains to past failure events, the mentioned data source is based on the best available meteorological data, specifically the outcomes of the RSE meteorological reanalysis MERIDA-OI [8] with optimal interpolation of observed values. Consequently, the validation process of the vulnerability model is divided into two steps:

1. Validation of the meteorological dataset against real wet snow events;
2. Validation of the calculated OHL outage return periods against empirical failure data.

The initial step is applied to recent and significant snowfall events that caused notable electrical disruptions. It involves comparing the wet snow loads recorded during these events with those reconstructed using the MEteorological Reanalysis Italian DAtaset (MERIDA) dataset applied to the Makkonen accretion model. The subsequent validation step involves comparing the statistics related to outage return periods calculated by the methodology with the corresponding statistics related to actual outages recorded in the grid. Given the limited number of recorded OHL failure events within the available observation interval (approximately 16 years), the high number and the significant differences characterising the lines under analysis (the whole NTG), the comparison between calculated and empirical outage return periods is conducted on clusters of lines grouped based on specific physical quantities. Creating line clusters allows identifying a sufficient number of failure events in each cluster, ensuring that the uncertainty regarding the empirical mean number of failures for the lines within each cluster remains adequately constrained. The selection of physical dimensions is based on engineering judgment, involving the identification of physical parameters believed to significantly affect the outage return periods of OHLs for each specific threat. Particularly, concerning the wet snow threat, the physical quantities used for clustering are:

- length of the line, to point out that longer lines have higher exposure to wet snow;
- maximum altitude of OHL spans, to take into account that higher altitude leads to greater exposure to wet snow events;
- voltage level, to consider that design characteristics affected by voltage levels strongly impact OHL response to wet snow loads.

The results obtained show that the clustering carried out allowed the lines to be grouped according to significant dimensions for which a very good matching is achieved with respect to the historical failure history: this permitted to successfully pass the validation. More detailed are reported in [3].

2.1.6 Efficient enumeration of multiple contingencies and power system response simulation

This section presents the modules for the efficient enumeration of multiple contingencies and for the assessment of their impact by simulating the power system

response to the contingencies themselves.

The methodology adopts an analytical probabilistic approach to enumerate the multiple contingencies which most contribute to the Expected Energy Not Served (EENS) risk indicator. The enumerate process consists of the following steps:

1. Calculation of a correlation matrix, to account for the fact that a severe weather event can affect more than one line during the event duration;
2. Identification of clusters of lines with high correlation, based on the correlation matrix;
3. Identification of relevant contingencies, i.e. combinations of tripping and not tripping of lines with non-negligible probability within each cluster;
4. Calculation of the probability of multiple contingencies.

The steps are described in more detail in the sequel.

Efficient enumeration of multiple contingencies: calculation of correlation matrix

The method starts from an $[N_{events} \times N_{lines}]$ event matrix M evaluated as in Chapter 2.1.2, where N_{events} is the number of weather events when a specific intensity threshold has been overcome at least on one line of the set, N_{lines} is the total number of lines considered in the analysis.

$$M(i,j) = \begin{cases} 0 & \textit{if i-th event does not strike j-th line} \\ 1 & \textit{if i-th event strikes j-th line} \end{cases} \tag{2.3}$$

Matrix M allows to compute the event tables which report the number of weather events when the intensity threshold has been overcome on the lines, see example referring to lines L1 and L2 in Table 2.1.

Table 2.1: Event table for lines L1 and L2

	L2	**Not L2**	**Totals**
L1	n_{11}	n_{10}	n_{1*}
Not L1	n_{01}	n_{00}	n_{0*}
Totals	n_{*1}	n_{*0}	

where:

- n_{11} is the number of severe events for which both lines L1 and L2 are affected by a weather variable exceeding a threshold Th [m/s] for wind and [kg/m] for ice-sleeve formation;
- n_{10} is the number of severe events for which line L1 is affected while line L2 is not affected by a weather variable exceeding a threshold Th;
- n_{00} is the number of severe events for which neither line is affected by a weather variable exceeding a threshold Th;
- n_{01} is the number of severe events for which line L2 is affected while line L1 is not affected by a weather variable exceeding a threshold.

The Linear Correlation Coefficient (φ) between line L1 and L2 is computed as in Equation 2.4.

$$\varphi_{12} = \frac{n_{11}n_{00} - n_{10}n_{01}}{\sqrt{n_{*1}n_{*0}n_{1*}n_{0*}}} \tag{2.4}$$

Repeating the computation in Equation 2.4 for any pair of lines, the algorithm builds the line correlation matrix R for the whole set of lines.

Line clustering

The clustering algorithm represents a fundamental pillar for the efficient calculation of long-term resilience indicators. In fact, these indicators will be computed considering only a subset of N-k contingencies, which affect some representative "clusters" of lines. A sound dimensional reduction starts from the selection of suitable line clusters, which represent a good trade-off between computational time and accuracy, taking into account the extension of past weather events over grid lines through Linear Correlation Matrix (R). To meet such requirements, this algorithm allows to create clusters with a user-defined threshold of minimum internal correlation between the lines in each cluster. Specifically, a hierarchical agglomerate algorithm is applied to cluster the lines based on correlation matrix R: in case the agglomerate algorithm provides very large clusters, these clusters are split into smaller ones considering topological information (e.g. the connection of the lines to the same substation).

Screening contingencies

The previous clustering steps allow for a reduction in the number of possible N-k contingencies; however, the methodology applies an effective approach based on total probability theorem and copulas of binary variables to efficiently filter

out multiple contingencies, also suitable for large power system applications. In particular, the probability of the logical *AND* event related to the failures of n lines can be expressed in terms of a copula CDF of binary Bernoulli variables, each of which represents the probability of a specific status of each line (in service / out of service). The above calculation of CDF values via copulas allows to filter out contingencies with negligible probability by exploiting the total probability theorem. In fact, given that a contingency consists in a combination of *ns* tripping and *nns* not tripping of lines, its probability is always lower than the probability of the logical *AND* of the *ns* trippings thanks to the total probability theorem. Thus, first, the algorithm computes the probability of an exhaustive set of combinations (logic *AND*) of trippings and discards all the ones for which the probability is lower than a given probability threshold. After that, all the contingencies which include any of the discarded *AND* combinations are also discarded by the algorithm.

Copula based calculation of contingency probabilities

Once identified the set of contingencies, their probabilities are computed by applying the theory of copulas for binary variables in each cluster. By Sklar's theorem [17] applied to discrete (particularly binary) variables which represent the statuses of the OHLs, the probability of the occurrence of a generic *h-th* contingency ($prob_{ctg,h}$) meant as a combination of a set of trippings (S) and a set of not trippings (NS), i.e. *P(S & NS)*, can be written as an algebraic sum of the cumulative distribution of Probability of the Copula (C) evaluated at suitable points $\bar{s}^{(\mathrm{i})}$ in subset Ω_{h} of the binary variable space, according to the general formula indicated in Equation 2.5 and related to a cluster of cardinality n and with Linear Correlation Matrix (R).

$$prob_{\mathrm{ctg,h}} = P(\bar{X}^{(\mathrm{h})}) = \sum_{\bar{s}^{(\mathrm{i})} \in \Omega_{\mathrm{h}}} sign(\bar{s}^{(\mathrm{i})}) C[F_1({s_1}^{(\mathrm{i})}) ... F_n({s_n}^{(\mathrm{i})}), R] \tag{2.5}$$

Where:

$$\bar{X}^{(\mathrm{h})} = (X_1 = {x_1}^{(\mathrm{h})}, ..., X_n = {x_n}^{(\mathrm{h})}) \tag{2.6}$$

$\bar{X}^{(h)}$ is the vector of statuses of the OHLs in the h-th contingency and $\bar{s}^{(\mathrm{i})}$ is the i-th point with n components ${s_1}^{(i)}, ..., {s_n}^{(i)}$ where generic term ${s_m}^{(i)}$ can be set to ${x_m}^{(h)}$ or ${x_m}^{(h)}$*-1*. Function $sign(\bar{s}^{(i)})$ is evalueted in Equation 2.7.

$$sign(\bar{s}^{(\mathrm{i})}) = \begin{cases} 1 & if {s_m}^{(i)} = {x_m}^{(h)} \text{-1 for an even number of positions } m \\ -1 & if {s_m}^{(i)} = {x_m}^{(h)} \text{-1 for an odd number of positions } m \end{cases} \tag{2.7}$$

Power response simulation

The power system response to contingencies selected in the previous step is evaluated using a cascading outage simulator which performs the following analyses:

- a post-contingency load flow analysis, with the identification of possible overloads caused on the surviving grid components;
- the identification of any additional line trippings due to previous overloads (cascading outage analysis);
- application of the re-dispatching of generation units aimed at relieving overloads and at bringing the lines back into a secure operational condition, quantifying any load shedding actions needed after the generation redispatch;
- registration of load disconnections at substations in case of each identified contingency and calculation of the related risk indicatorExpected Energy Not Served (EENS) on an annual basis [MWh/year], which is defined by ENTSO-E [18] as the expectation value of the amount of energy not being served to consumers on yearly basis, due to system capacity shortages or unexpected outages of assets;

The $EENS_{PS,j}$ (Expected Energy Not Served at *j-th* substation) is computed in Equation 2.8:

$$EENS_{\mathrm{PS,j}} = \sum_{h=1}^{N_{\mathrm{ctg,j}}} t_{\mathrm{recovery}} \cdot Load_{j,h} \cdot prob_{\mathrm{ctg,h}} \tag{2.8}$$

where $N_{ctg,j}$ is the number of contingencies causing a partial or total loss of supply at the *j-th* substation, $Load_{j,h}$ is the unserved load at the *j-th* substation for the *h-th* contingency, the $prob_{ctg,h}$ computed in 2.5 which determines the loss of load at the *j-th* substation, while a $t_{recovery}$ is the conventional recovery time set to 16 hours.

2.1.7 Case study

This section presents a case study to demonstrate the effectiveness of the Terna-RSE methodology in identifying the critical and priority areas and in quantifying the benefits of the hardening interventions on the grid. The analyses are based on the calculation of the EENS index, which represents the performance level of the grid. The EENS can measure the risk level associated with the outage of a substation connected to the HV grid, because it combines:

- the probability of occurrence of substation outage;
- the potential impact of the outage in terms of energy [MWh] not served to the affected customers.

Therefore, via the EENS index the TSO can identify and assess the high-risk area, i.e., the ones characterized by higher values of EENS, in order to define the priority interventions necessary to enhance the resilience and security of the grid and mitigate the loss of load risk. Moreover, the benefits achievable through the implementation of the interventions can be calculated in terms of reduction of EENS for the substations of the area under study.

Test system

The case study refers to a real portion of the transmission system which is critical for weather induced failures. In particular, in Figure 2.5 report a diagram of the grid portion under study and Table 2.2 report a linear correlation coefficient among the lines which are derived from historical severe weather occurrences recorded close to the lines. The loads at the four Primary Substation (PS) are evaluated based on the available historical series of power consumptions. In an *average loading grid condition* the loads at the PSs are reported in Table 2.3. The RPs of the lines are reported in Table 2.4. The analysis considers both direct and indirect effects of the weather threat considered on the OHLs.

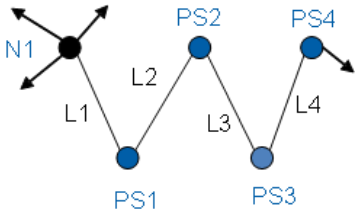


Figure 2.5: One line diagram of the portion of the grid vulnerable to weather events. The black arrows represent the connections to the rest of the HV grid

Evaluation of the EENS in the pre-intervention phase

In the pre-intervention phase, aimed at identifying the high-risk areas of the grid, the methodology enables to identify and assess all the possible and meaningful contingencies reported in Table 2.5 for increasing values of RP, quantifying their $prob_{ctg,h}$. This probability term depends both on the probability of occurrence

Table 2.2: The correlation sub-matrix corresponding to the set of lines L1, L2, L3, L4

	L1	**L2**	**L3**	**L4**	**...**
L1	1	0.987	0.995	0.107	
L2	-	1	0.999	0.106	
L3	-	-	1	0.107	
L4	-	-	-	1	
...	-	-	-	-	1

Table 2.3: Loads at primary substations in an average loading condition of the grid

Substation	**Load [MW]**
PS1	30
PS2	20
PS3	10
PS4	30

Table 2.4: Return Period of the four lines of the case study

Line	**RP [Year]**
L1	3
L2	13
L3	13
L4	∞

of the impacting weather event and on the probability that, upon the occurrence of the weather event, those lines and no others are affected and experience an outage. Therefore, this probability of occurrence is a function of both the RP of the lines and of the level of meteorological correlation between them, which is evaluated considering the weather events that occurred on the lines over a multi-year historical horizon.

Afterwards, the response of the system to the above mentioned contingencies is analyzed, assuming a conventional restoration time of the outages of 16 hours. Table 2.6 reports the amount of unserved load, the yearly contingency probability of the failure occurrence and the EENS indicator for the three contingencies that cause the disconnection of PS1 substation. Of course, contingency G also causes the disconnection of PS2 substation, but Table 2.6 only lists the impact, probability and risk indicators EENS associated with PS1 substation. The methodology evaluates

Table 2.5: List of analyzed contingencies for increasing RP values

RP [Year]	Ctg ID	Outaged Lines			$prob_{ctg,h}$ [p.u./year]
		L1	L2	L3	
3	A	1	0	0	0.208977
13	B	0	1	0	0.000465
	C	1	1	0	0.018467
	D	0	0	1	0.000463
	E	1	0	1	0.018469
	F	0	1	1	0.000057
	G	1	1	1	0.055354

the EENS indicators for each substation of the grid portion under test. The total EENS associated with PS1 substation is equal to 44.3 MWh/year and the RP of PS1 substation outage is 11 years. It is worth noticing that the response of the system to multiple contingencies is simulated considering the model of the whole transmission system in the cascading outage simulator.

Table 2.6: Contributions of contingencies affecting PS1 substation to annual EENS

RP [Year]	Ctg ID	Unserved load [MW]	$prob_{ctg,h}$	$EENS_h$ [MWh/year]
13	C	30	0.018467	8.9
	E	30	0.018469	8.9
	G	30	0.055354	26.6

Evaluation of the EENS in the post-intervention phase and quantification of the benefit for CBA

After the identification of the critical and priority portions of the grid, the relevant areas are analysed to define the interventions necessary to increase the level of resilience of the transmission infrastructure and, consequently, of the substations.

Lines L2 and L3 present few spans with relatively low RP for the weather threat under study. In this specific case the most cost-effective solution identified via the Cost Benefit Analysis (CBA) consists in the partial undergrounding of the lines, thus avoiding the exposition of critical line spans to the threat. This intervention makes lines L2 and L3 resilient to the threat under study. Alternative solutions involving the partial undergrounding of line L1 (with more spans exposed to the threat and a lower RP with respect to lines L2 and L3) are deemed less convenient by the CBA.

The capability provided by the methodology to punctually evaluate how the intervention on each line span can affect the overall resilience level of the system enables the TSO to identify the minimum hardening actions required, thus guaranteeing the cost-effectiveness of the grid planning process. Finally, applying again the methodology in the post-intervention scenario leads to a null value of the EENS for substation PS1 with reference to the specific threat, which means that the substation is completely resilient to the threat. In the end, the benefit of the intervention, in terms of EENS variation, is given by Equation 2.9.

$$\Delta EENS = EENS_{\text{ps,post}} - EENS_{\text{ps,pre}} = -44.3 MWh/year \tag{2.9}$$

2.1.8 Conclusions

This section presented an innovative methodology, jointly developed by RSE and Terna, aimed at assessing long-term resilience indicators as a means of prioritizing grid reinforcement actions. This innovative approach, which is the result of close collaboration between experts in energy systems, grid planning, component design and meteorology, is currently focused on solving the main causes of failure of the Italian HV and HV grid, namely wet snow and high wind events. To this end, it evaluates the return periods of outages in the HV/HV substations feeding the distribution networks, starting from the return periods of outages in the lines connected to the substation and considering the mesh level of the network. After a successful validation phase, the methodology was approved by the Italian Regulatory Authority and published as an addendum to the Italian TSO network code. The methodology itself is based on a probabilistic framework. It combines probabilistic climatological models that predict extreme values of stress variables (such as snow loads and wind speeds) over various time horizons (up to the year 2050) with probabilistic analytical models that assess the vulnerability of overhead lines (OHL) to the direct and indirect effects of wet snow and wind. Thanks to the methodology, it will be possible to anticipate climate scenarios during the planning phase and to consider all potential weather events and their combinations that are considered essential to effectively address the impacts of climate change on network planning strategies. The application of this methodology demonstrates its effectiveness in assessing the return periods of line disruptions in line with operational experience. Furthermore, it effectively quantifies the benefits of grid interventions, expressed in terms of changes in energy not supplied (EENS) and return periods of substation outages.

2.2 Tree interference mapping with LiDar for overhead lines

Strong wind, representing one of the major causes of load disruptions in the Italian TSO, can affect OHL in two ways [11]:

- direct effects: by directly applying a pressure on the sub-components of the line, causing mechanical damage on the infrastructures;
- indirect effects: causing contact between the surrounding vegetation and the line [12].

By the fact that about the 70% of Italian power OHLs are in forested area, due to the orography of the Italian territory, the vegetation management is a crucial task carried out by monitoring with sensors and helicopters, and by preventive and specific tree cuts. This represents an important activity for Terna to guarantee power supply.

A statistical approach to model grid asset vulnerability to tree falls is presented in [19] which proposes a predictive method for distribution feeder vegetation management based on a risk framework, accounting for a variety of factors extracted from network parameters and historical outage data, the historical weather and weather forecast data, various vegetation indices and high resolution imagery data, and historical utility records about outages and maintenance. However, statistical models can be affected by classification errors (e.g. in fault recording) and cannot quantify the benefit coming from countermeasures (e.g. specific trimming policies).

Terna and RSE have been collaborating for some years in the development of a risk-based methodology for resilience assessment, that relies on physics-inspired vulnerability models [2], as described in Section 2.1. The methodology adopts an analytical and engineering-based modeling approach for line vulnerability, with a detail up to the level of each OHL span, considering actual design parameters and the orography and vegetation to analyze both direct and indirect effects. In recent years, several scientific studies have been carried out regarding probabilistic models representing the vulnerability of OHL against strong wind events, including [12]. The use of this model implies an accurate and punctual mapping of the vegetation present around the electrical energy transmission infrastructures. The current model [12] of OHL vulnerability to interfering vegetation used in the Terna-RSE methodology exploits CORINE Land Cover database [13] to map the vegetation present in Italy. However, this database provides average values for tree features and does not contain precise indications on actual conditions of tree interference along the Right of Way (ROW) of the line. To fill this gap, the present paper proposes an advanced vulnerability model which integrates the vegetation mapping

based on LiDar systems [14] which can be more accurate and updated than the approach in CORINE.

2.2.1 Availability of dataset for vegetation mapping in resilience assessment analyses

This section describes the major data sources available for vegetation mapping, with a focus on the data from LiDar systems to be used in the advanced vulnerability model.

CORINE Database

The assessment of OHL vulnerability to tree fall due to strong wind requires the characterization of many features for the different tree species (trunk height, coniferous or broad leaf, maximum breaking strength, root-soil system features), also including their uncertainties. To this purpose, the actual vulnerability model in Terna-RSE methodology [2] uses the COoRdination of Information on the Environment (CORINE) Land Cover database, which provides the data needed for modelling of tree interference. This database, developed in collaboration with Superior Institute for Environmental Protection and Research (ISPRA) as part of Copernicus project [20], is based on satellite images. The Database (DB) maps the land use and coverage and the possible presence of vegetation with a scale of 1:100000, providing the mean, minimum and maximum values of vegetation height based on mapped tree species. CORINE DB is updated each 6 years: thus, the information contained is not very up to date. A Geographical Information System (GIS) is used to overlap vegetation information and OHLs coordinates (Figure 2.6): this allows to retrieve the vegetation type and to calculate the percentage of interfering and prevalent High-Stemmed (HS) and Low-Stemmed (LS) vegetation, with a single span detail along the line route.

Figure 2.7 shows the results of the statistical analysis about tree interference on the OHLs, with a focus on two Italian regions. Mixed and high vegetation are the most dangerous types of vegetation for OHLs because such trees, even though outside the ROW, are most likely to impact the lines in case of strong wind or gusts. The average height of the trees in the two region is about 28 m for HS species and 11 m for LS species.

Lidar inteference mapping

Besides not being frequently updated, CORINE data have relatively low resolution. Thus, a frequently updated and more accurate mapping of vegetation interference can be an interesting step forward for vulnerability assessment. As part of its

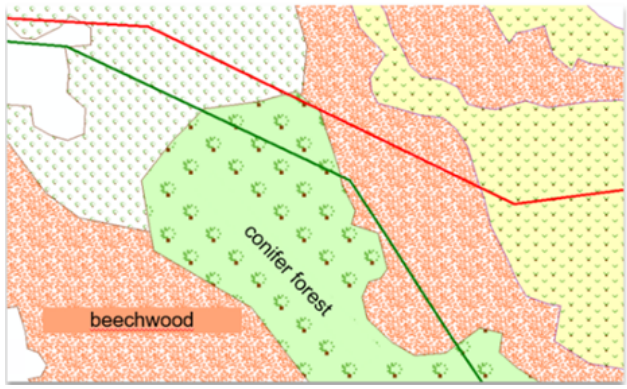


Figure 2.6: Example of overlapping between CORINE DB tree coverage maps and the route of two lines

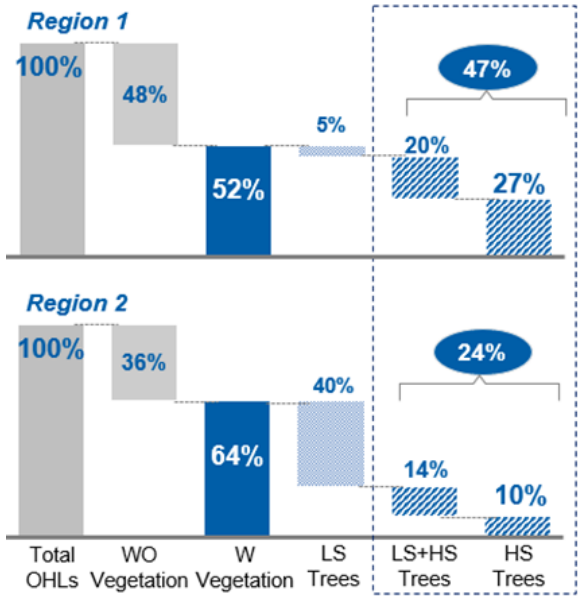


Figure 2.7: Analysis of vegetation type on two Italian regions with CORINE DB

maintenance practices, Terna uses its fleet of helicopters to carry out the mapping of the terrain around the lines using LiDar [14] a remote sensing system that allows to measure the distance of an object or surface from power lines using a laser pulse.

The main objective of the inspections is to measure the actual distance between power lines and surrounding vegetation, in order to map possible tree interference and plan preventive cutting actions, as shown in Figure 2.8.

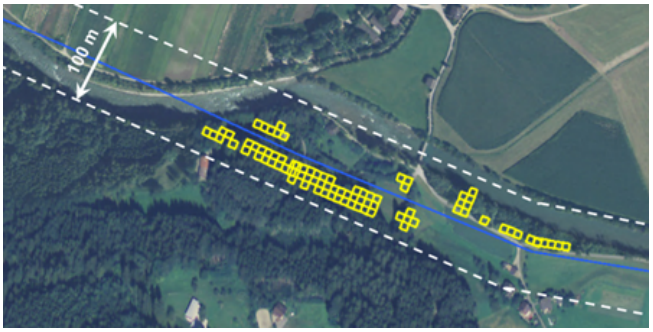


Figure 2.8: LiDar mapping of tree interference around the line route

The LiDar mapping has a width equal to 50 meters per line side with spatial resolution up to 1 m x 1 m and allows an accurate reconstruction of orography and of the presence and height of vegetation along the lines, as shown in Figure 2.4. This information is updated annually by means of new surveys.

LiDar Data useful for vulnerability assessment

Among the data made available by LiDar systems, the advanced model intended for OHL vulnerability to tree interference requires data about potential contacts between a cylindroid centered on the catenary of the wires (conductors and/or shield wires) and the potentially interfering vegetation both in the ROW and, above all, outside the ROW, inside each cell 1 m x 1 m along the route of each line span.

As far as the vertical and lateral contacts are concerned, the diameter of the cylindroids around the conductor is a function of the voltage level of the line. The intersection of the vegetation with only the outermost cylindroid is classified with a lower criticality level (deferrable action) than the case of the intersection of the vegetation also with the innermost cylindroid, classified with a higher criticality level (urgent). Table 2.7 shows the radius of the cylinders considered per voltage level (e.g. if the minimum distance along the span of a 150 kV line between the conductor and vegetation is less than 2.5 metres, this will result in an urgent criticality level).

To carry out these assessments, a catenary was considered for the conductors in conditions of maximum inclination, in line with the indications of Std. CEI

Table 2.7: Values of distances for deferrable and urgent criticality

Voltage [kV]	Deferrable criticality [m]	Urgent criticality [m]
≤150	5	2.5
220	6	3.5
380	8	5

11.4 [9] already adopted for the creation of the "basic" vulnerability model in [12]. Therefore, the useful data for the advanced vulnerability model are:

- possible vertical interference between the cylindroid of the wire with trees inside the ROW in a specific cell 1 m x 1 m: in this regard a parameter P1 is defined with binary value 0 (no vertical contact), 1 (vertical contact) for each cell along the route of the span;
- possible lateral contact due to interference of the cylinder along the 30° inclined catenary with trees outside the ROW in a specific 1 m x 1 m cell: in this regard, a parameter P4 is defined with binary value 0 (no lateral contact), 1 (lateral contact) for each cell along the span ROW, with indication of the distance D_{int} of the interfering tree from the 30° inclined catenary (value from Std CEI 11.4 [9]);
- possible lateral contact of the cylindroid due to the overturning of trees from outside the ROW in a specific cell 1 m x 1 m: a parameter P2 is defined with a binary value equal to 0 (no lateral contact) or 1 (lateral contact) for each cell along the span route.

For each of these potential contacts, the LiDar system also indicates whether an urgent or deferrable maintenance intervention is associated with it. Another piece of information, provided by processing the three-dimensional terrain model with 10 m resolution with GIS tools, consists of a more accurate evaluation of the slope of the terrain, compared to the contour lines adopted in the original model, on the 10 m x 10 m cells with possible interferences on the line route. These elaborations derive the maximum, average and minimum slope value within the cell.

2.2.2 The proposed advanced model for indirect effects of wind and wet snow

This section presents the advanced vulnerability model of OHL spans to indirect effects of interfering vegetation, including LiDar indications, and its implementation

in Vulnerability assessment tool (VULLINE), developed by RSE for Terna-RSE methodology [2].

The original model: some limitations

For the sake of clarity, this subsection recalls the analytical model for the vulnerability of OHL span to indirect effects of wet snow and wind described in [11] [12]. Let us consider a line (see Figure 2.3) surrounded by trees with a linear coverage density δ_{out} outside the ROW and possibly a density δ_{in} inside the ROW (δ_{in} nearly 0, given the Terna strict maintenance practices in line with Std CEI 11-4 [9]). Let us P_F define the probability of Event F, i.e. failure of a line span due to the contact of a tree. Event F can be caused by:

- probability of failure of a line span due to lateral contact of a tree (*Event C*) due to the tree fall or the lateral swing of the conductor onto a tree branch;
- probability of failure of a line span due to vertical contact of a tree (*Event V*).

$$F = C \cup V \tag{2.10}$$

Considering that trees can be inside (*Event I*) and/or outside (*Event O*) the ROW leads to Equation 2.11 and then to Equation 2.12.

$$F = (C \cup V) \cap (O \cup I) \tag{2.11}$$

$$F = (C \cap O) \cup (C \cap I) \cup (V \cap O) \cup (V \cap I) \tag{2.12}$$

Events $(C \cap I)$ and $(V \cap O)$ can be assumed as empty ($\emptyset$) because negligible harm can be provoked by the fall of trees inside the ROW or by the vertical contact of trees outside the ROW. Thus Equation 2.12 can be can be simplified as Equation 2.13.

$$F = (C \cap O) \cup (V \cap I) \tag{2.13}$$

where $(C \cap O)$ and $(V \cap I)$ respectively represent the independent events that a tree inside the ROW has a vertical contact with a phase conductor, and that a tree outside the ROW has a lateral contact with the phase conductor. Thus the probability of failure of a line span due to the contact of a tree (*Event F*) i.e. P_F can be written as Equation 2.14:

$$P_F = 1 - [(1 - P_r(C \cap O)) \times (1 - P_r(V \cap I))] \tag{2.14}$$

Figure 2.3 shows the diagram of the forces acting on the tree. $F_{wc,o}$ and $F_{wc,v}$ are the horizontal and vertical components of the force exerted by wind on the conductor, while $N_{c,i}$ and $N_{c,pp}$ are the vertical forces on the conductor due to its own weight and ice/snow. $F_{w,o}$ is the horizontal component of the force exerted by wind on the tree, while N is the resulting normal force acting on the tree due its own weight, wind and snow. Thus, the final probability of failure of a line span due to vertical contact and/or lateral fall of the trees inside and outside the ROW according to the original vulnerability model in [12] is given by Equation 2.15.

$$P_F = 1 - [(1 - P_{r1}) \times (1 - P_{r2,3}) \times (1 - P_{r4})] \tag{2.15}$$

where, in particular the expressions for P_{r1}, $P_{r2,3}$, P_{r4} are reported in Equations 2.16, 2.17, 2.18.

$$P_{r1} = 1 - \left(1 - \int_{TS}^{\infty} S(y)dy\right)^{\delta_{\text{in}}\text{L}} \tag{2.16}$$

$$P_{r2,3} = 1 - \Big(1 - P_r(M_{\text{overtuning}} - M_{\text{lim}} > 0) \times \times (P_r(h_{\text{t,outROW}} - (h_c^2 + la^2 + cl^2)^{0.5} > 0\Big)^{\delta_{\text{out}}\text{L}} \tag{2.17}$$

$$P_{r4} = 1 - \left[1 - P_{r2,3}(sag \times \sin\zeta \geq \frac{ROW}{2} - b_{\text{r}}) \times \times P_r\left(h_{\text{t,outROW}} \pm \frac{ROW}{2} \cdot \sin slope \geq ... \geq ht - \sqrt{(Q_{\text{sag}}{}^{0.99})^2 - \left(\frac{ROW}{2} - b_{\text{r}}\right)^2}\right)\right]^{\delta_{\text{out}}\text{L}} \tag{2.18}$$

P_{r1} in Equation 2.16 is the probability of vertical contact of the line conductor given a linear tree density inside the ROW equal to δ_{in} and a line span equal to L, being $S(\cdot)$ the convolution of tree height density and conductor sag density and $TS = HT$ - $b_r \cdot \sin slope$, b_r is the bracing of the tower, *slope* is the slope angle of the terrain and HT is the tower support height, as in [12].

$P_{r2,3}$ in Equation 2.17 is the probability that the tree is overturned and strikes the line, i.e. the $M_{overtuning}$ applied by forces is higher than the maximum moment of the soil-root system M_{lim} and the tree outside ROW has a higher height with

respect to the distance between tree and conductor given by $(h_c{}^2 + la^2 + cl^2)$ where h_c is the height of the lowest point of the phase conductor from the terrain, cl is the clearance distance (see Figure 2.3) and la is the distance along the direction of the line.

P_{r4} in Equation 2.18 is the probability of lateral contact due to swinging of the conductor, where $Q_{sag}{}^{0.99}$ is the 99^{th} quantile of the sag of the line, ζ is the inclination angle of the catenary due to vertical and horizontal forces.

The limits of the presented model are the following:

- it does not consider the actual location of the potential interfering trees with respect to the layout of the line, assuming an average density of trees outside the ROW equally subject to overturning on the span itself, which can lead to an overestimation of the exposure of the line to possible tree interference;
- it does not consider the actual location of the line with respect to the direction of maximum orographic gradient.

To fill these gaps, the advanced model integrates LiDar data in order to evaluate the terms in 2.15 with a higher accuracy. In fact, these data rely on short term updated monitoring of vegetation interferences on the actual OHL right of way layout, thus they can account for aspects (such as tree growth over the years) which are extremely uncertain and for which a quantitative model is far from being available.

Adding LiDar information in the vulnerability model

The advanced model adopts a cell-based representation of the single OHL span, i.e. the LiDar system analyses all the 1 m x 1 m squares around the ROW of the individual spans. Specifically, indexes i and j will be used respectively for the span and the cell.

1. ***Lateral contact due to overturning of the tree***

Term $P_{r2,3,j}{}^{(i)}$ associated to the probability of failure of *i-th* span due to lateral contact of a tree from outside ROW at *j-th* cell is translated as in Equation 2.19.

$$P_{r2,3,j}{}^{(i)} = P_r(M_{\text{overtuning,j}} - M_{\text{lim,j}} > 0)\times \\ \times (P_r(h_{\text{t,outROW,j}} - (h_{\text{c,i}}{}^2 + la_{\text{i,j}}{}^2 + cl_{\text{i,j}}{}^2)^{0.5} > 0) = P_{r3,j}{}^{(i)} \times P_{r2,j}{}^{(i)} \quad (2.19)$$

For the generic *j-th* cell of the *i-th span*, the LiDar data can provide one of the two alternative outcomes:

- parameter $P_{2,j}{}^{(i)}$=0: no geometric contact with the span outside ROW for cell j and span i. As a consequence, term $\mathrm{P_{r2,j}}^{(\mathrm{i})}$=0. Thus, $P_{r2,3,j}{}^{(i)}$ =0.
- parameter $P_{2,j}{}^{(i)}$=1: presence of geometric contact with a tree outside ROW for *j-th* cell and *i-th* span. In this case Equation 2.20 holds valid:

$$P_{r2,3,j}{}^{(i)} = P_r(M_{\mathrm{overtuning,j}} - M_{\mathrm{lim,j}} > 0)\times \\ \times \left(P_r(h_{\mathrm{t,outROW,j}} - ({h_{\mathrm{c,i}}}^2 + {la_{\mathrm{i,j}}}^2 + {cl_{\mathrm{i,j}}}^2)^{0.5} > 0 \right) = P_{r3,j}{}^{(i)} \quad (2.20)$$

To calculate $P_{r3,j}{}^{(i)}$ the model applies the same physics inspired model of interaction shown in [12] by exploiting some data on vegetation coming from CORINE DB [13] specifically the maximum, minimum and mean heights for the tree in each cell, in order to estimate the resistance of the tree itself to overturning, also including uncertainties in some tree features (e.g. wood density).

2. ***Contact due to lateral swing***

In this case, parameter $P_{4,j}{}^{(i)}$ is used to evaluate the term associated to the contact probability due to lateral swing (Probability contact due to lateral swing of the inclined catenary of the *i-th* span and the tree at *j-th* cell).

- parameter $P_{4,j}{}^{(i)}$=0: absence of lateral contact due to swing of the inclined catenary of the *i-th* span and the tree at *j-th* cell. This implies that the probability of lateral contact due to swinging is $P_{r4,j}{}^{(i)}$=0;
- parameter $P_{4,j}{}^{(i)}$=1: possible presence of lateral contact due to swinging of inclined catenary. In this case, the LiDar system provides an estimation of the distance of a tree from the line axis i.e. D_{int}. Thus, ROW is calculated as in Equation 2.21.

$$ROW^* = b_r + fr_{ms}\sin(30^\circ) + D_{int} \quad (2.21)$$

where b_r is the bracing of the cross-arm of the tower and fr_{ms} is the sag in the conditions of maximum temperature, according to design standard [9]. Thus, the final term $P_{r4,j}{}^{(i)}$ is given in Equation 2.22.

$$P_{r4,j}{}^{(i)} = \Bigg[P_r(sag_i \times \sin\zeta \geq \frac{ROW_i^*}{2} - b_{\mathrm{r,i}}) \times$$
$$\times P_r\Bigg(h_{\mathrm{t,outROW,j}} \pm \frac{ROW_i^*}{2} \cdot \sin(slope, j) \geq hs_i - \sqrt{(Q_{\mathrm{sag,i}}{}^{0.99})^2 - \left(\frac{ROW^*}{2} - b_{\mathrm{r,i}}\right)^2} \Bigg) \Bigg] \tag{2.22}$$

3. ***Vertical contact***

Parameter $P_{1,j}{}^{(i)}$ from LiDar systems is used to model the possible vertical contact: this parameter is particularly important because it allows to identify situations (e.g. valleys) where there is no vertical contact even if the sag of the span is comparable to the tower heights. In particular:

- parameter $P_{1,j}{}^{(i)}$=0: absence of vertical contact between line and interfering vegetation. In this case, it holds: $P_{r1,j}{}^{(i)} = p_{1,j} = 0$.
- parameter $P_{1,j}{}^{(i)}$=1: presence of vertical contact between line and interfering vegetation. The calculation is done as in Equation 2.23 according to the model in [12], using CORINE data for tree height.

$$P_{\mathrm{r1,j}}{}^{(\mathrm{i})} = \int_{hs}^{\infty} P_{V,i}(y) \cdot pdf_{ht_i nROW,j}(y) dy \tag{2.23}$$

Overall span failure probability

For any cell with a potential tree interference, the model calculates the probability P_{fs} for which the tree in cell j interferes with the *i-th* span, calculated in Equation 2.24

$$P_{\mathrm{fs}}(i,j) = 1 - (1 - P_{\mathrm{r1,j}}{}^{(\mathrm{i})})(1 - P_{\mathrm{r2,3,j}}{}^{(\mathrm{i})}(1 - P_{\mathrm{r4,j}}{}^{(\mathrm{i})}) \tag{2.24}$$

The more accurate indications from LiDar systems allow to avoid using the tree density parameters δ_{out} and δ_{in}, because the failure probability P_{fs} is calculated for any *j-th* cell interfering with *i-th* span of the line. Thus, under the realistic assumption that a single event of strong wind affects all the interfering cells at the same time, the total failure probability of span *i*, $P_{f,i}$ can be calculated as in Equation 2.25.

$$P_{\mathrm{f,i}} = \max_{j=1,\ldots,n_i} P_{\mathrm{fs}}(i,j) \tag{2.25}$$

2.2.3 Case study

This section compares the performances of the original vulnerability model, which uses only CORINEDB, and of the advanced model, which also integrates LiDar information [21]. To this purpose, the analysis is performed on a set of 117 lines (a representative subset of lines in the Italian EHV and HV transmission system, which are relevant from the point of view of tree interference). For analysis purpose, the lines are divided into subsets by voltage level. In Table 2.8 compares the numbers of lines (for each voltage level) with RPs < 50 years (critical lines) and with RP < 15 years (very critical lines), calculated with the original model using exclusively CORINE database, and the advanced model integrating LiDar information.

Table 2.8: Comparison of the line failure RP's for vegetation interference between original model (using exclusively CORINE DB) and the advanced vulnerability model integrating LiDar map

		Indirect effects analysis only using CORINE data		Indirect effects analysis integrating also LiDar mapping	
Voltage Level [kV]	# Analyzed OHLs	# OHLs RPs<50	# OHLs RPs<15	# OHLs RPs<50	# OHLs RPs<15
400 & 220	13	13	13	10	9
150	32	31	30	25	18
132	61	58	55	54	48
≤ 132	11	9	9	9	9
Totals	117	111	107	98	84

The LiDar-based mapping of the vegetation around the line route allows an accurate identification of potential interferences of vegetation with the OHL route, as well as frequent updates in the identification process above. All this avoids over estimations due to the naive overlapping of CORINE low-resolution tree coverage maps and the grid asset layout. Specifically, the following considerations can be done:

1. Although the higher voltage levels (220/400 kV) are naively supposed not to have vegetation interference problems, a potential risk of failure from the overturning of trees from outside ROW is confirmed by LiDar;

2. For voltage levels $\leq$132 kV the criticalities found with CORINE are confirmed

by LiDar surveys, while significant reductions of critical lines (-19%) and of very critical lines (-40%) are identified at 150 kV level.

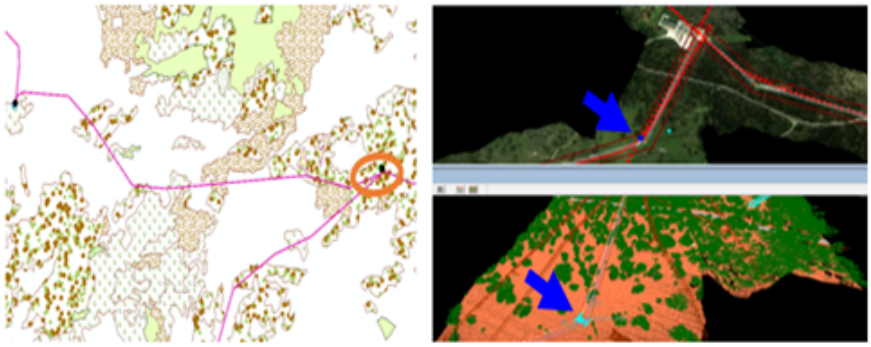


Figure 2.9: (a) Overlap between CORINE tree coverage map and line route. (b) LiDar information about actual interfering cells along the line routes

In order to explain the overestimation, Figure 2.9 shows an example of line span: based on the map overlapping in Figure 2.9 (a), the line is critical (RP $<$ 50 years) according to the model only based on CORINE DB which indicates the presence of an area with predominantly tall-stemmed forests with holm oaks and cork oaks with an average height between 20 and 28 m. Instead, from Figure 2.9 (b) it can be seen that LiDar mapping does not detect interferences with vegetation, so the span is resilient (i.e. RP $<$ 50 years) to wind indirect effect.

2.2.4 Conclusions

An advanced analytical model to assess the vulnerability of overhead line spans to interfering vegetation is developed, also including the tree interference mapping available from LiDar systems. The simulations performed on a representative set of OHLs in the Italian transmission system show that the proposed model provides a 40% reduction in the number of very critical lines (i.e. lines with RP's not higher than 15 years) with respect to the model which only uses CORINE land cover information.

2.3 Interphase spacers to increase power system resilience against wet snow

As mentioned in previous sections, extreme weather events are increasingly impacting the electricity transmission grid, and it is the task of the Italian TSO, and others, to make the grid increasingly resilient. It is therefore essential to plan the right interventions to mitigate the effects of climate change, reducing both power outage probability and risk indicators such as the Expected Energy Not Served (EENS). In many countries, including Italy, wet snow events represent one of the main causes of load interruptions in both distribution and transmission grids: over the last 10 years, numerous studies have been conducted to assess and mitigate the effects of snow events on both system infrastructure and electricity supply service [11] [22][23]. Among the reinforcement interventions available, Interphase Spacers (IS) represent a capital-light measure under experimentation in Terna to counteract and mitigate the wet snow related phenomena, thus reducing the risk of outage of transmission power lines. The IS effects on the control of galloping phenomena and in case of wet snow sleeve shedding have been studied in the last years in the literature using complex finite element models [24] [25]. Despite this, Cost Benefit Analysis (CBA) for the prioritization of the interventions in large power systems require to quantify the benefits of these devices using models which represent a suitable trade-off between accuracy and applicability. To fill this gap, in this section proposes a model for these devices in the Terna-RSE resilience assessment methodology to quantify their benefits for CBA of the grid interventions.

2.3.1 The proposed model

This section presents an overview of the wet snow related phenomena for which IS may represent an interesting countermeasure.

Physical phenomena

Given the basic function of the interphase spacer (i.e. assuring the separation of the phases in case of actions which tend to reduce their distances), it is quite obvious that main phenomena for which interphase spacers can perform mitigative actions are:

- galopping;
- excessive reductions of the clearance distances between energised parts (conductors) of an overhead line and mass, due to unequal sags;

- excessive reductions of the clearance distances between energised parts and mass, due to the shedding of one wet snow sleeve. The wet slow sleeve accretion phenomenon is described by Makkonen model [26].

1. ***Galopping***

Galloping [27] is a phenomenon of vibration of the conductor characterized by low frequency (0.1÷1 Hz) and high amplitude (0.1÷1 times the sag of the concerned span) vertical oscillations and it is generated, under particular conditions of mechanical tensions, when the conductor is hit orthogonally by a low speed laminar wind. Even if the phenomenon can also occur on conductors on which there are no ice sleeves, it is more frequent in cases when there is an asymmetrical accumulation of ice or snow. In most cases, the phenomenon takes the form of stationary waves associated with the first three modes of vibration, which are those corresponding to the greatest amplitudes of oscillation and, consequently, to the greatest variations in axial tension on the conductors. Galloping can give rise to: *(i)* mechanical overloads (on the conductor itself, on the clamps, on the armaments and on the supports); *(ii)* imbalances between the tensions of the various phases, with anomalous torsional actions on the support; *(iii)* in the case of conductors arranged with overlapping phases, when one phase approaches the other temporarily, with possible tripping of the line due to violation of the phase-phase insulation distances. This phenomenon will not be considered in the current modelling framework.

2. ***Excessive reductions of the clearance distances due to unequal sags***

The process of wet snow accretion [11] [26] is due to the action of the wind which pushes the snow with a high content of water on the side of a wire: the wet snow adheres to the surface, starting from the cavities between the elementary strands. The snow adhesion to the conductor side moves the center of mass of the section away from the geometric barycentre of the wire, generating a torsional moment which tends to rotate the conductor itself, exposing a new free surface to the deposit of more snow and thus amplifying the phenomenon. The limited torsional stiffness of the conductor is therefore the main cause of the formation of large cylindrical sleeves in the presence of this type of precipitation. Operational practice shows that no equal thicknesses of sleeves are attained in the wires (conductors and shield wires) due to non-identical environmental conditions (snow flux, wind) affecting the wires. This can cause different sags to the wires, thus a reduction of the clearance distances among energised phases and mass (tower support, shield wires).

3. ***Excessive reductions of the clearance distances due to shedding of wet snow sleeves***

Another critical situation can take place when one wet snow sleeve around a wire (especially the lowest phase conductor) sheds due to the overcoming of the maximum adhesive and cohesive forces which can be exerted by snow. This causes two effects: *(i)* in the transient, the wire from which the snow sleeve detaches has a jump due to the released of the strain energy of the wire, causing potentially excessive reductions of the clearance distances between phases or between phases and shield wires. Moreover, the resulting impulsive action can also lead to mechanical overloads on the clamps and the attachment points of the support; *(ii)* in the post-detachment steady state, the wire with no sleeve has a smaller sag with respect to the other wires, which still can cause an excessive reduction of the clearance distances.

The Interphase Spacer: in-field application

The interphase spacers are installed in some lines of the Italian Italian Extra High Voltage (EHV) transmission system, in particular in the Northern regions: their number, location and characteristics (weight, etc.) are selected depending on the span length and the total difference of the heights of the attachment points of the phases themselves, according to the TSO design guidelines. Figure 2.10 reports an example of installation of the IS devices on a triple of phase conductors.



Figure 2.10: Installation of IS devices on a triple of phase conductors

The analytical vulnerability model: rationale and implementation in VULLINE Tool

The IS model is integrated in the wider modelling framework VULLINE, developed by RSE for the Terna-RSE resilience assessment methodology [2] and used to

model the vulnerability of OHLs to wet snow and wind direct and indirect threats. VULLINE [11] takes into account both the national and international standards [9][28] for design criteria and for the assessment of the actions of such threats on the OHLs sub-components. The IS applies its mitigation effect under manifold aspects:

1. it increases the torsional rigidity of the phase conductors, contributing to reduce the rotation of the wires, and thus, the amount of wet snow linear load [kg/m] accreted on the conductors themself;

2. it maintains a minimum distance between phase conductors, thus reducing the probability of excessively reduced clearance distances between conductors, under steady state conditions (post-detachment steady state, unequal sags);

3. during the transients following wet snow sleeve shedding, the IS absorbs part of the strain energy released by the unloaded conductor, thus reducing the jump height of the same wire, and thus helping avoid potential flashovers.

All these aspects are modelled in VULLINE tool.

1. ***Increase in torsional rigidity***

Concerning point 1, few works deal with experimental tests of the effectiveness of the interphase spacers in reducing the amount of linear wet snow load. In order to evaluate the vulnerability of a span endowed with IS to a specific linear load q_l, VULLINE tool applies a derating factor derived from [29] given in Equation 2.26, providing a "derated load" q_{IS}.

$$q_{\mathrm{IS}} = q_l \times [-0.276 \times \ln q_l + 0.5663] \tag{2.26}$$

2. ***IS effect on minimum clearance distances***

Concerning point 2, the authors extend the optimization formulation proposed in [30], by adding a constraint about the distances between phases 1 and 2 and between phases 2 and 3, which, in case of IS application, are at least separate by a distance equal to the IS length. For the sake of auto-consistency, the optimization problem is briefly recalled. Given a cylindrical coordinate system based on variables t (distance from one terminal) and γ (inclination angle with respect to vertical line) to mathematically formulate the potential trajectories $X_j(t_j, \gamma_j, F_j)$, $Y_j(t_j, \gamma_j, F_j)$, $Z_j(t_j, \gamma_j, F_j)$ the goal of the problem is shown for any specific linear wet snow load causing a vector F for the wire sags in Equation 2.27:

$$\arg\min_{\bar{t},\bar{\gamma}} \left[D_{min}(\bar{t},\bar{\gamma},\bar{F}) \right] \tag{2.27}$$

with:

$$\left[D_{min}(\bar{t},\bar{\gamma},\bar{F}) \right] = \min \left[D_{min,E}(\bar{t}^{(E)},\bar{\gamma}^{(E)},\bar{F}^{(E)}), D_{min,ESW}(\bar{t},\bar{\gamma},\bar{F}) \right] \tag{2.28}$$

$$D_{min,E}(\bar{t}^{(E)},\bar{\gamma}^{(E)},\bar{F}^{(E)}) = \min_{i=1...N_E, j=1...N_E, i\neq j} D_{i,j}\left([t_i^{(E)} t_j^{(E)}], [\gamma_i^{(E)} \gamma_j^{(E)}], [F_i^{(E)} F_j^{(E)}] \right) \tag{2.29}$$

being $D_{min,E}$ (minimum distance among the phase conductors) and $D_{min,ESW}$ (minimum distance between any phase conductor and shield wires). The constraints of the present problem are given in Equation 2.30

$$\begin{cases} D_{min}(\bar{t},\bar{\gamma},\bar{F}) \geq D^* \\ -30 \leq \gamma_w \leq +30 \quad \forall w = 1...N_w \\ D_{i,j}\left([\tau_{i,IS}^{(E)} \tau_{j,IS}^{(E)}], [\gamma_i^{(E)} \gamma_j^{(E)}], [F_i^{(E)} F_j^{(E)}] \right) = L_{IS} \\ \{i=1, j=2\} \; and \; \{i=2, j=3\} \end{cases} \tag{2.30}$$

where $\tau_{i,IS}$ are parameters in the optimization problem and represent the location of the IS device on phase i while L_{IS} is the length of the IS device adopted of the specific line.

3. ***Reduction of wire jump after sleeve shedding***

Concerning point 3, the present model applies an energy-based method to evaluate the maximum jump height of a conductor in case of sleeve shedding. The preliminary model adopted for the effects of interphase spacers is based on energy conversion equations as in [31] and on the multispan-model described above and already implemented in VULLINE tool [2][11]. Figure 2.11 indicates the scheme of the forces used for the modelling.

The following assumptions are carried out:

- the action of interphase spacers is only along vertical axis (no horizontal component of the force);
- under normal conditions (equal sags for the two phases) the spacer weight is equally distributed among the two spans. In case of shedding of the sleeve

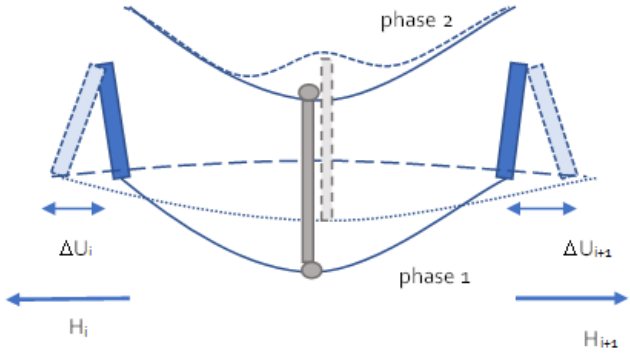


Figure 2.11: Scheme of the forces acting on a single interphase spacer

from the lower phase (phase 1 in Figure 2.11), the spacer applies at most a maximum force $F_{s,max}$ on the lower conductor, which opposes the upward movement of the lower phase;

- even if the interphase phasers along the span connect all the three phases together, it is assumed that the effects on the maximum jump of each phase are due to the spacers directly connected to the phase under study. We neglect mutual effects among all the three phases;
- in particular, from [25] it is assumed that the IS can be modelled as a linear spring which follows the Hooke's law as in Equation 2.31:

$$F_s = \frac{E_{IS} A_{IS}}{L_{IS,o}} \delta_{IS} \tag{2.31}$$

where $\delta$is the longitudinal extension, E_{IS} is the Young's modulus, A_{IS} is the cross-section of the IS device and $L_{IS,o}$ is the spacer rod's original length.

Under this assumption, the adopted energy conversion model in Equation 2.32 assumes that the work done by external forces (tensions from neighboring spans) determines an increase of the potential energy of the lower phase (the phase from which the sleeve detaches) and of the interphase spacer connected to this phase, due to vertical lift Δh, an increase of the elastic energy stored in the IS due to the compression action applied to the lower phase, but also an increase of the potential energy of the upper phase (phase 2 in the example in Figure 2.11).

$$\Delta U_i \cdot H_i + \Delta U_{i+1} \cdot H_{i+1} = \left(\frac{2}{3}WL + P_s\right)\Delta h + \\ + \left[\frac{W^2L^5}{128EA(f_0 - \Delta h)^2} - \frac{W^2L^5}{128EA(f_0)^2}\right] + \frac{1}{2}\frac{E_{IS}A_{IS}}{L_{IS,o}}\delta_{IS}^2 + \frac{2}{3}pL\Delta h^{'} \quad (2.32)$$

where E_{IS} is the Young's modulus, A is the cross sectional area of the conductor, W is the unitary linear weight of (unloaded) conductor, P is the unitary linear load of the (loaded) conductor and ΔU_i is the variation of the position of the *i-th* suspension of the line section between the condition before the sleeve shedding and after the sleeve shedding. It is assumed that the spacer is compressed by a quantity δ_{IS} when applying the force $\mathrm{F_s}$. The first member represents the work done by the external forces acting on the system under study (the tensions of the neighboring spans). The first term at the second member is the potential energy increase of the unloaded phase (phase 1) and of the IS of weight $\mathrm{P_s}$ the second term is the increase of the strain energy of the same phase, the third term represents the elastic energy stored in the spacer, the fourth term is the potential energy increase for the upper phase connected to the lower one. Based on simple geometrical formulas, it is derived in Equation 2.33.

$$\Delta h^{'} = (\Delta h - \delta_{IS})\sqrt{\frac{\Delta h - \delta_{IS}}{8f_0}} \quad (2.33)$$

where $\mathrm{f_0}$ is the sag of the loaded phase.

Equation 2.32 has two variables Δh and δ_{IS}: in order to be solved, an additional constraint is required: it is assumed that variable, δ_{IS} corresponds to the maximum force which can be applied by the spacer without breakage ($F_{s,max}$). Given this condition, Equation 2.32 is solved using the least square method. The condition of wet snow shedding is obtained by applying a model based on the balance between weight of the wet snow sleeve and the cohesive and adhesive forces of the sleeve as described in [11]. In particular, the maximum cohesive force, per unit length of the wire, is proportional to the thickness of the wet snow sleeve and depends also on the liquid content of the wet snow itself [32]. Additional modelling aspects are considered with reference to the IS devices. The weight of IS devices and the wind force on them are respectively added to the vertical and transversal components of the forces applied to the phase conductors and, as a consequence, to the tower supports and cross-arms. Specifically, for off-nominal conditions (wind speed different from 65 and 130 km/h used in the design standards) the wind action on the device is assumed proportional to the square of the wind speed. Given the typical IS configuration adopted in the Italian system, under nominal conditions, half of

the nominal wind force value is considered on top and bottom phase, while for mid phase the model assumes the entire value of the nominal wind-induced force.

Evaluation of OHL Failure RP's

The RP is the average time between two consecutive failures for the line. The vulnerability curves computed with the proposed model are combined with the climate curves, which give the probability of overcoming specific values of linear wet snow loads in a climatological period (e.g. a future horizon 2020-2030) to compute the RP for the outages of lines. Details on the methodology and its validation are in [2].

2.3.2 Case study

The present section discusses the results of the application of the proposed IS model to quantify the benefits of this countermeasure, in terms of increase of line failure RP's in [33].

Test system and simulation scenarios

The model is applied to a set of lines in the Northeast of the Italian EHV grid, frequently exposed to heavy wet snow loads. Terna has already started the experimentation of IS devices on these lines. Table 2.9 summarizes the simulations.

Table 2.9: List of described simulation cases

Sim ID	Description	Goal
Sim 1	Calculate the failure RP's of the OHLs under test, without any IS applied	Verify the criticality of such lines with respect to wet snow events
Sim 2	Application of IS devices and comparison of failure RP's before and after the deployment of the countermeasure, assuming a maximum cohesive pressure for the wet snow equal to 650 N/m2	Evaluate the benefits of IS device in increasing the failure RPs
Sim 2b	Application of IS on phases + Antitorsional (AT) devices on shield wires	Evaluate the benefits of combination IS+AT
Sim 3	Application of IS devices and comparison of failure RP's before and after the deployment of the countermeasure, assuming a maximum cohesive pressure for the wet snow equal to 200 N/m2	Evaluate the ability of IS devices to Limit the maximum jump height of the conductor after snow shedding

The maximum number and the position of IS devices are calculated based on TSO guidelines and depending on line span length and difference of the heights of

the attachment points. The simulations are performed using the mechanical data available for the lines from Terna database.

Sim 1: Base case

The Sim 1 is a base case where VULLINE has been run assuming that no IS devices are located in the OHL spans under study. The model adopted for the vulnerability assessment considers both the mechanical damages due to direct wet snow actions on the OHL subcomponents and the potential flashover due to reduced clearance distances as in [30]. Table 2.10 summarizes the failure return periods computed by VULLINE for the three lines: the average annual number of faults recorded on the analyzed set of OHLs during grid operation in the eight years (2000-2008), when no IS devices were deployed on these OHLs, is equal to *7/(3*8) = 0.292 faults/yr*, while the average annual number of faults computed by VULLINE is equal to *0.279 faults/yr*.

Table 2.10: Failure RPs for the OHLs set without IS application

Line ID	# of spans	OHL failure RP [Year]	RP_{min} among spans [Year]
Line 1	70	4.6	13.0
Line 2	131	2.6	10.8
Line 3	30	4.2	5.6

The base case confirms the criticality of the OHLs under study for problems related to the reduced clearance distances induced by unequal sags over the wires. Specifically, based on the spatial configuration of the attachment points for the wires of each span, the optimization problem in subsection IIII indicates if the most probable flashover condition occurs between two phases (two-phase faults) or between one phase and the grounded shield wire/s (one-phase to ground faults).

Sim 2: Application of IS devices

This scenario simulates the deployment of the maximum number of IS devices allowable on each span of the line, on the basis of Terna's installation guidelines. Moreover, a high cohesive force of the wet snow is assumed, which means that wet snow shedding occurs only at very high linear loads where other failure mechanisms become dominant (i.e. the mechanical damages of supports due to direct actions of wet snow). Figure 2.12 indicates the number of IS devices allowable on each span on the basis of Terna guidelines.

It is worth noting that based on the features of the span (length, difference of heights, etc.) not all the spans can be endowed with IS devices. Table 2.11

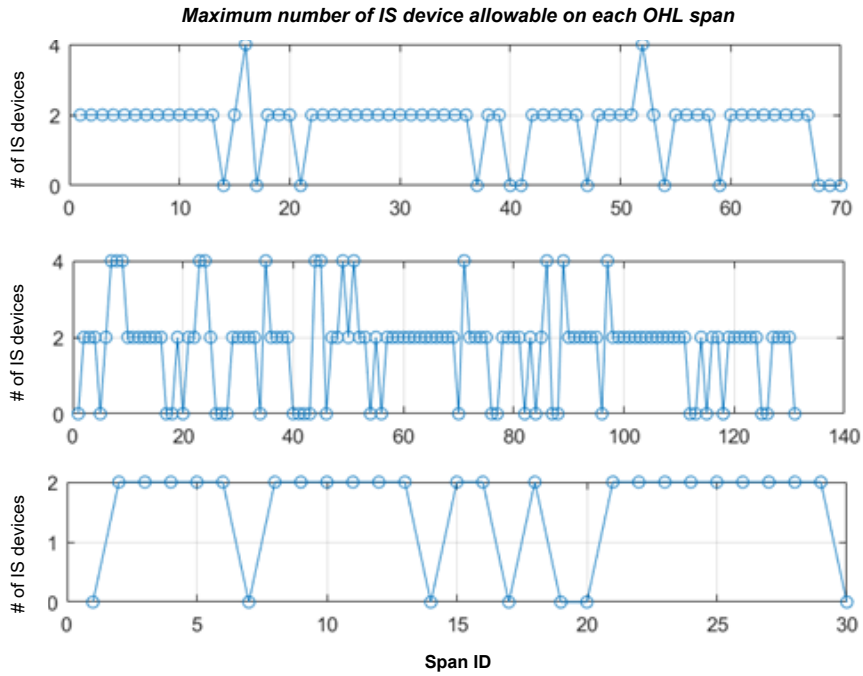


Figure 2.12: Maximum number of IS devices allowable over the spans of the three OHLs under test

reports the failure RPs of the OHL's where the maximum number of IS devices are deployed on all the spans where the deployment is feasible.

Table 2.11: Failure RPs for the OHLs set with IS application

Line ID	OHL failure RP [Year]	RP_{min} among spans [Year]
Line 1	11.4	30.9
Line 2	9.8	35.5
Line 3	44.5	111.5

Both the overall OHL failure RPs and the maximum RP's over the span increase wrt the base case. In particular, the maximum increase in the OHL failure RPs is for Line 3 where the total RP passes from 4.2 years to 44.5 years (close to the threshold of 50 years, used for the intervention prioritization in the CBA). Anyway, all the three lines keep a failure RP lower than 50 years. The reasons are manifold:

(i) some spans cannot be endowed with IS devices (e.g. the minimum RP for line 2 in the 3rd column of Table 2.11 is associated to span 126 at line 2 where no IS application is possible); *(ii)* also in case IS is applicable to the span, the vulnerability curve associated to shield wires (especially to those endowed with fiber optics) usually starts to show not negligible probabilities of failure at wet snow loads around 12 kg/m, not so rare in regions exposed to severe snowstorms. Figure 2.13 compares the failure RPs of the spans before (x-axis) and after (y-axis) the application of the IS devices: only the spans with both RPs below 500 years are plotted in the figure. It is worth noting that for some spans in all the three lines the post-intervention RP's still remain below 50 years, thus they can be considered critical for CBA analysis (see circle in Figure 2.13).

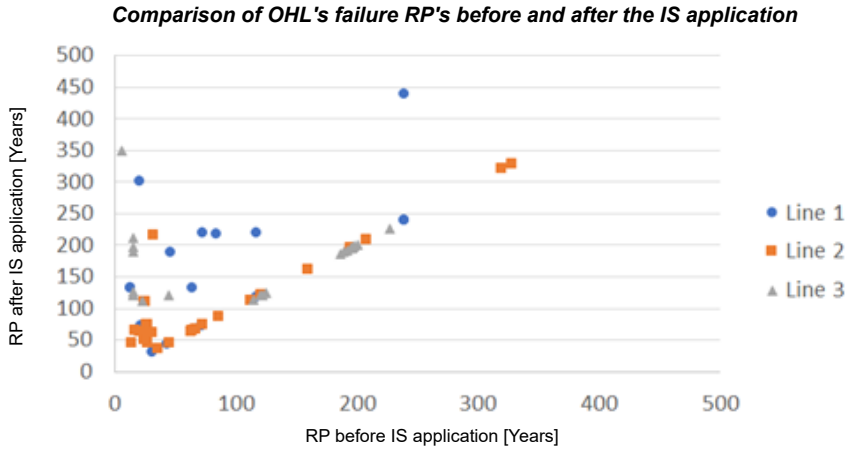


Figure 2.13: Comparison of failure RPs for the spans before (x axis) and after (y-axis) of the deployment of IS devices

The wet snow linear mass reduction on phase conductors due to IS application reduces the vulnerability of both conductors and tower supports but brings no benefit to shield wires which are still exposed to heavy sleeves. This suggests deploying also AT devices on shield wires to improve RPs.

Sim 2b: Applying a combination of IS and AT devices

The application of AT devices to the shield wires is done following the installation criteria from Terna illustrated in [34]. Specifically, the AT devices cannot be installed in the shield wires with fiber optics: the developed vulnerability model considers this aspect and does not apply any AT devices on such spans. On the

contrary, several AT devices can be installed on line 3, as shown in Figure 2.14 which represents the number of AT devices potentially installable according to the VULLINE model. All this leads to no failure RP improvements on lines 1 and 2, while line 3 undergoes a significant increment of failure RP from 44.5 to 58.3 years, which can be properly valorized in the CBA by Terna.

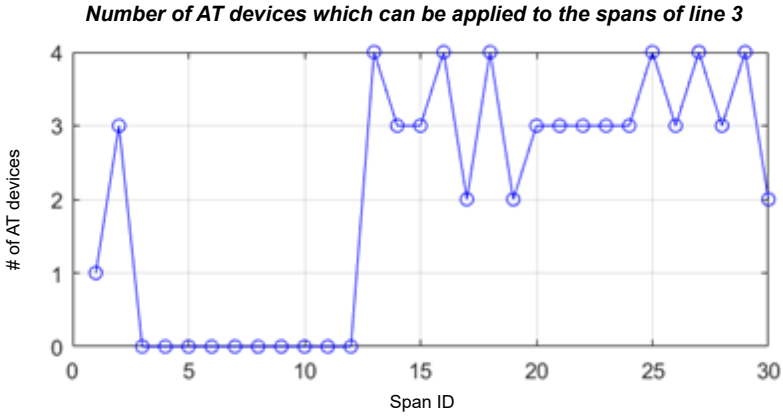


Figure 2.14: Number of AT devices installable on the spans of line 3 according to the VULLINE model

Sim 3: Applying IS devices in case of sleeve shedding

The present simulation assumes a reduced cohesive pressure of 250 N/m2 instead of 650 N/m2, which can occur in case of wet snow with a liquid content outside the typical values (around 20%). With a relatively low cohesive pressure, a lower amount of snow load can cause the sleeve shedding with a consequent jump of the unloaded phase. The benefits of the IS device consists in keeping the phases separate assuring an absorption of the released strain energy of the unloaded phase. As an example, Figure 2.15 reports the jump height of the lowest phase on the spans of line 1 without and with the installation of IS devices at 6 kg/m.

It is worth noting that many spans can experience jump heights of the lowest phase with values between 5 and 15 m when no IS are installed. On the contrary, in case IS devices are installed, they achieve a two-fold effect: on one side, they reduce the wet snow mass on the conductor. This means that many spans, that experienced the shedding of the sleeve in case of a "nominal" linear mass (i.e. nominal means "without IS" application) of 6 kg/m, are characterized by lower vertical actions in case of IS presence, thus they do not reach the shedding condition

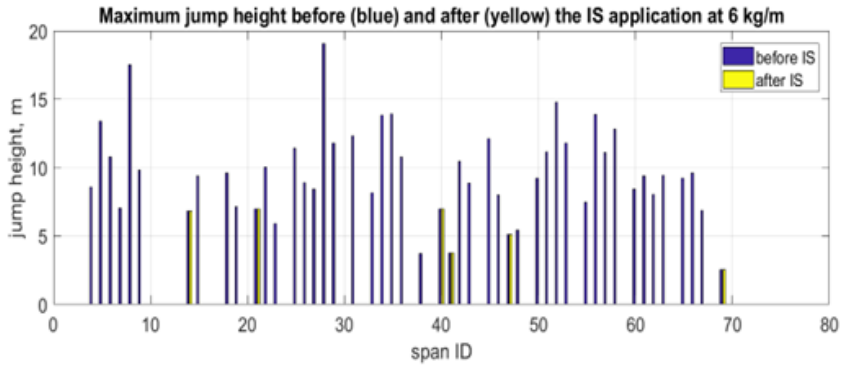


Figure 2.15: Comparison of maximum jump heights of the lowest phase after wet snow sleeve shedding on the spans of line 1, at 6 kg/m

(thus, jump height is equal to 0). On the other side, in case of higher "nominal" wet snow masses which can cause sleeve shedding the IS devices lead to smaller jump weights, thus favoring the separation of the phases. IS devices cannot be installed in some spans for which of course the yellow and blue bars in Figure 2.15 correspond to the same value.

2.3.3 Conclusions

An analytical model is presented for interphase spacers, a lightweight countermeasure to improve OHL response to wet snow and galloping phenomena, is developed. The model simulates the main beneficial effects of IS devices (increased torsional stiffness, reduced maximum jump height and phase separation), but also their weight and increased wind actions. Simulations allow the benefits of such measures to be quantified in depth in terms of increased RP of rupture per span. This metric can also be used to evaluate the best candidate spans where to place the devices. Further steps will consist in integrating these models into Terna's CBA for the prioritisation of future grid reinforcements.

Chapter 3

Operational Resilience in the Electricity Distribution Grid

3.1 Measurement problems in MV/LV cabin

In the evolutionary context that the Italian electricity grid is facing, both on the transmission and distribution side, the challenges of climate change and modernization of the grid, including generation, are being addressed. Changes in electricity generation and the shift to renewable sources can create instability within the grid. It becomes crucial to assess short-term operational resilience therefore, in order to have a more modern and efficient infrastructure.

In order to obtain an increasingly resilient grid, it is essential to use diagnostic tools that are based on the analysis of data coming from the field and affected by the least possible error.

If a MV/LV substation is seen as a user node of the network, it is possible to exploit the data that comes from it for various purposes, including, for example, analyzing the health status of that substation and in what conditions it is operating.

It is therefore becoming increasingly important to obtain precise and accurate measurements in order to monitor the health of the electricity grid itself and beyond. Inside MV/LV substations, however, several factors come into play that make the measurement may not be accurate, including stray magnetic fields, sensor positioning errors and more. The objective, therefore, is to investigate the measurement problems inherent to the substations and to understand how these measurements also affect the efficiency of the network, for example on voltage control. In fact, these measurements can also be useful for triggering voltage controls, such as distributed online voltage control. This controller, however, will be affected

by all measurement uncertainties at the measurement sensing point. It is therefore essential to understand the issues that influence these measurements.

3.1.1 Rogowski coil

The Rogowski Coil (RC) [35], named after the German physicist Walter Rogowski, is a transducer capable of measuring current, the operation of which is based on Ampere and Faraday's laws. Thanks to the development of electronic devices, there has been an improvement in transducer technology, allowing optimal measurement even of currents with low amplitude levels. One of the main advantages of the RC relates to the absence of a ferromagnetic core, a construction parameter that allows the construction of a linear characteristic: also thanks to the accuracy of electronic devices, the measurement range of the RC can vary between mA and MA. This transducer is also low-cost compared to other measurement methods, which is why the RC can be said to be a competitive solution for measuring high-current transients. Furthermore, if the coil has its ends joined, it can take on any shape: Ampere's law states that the integral over a closed circuit of the magnetic field is equal to the current, regardless of the shape of the circuit. This aspect confirms the physical flexibility that the Rogowski coil possesses as a current transducer, making it the best solution in situations where other devices, such as measuring transformers, do not have the desired flexibility. However, the nature of the RC's measurement method, which measures the derivative of current, limits its use for measuring AC currents only.

Summing up some advantages:

- resistance to high overloads without being damaged;
- measurement of currents over a wide range, without saturation of the ferromagnetic core and consequent formation of a non-linear characteristic;
- ease of use due to flexibility and light weight;
- low cost;
- non-intrusive nature, with no energy drawn from the main circuit;
- wide bandwidth, in a range from 0.1 Hz to 1 GHz;
- excellent transient response;
- safety, guaranteed galvanic isolation with the main circuit.

Whereas the disadvantages:

- low accuracy;
- dependence of accuracy that may vary depending on the positioning of the coil with respect to the conductor;
- does not perform DC current measurements.

An example of a RC is shown in Figure 3.1.

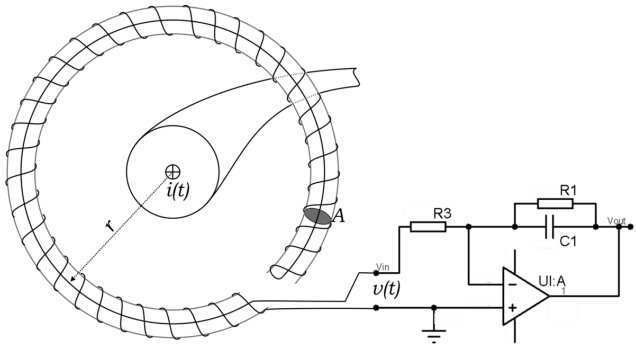


Figure 3.1: Example of RC with operational amplifier

A typical Rogowski coil consists of toroidal windings surrounding the current path With reference to Ampere's law, the relationship between the current flow through the Rogowski coil and the magnetic field is as follows in Equation 3.1:

$$I(t) = \frac{1}{\mu_0} \oint \vec{B}(t) d\vec{s} \tag{3.1}$$

Where I is the current, μ_0 is the vacuum magnetic permeability, s is the path of the toroid and B is the magnetic field.

Considering the constant coil cross-section and homogeneous coil distribution per unit length, it is possible to exhibit a relationship between the induced voltage u at the terminals of the Rogowski coil and the current I via Faraday's law reported in Equation 3.2:

$$u = \frac{d\Phi}{dt} = \oint \vec{B}(t) d\vec{A} = \frac{A}{s} \mu_0 I(t) \tag{3.2}$$

Where A is the cross-section and s is the number of turns per unit length. In order to derive the current value from the induced voltage, it is necessary to use an integrator block to be applied to the signal at the RC terminals.

Signal hardware integration techniques

There are several techniques for integrating the signal with hardware circuits, including:

1. Integrator with RC circuit;
2. Integrator with operational amplifier.

1. ***Integrator with RC circuit***

In this case, the self-inductance of each wire is modelled as L. The values R and C are the resistance and capacitance, respectively, that make up the integrator circuit. The equivalent circuit of such an integrator is shown in Figure 3.2. The potential difference will be expressed in Equation 3.3, from which the I value can be derived.

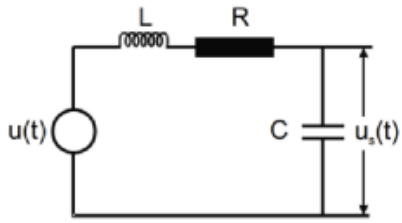


Figure 3.2: Equivalent circuit of an RC integrator using a single turn

$$u_s(t) = \frac{1}{C}\int_0^t i\ dt' = \frac{1}{RC}\int_0^t u(t')\ dt' = \frac{A\mu_0}{sRC} = \mu_0 \frac{NA}{S_m}\frac{1}{RC} I(t) \tag{3.3}$$

Where N is the number of turns, A is the cross-section of the RC, and S_m is the length of the RC.

2. ***Integrator with operational amplifier***

One of the inherent advantages of the op amp integrator is noise reduction due to low-pass filter behaviour, which is important for high-precision measurements. An hardware integrator is appropriate for high frequencies ($>$ 100 MHz), while an integrator based on an operational amplifier is useful for low-frequency measurements ($<$ 100 MHz). The perfect integrator must fulfil several requirements: not only must it have a very wide bandwidth, but it should have a time constant many times larger than the main circuit constant. The hardware integrator has

several limitations: for example, when measuring at the mains frequency (50 - 60 Hz), both R and C must have high values. In addition, the supplement may be affected by parasitic capacities. Because of these problems, the integrator with operational amplifiers is preferred for mains frequency measurements. An example of this integrator and it's frequency characteristic is shown in Figure 3.3.

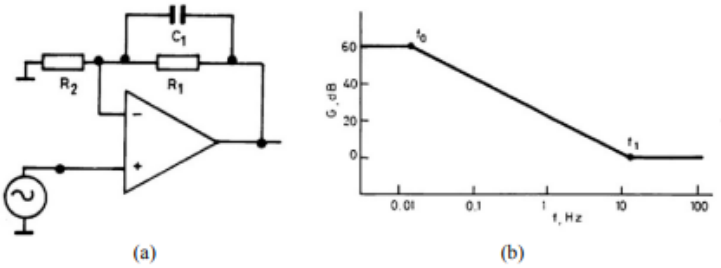


Figure 3.3: (a) Operational Amplifier. (b) Frequency Characteristic

Signal software integration techniques

Another signal integration technique is the software technique, which consists of using a microprocessor-based device with an analogue-to-digital converter to integrate the signal output from the RC. In this method, a signal processing software operates as an integrator: the use of an additional block operating as a digital filter can result in improved output [36]. Figure 3.4 shows a block diagram that best represents the digital integration process. This is a particularly appropriate method for medium frequencies. Although the analogue integrator is simple to realise, it presents problems consisting mainly in the sensitivity to temperature and drift over time that the integrator components may suffer, effects that cannot be compensated for in any way. In contrast, digital integrators are developed on numerical methods but have a higher uncertainty on signals containing harmonic orders at high frequencies. Furthermore, digital integration algorithms have a significant measurement error when the signal frequency fluctuates in the margins of the network frequency. One option to improve the response of digital integration is to increase the sampling frequency but this causes an increase in cost in hardware and computational analysis.

There are several techniques for integrating the signal with hardware circuits, including:

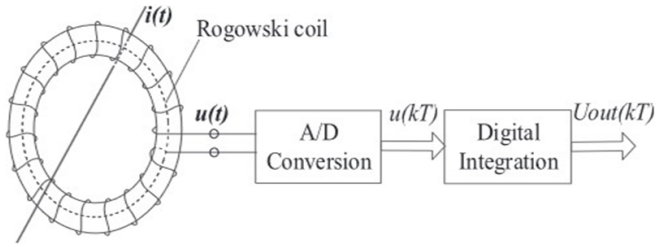


Figure 3.4: Schematic diagram of a RC with digital integration

1. Newton - Cotes algorithm [37];
2. Recursive filter algorithm [38].

1. ***Newton - Cotes algorithm***

It is the most widely used algorithm for the integration process of the RC. The first-order transfer function is given in Equation 3.4.

$$H_T(z) = \frac{T}{2}\frac{1+z^{-1}}{1-z^{-1}} \tag{3.4}$$

Considering a defined sampling period T, it is possible to transform the Equation 3.4, according to the Z-transform, obtaining the Equation 3.5.

$$H_T(j\omega_i) = \frac{T}{2}\frac{1+(e^{i\omega_i})^{-1}}{1-(e^{i\omega_i})^{-1}} \tag{3.5}$$

Where $z = e^{j\omega_i}$, $s = j\Omega$, $\omega_i = \frac{2\pi}{N}$ is the digital angular frequency, $N = \frac{f_s}{f_i}$ is the number of sampling points per period, f_i is the signal frequency and $\Omega_i = T\omega_i$ is the analogue angular frequency.

The error of the digital integration algorithm depends on the sampling and signal frequencies, but is low at network frequencies: however, higher harmonic orders increase the frequency content of the signal. This introduces measurement errors for distorted voltage or current waveforms.

2. ***Recursive filter algorithm***

Filters are tools used to extract information from signals through a process that separates desired and unwanted information with a frequency dependency [38]. There are two types of filters: non-recursive, which are the simplest, and recursive, which are more complex and used particularly in the field of signal processing.

The T-PMR [39] is a device developed by Tesmec for the monitoring and protection of MV/LV substations. In particular, currents are monitored through the use of RC and a recursive filter for signal integration, shown in Figure 3.5. The represented recursive IIR algorithm is based on a sampling frequency of 256 points/period. The numerical frequency cut-off is fixed through a 0.5 Hz pole, with 40 dB attenuation and zero phase shift at 50 Hz. Consequently, the signal must be amplified by a factor of 100 after filtering.

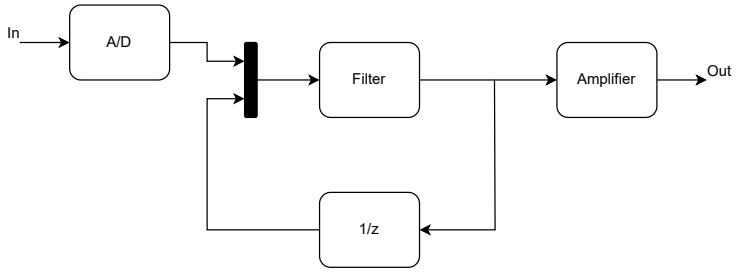


Figure 3.5: Recursive filter of T-PMR

The function representing the filter as reported in Equation 3.6:

$$y(k) = b \cdot x(k) + (1 - b) \cdot y(k - 1) \tag{3.6}$$

Where b is cut-off factor for sampling at 256 points/period, calculated using the Equation 3.7:

$$b = \frac{2\pi \cdot 0.5}{256 \cdot 50} \tag{3.7}$$

And *x(k)* is the sample at the current step multiplied by the cutoff factor, *y(k)* is the sample integrated at the previous step. Next, the T-PMR processes the signal through a filter to eliminate the DC offset and a low-pass in the 2 kHz band.

Standard for measurements made with RC

In order to carry out the measurements correctly and, above all, process the data using a well-defined standard, we refer to the indications expressed in standard CEI EN IEC 61869-10 [40]. This part of IEC 61869 deals with defining standards for passive current transformers with low power, analogue output and electrical measuring instruments or electrical protective devices with nominal frequencies between 15 and 100 Hz, thus also RC. This standard defines the percentage error of measurements, in amplitude terms, made with RC, according to Equation 3.8.

$$\epsilon_{\%} = \frac{K_r U_s - I_p}{I_p} \cdot 100 \tag{3.8}$$

Where K_r is transformation ratio, I_p is the RMS value of the primary current and U_s is the RMS value of the secondary voltage.

The standard defines that for a measurement made by an RC, the accuracy class is defined by the highest permissible percentage error with current primary and output data. The accuracy class standards are and maximum permissible amplitude errors are given in Table 3.1.

Table 3.1: Error limits for RC

Accuracy class	Ratio Error [±%]				
	0.01 I_{pr}	0.05 I_{pr}	0.2 I_{pr}	I_{pr}	KI_{pr}
0.1	-	0.4	0.2	0.2	0.1
0.2	-	0.75	0.35	0.2	0.2
0.2 s	0.75	0.35	0.2	0.2	0.2
0.5	-	1.5	0.75	0.5	0.5
0.5 s	1.5	0.75	0.5	0.5	0.5
1	-	3	1.5	1	1
3	-	-	4.5	3	3

Due to the linear characteristic, the RC can be used within a wider range of primary current values. Standard values for a primary current extension factor are 5-10-20-50-100 A.

Furthermore, thanks to IEC 61869-6:2016 [41], the limits of accuracy on harmonics are defined, which are applicable during the test procedures considered by IEC TC 38.

The regulations also provide standards for the positioning of the conductor within the RC. In particular, ideal tests are defined, performed with the primary conductor centred and perpendicular to the RC and without the influence of an external current-carrying conductor. In Figure 3.6 shows three levels of primary conductor positions for which accuracy is required, where the ideal condition for a measurement with only the inner conductor and centred is PF = 0.

3.1.2 Simulation setup

Experimental setup

Figure 3.7 shows a block diagram depicting the measurement setup used during the experimental phase of the proposed work. Specifically, the Pacific Smart Source

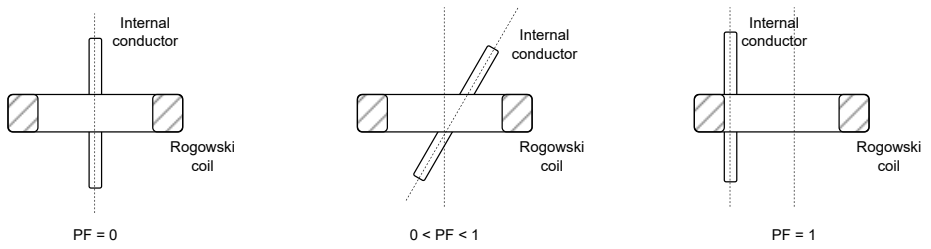


Figure 3.6: Position of primary conductor according to position factor PF

[42] is a generator used to deliver a voltage/current with high precision: the current is measured by the three RC and the Tektronix A621 current clamp [43], which will be used as a reference. To obtain the desired currents, a variable resistive load is inserted into the circuit. The output signal of the RC is acquired and processed via hardware and software integration by the T-PMR, while the output signal from the clamp is acquired by the TiePie HS5 [44] to be used as a reference. Subsequently, the data extracted from the T-PMR and TiePie are acquired from the PC using proprietary Tesmec software and a Matlab script for signal acquisitions via TiePie, respectively. The RC under test are prototypes made by the company Tesmec, with a transformation ratio of $k_t = \frac{1kA}{100mV}$.

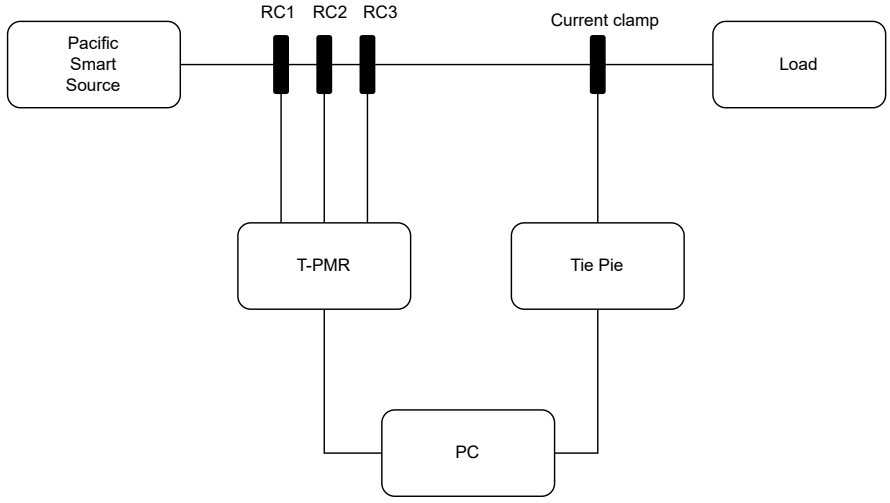


Figure 3.7: Measurement setup block diagram

Simulation parameters

As shown in Table 3.1 different percentages of the test current are used. The precise choice of I_{pr} is therefore necessary in order to avoid having currents that are too low to measure in the case of 5% I_{pr} or currents that are too high for the entire measuring system to withstand in the upper end $K_r I_{pr}$, where the proportionality factor K_r must also be fixed. Ideally, the best option would be to bring the measurand closer to the range of the instrument, i.e. the RC, to decrease the systematic error caused by the range: however, this is very difficult to achieve in a testing environment, as the coil range is 1000 A. Delivering an amount of current of this order of magnitude is not easy to achieve, which is why the magnetic field is increased in proportion to the current delivered with a test cable with 16 coils. In addition, the maximum power dissipation of the resistive load inserted within the setup is 30 A. Another limitation concerns the capacity of the cables used for the connection between the Pacific and the load, on which the coils and the current clamp take measurements, which is 15 A. The current values delivered by the Pacific and increased in terms of magnetic field are shown in the Table 3.2.

Table 3.2: Test currents and multiples

$\mathbf{I_{pacific}[A]}$	$\mathbf{I_{pacific}[A]}$	$\mathbf{I_{pacific}[A]}$	$\mathbf{I_{pacific}[A]}$
0.41	1.66	7.6	14.7
5% $\mathbf{I_{pr}}$ [A]	**20% $\mathbf{I_{pr}}$ [A]**	**$\mathbf{I_{pr}}$ [A]**	**$\mathbf{I_{pr}}$ [A]**
6.8	26	121	235

Once the currents have been defined, we distinguish between the two options displayed: in one part, the current delivered by the Pacific is purely sinusoidal; in the other part, the current is distorted. In the first case, the Pacific will totally inject a 50 Hz sine wave with an RMS value equal to the various I_{pr} percentages shown in the Table 3.2.

Considering instead the distorted current, the Pacific is capable of generating a maximum number of 50 harmonics. The percentage harmonic coefficients, derived from the ratio between the harmonics and the fundamental, and chosen on the basis of the EN 50160 standard [45] in which harmonic limits are defined, are ordered in Table 3.3. The harmonics from the $29th$ to the $50th$ are null and are not shown in the table.

Thirty acquisitions are made, which is high enough to reduce the effects of random phenomena. Each acquisition, for each current level and each type of position, has an observation time of 200 ms. The frequency resolution is 5 Hz.

Table 3.3: Percentage harmonic coefficients for distorted current

Harmonic order	Coefficient [%]	Harmonic order	Coefficient [%]
1	100	15	0
2	0.146	16	0
3	0.219	17	0.014
4	0.032	18	0
5	1.938	19	0.054
6	0	20	0
7	0.362	21	0
8	0	22	0
9	0.212	23	0.036
10	0	24	0
11	0.286	25	0
12	0	26	0
13	0.117	27	0
14	0	28	0
15	0	29	0.002

This is a high enough value to avoid an imperfect distribution of harmonic tones in the frequencies close to the fundamental (50 Hz), caused by a small but perceptible variation in the mains frequency. In this way, the harmonic tones present between 45 Hz, 50 Hz and 55 Hz are more accurately distributed in their actual frequencies.

Signal processing

In order to analyze the data obtained from the coils and the current clamp appropriately, a processing step was required, shown in Figure 3.8. During the first phase, the signal to be emulated by the Pacific, sine or distorted, is chosen. In the second phase, the data from the coils, processed first by the T-PMR, are acquired as .CFG files (COMTRADE files). Subsequently, the .CFG files are converted into .CSV files. At the same time, the reference signal acquired by TiePie is acquired in .CSV files. Then, when there is a purely sinusoidal voltage regime, the rms values of the currents integrated in hardware or software mode via the T-PMR are taken; the same step is also performed for the reference currents, which are subjected to numerical calculation of their RMS value. Consequently, the percentage error is calculated via the Equation 3.8 where $K_r U_s$ is the RMS value of the current under test and I_p is the value of the reference current. This is repeated for all the different test currents, with hardware and software integration and with the three different coil positions, as indicated in standard [41] and [40].

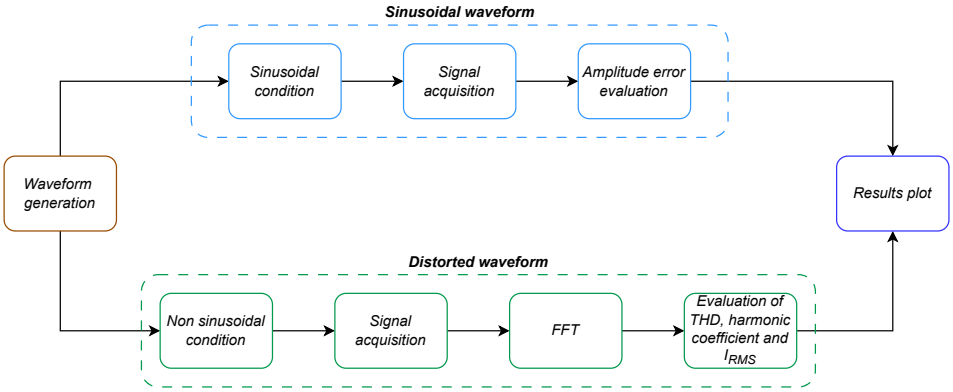


Figure 3.8: Block diagram of signal processing

With regard to measurements with distorted test currents, the processing requires several steps. The first processing involves calculating the RMS of the currents from the coils and the reference currents. As in the previous case, the percentage error between the output currents from the T-PMR and TiePie is calculated according to the formula 3.8. The second processing consists of calculating the Total Harmonic Distortion (THD) of the currents involved, as shown in Equation 3.9.

$$THD = \frac{\sqrt{\sum_2^\infty (I_h)^2}}{I_1} \cdot 100 \tag{3.9}$$

Where I_h is the value of the h-th harmonic of the current and I_1 is the fundamental value of the current at 50 Hz.

The THD of the reference current delivered by the Pacific and the hardware and software integrated currents of all coils, in all three operating positions and with all percentages considered of the test current, were calculated, as for the sinusoidal currents.

Finally, the ratios between the various harmonic tones and the fundamental were derived, taking as reference all harmonics present in the current delivered by the Pacific. This harmonic coefficient is derived from the Equation 3.10:

$$\alpha_h = \frac{I_h}{I_1} \cdot 100 \tag{3.10}$$

As with sinusoidal and distorted currents, coefficients are calculated for all current levels and all positions of one of the three coils, compared with the harmonic ratios set by Pacific.

3.1.3 Results

The limits taken into account by the standard and shown in the Table 3.4 are accuracy class 3 and accuracy class 1, for both emulated signal conditions. Tests were carried out for both regimes, one for:

- each position of the RCs: central and perpendicular to the cable (PF0), Coil adjacent to the cable (PF1), coil inclined 45° to the cable (PF45), as shown in Figure 3.6;
- different current value, defined in [41] [40];
- two type of signal integration: hardware and software.

As described in Chapter 3.1.2 were evaluated:

- percentage error between reference current and measured current with RC under test;
- THD;
- harmonic coefficient described in Equation 3.10.

For ease of reading, results have been reported for a single RC under test.

Table 3.4: Percentage amplitude error limits for accuracy levels expressed by the standard

	20% I_{pr} [%]	**I_{pr}**[%]	**K·I_{pr}**[%]
Acc_3	4.5	3	3
Acc_1	1.5	1	1

Sinusoidal condition

From the Table 3.5, it can be seen that the percentage error into accuracy class 3, defined in Table 3.4, tending to remain uniform for the three percentages of test current measured. The first consideration we can obtain from this test is the property of the percentage error to always be negative: this implies that the coils underestimate the rms value of the measured currents with respect to the current clamp. In particular, for PF45, the percentage error has the highest value, comparing it to the other two positions analyzed. Comparing the two integration techniques, however, it can be seen that in all positions, software integration always

has a smaller error. With regard to the level of current used, however, the higher you go with the current, the more the error tends to decrease as you approach the full scale of the coils. Ideally, by raising the current further, which is difficult to achieve in a laboratory environment, a very low error value could be obtained.

Table 3.5: Percentage amplitude errors for sinusoidal current as a function of: position, integration technique and current level

Position	**Signal integration**	**Error [%]**		
		20% I_{pr}	**I_{pr}**	**K·I_{pr}**
0	Hardware	-1.5	-1.4	-1.4
	Software	-1.5	-1.3	-1.4
1	Hardware	-1.3	-0.9	-0.5
	Software	-1.2	-0.8	-0.4
45	Hardware	-1.8	-1.6	-1.6
	Software	-1.7	-1.6	-1.5

Distorted condition

For the distorted condition, the results are shown in the Table 3.6. Just as for the sinusoidal regime, the same considerations can be derived. In particular, position 1 appears to be the one with the lowest error, in all cases analysed the software integration has a more accurate response than the hardware and for high currents the error is lower.

In addition, THD was also evaluated, which is shown in Table 3.7. It shows that the value is constant for each position of the RC under test at the same current value, but by increasing the current value, the THD evaluated with RC approaches that of reference.

Figure 3.9 shows the percentage harmonic coefficients, calculated by Equation 3.10, for RC under test at position PF0. In particular, focusing on the hardware and software responses for the various harmonics, we divide the harmonic spectrum into three parts:

- *2^{nd} to 4^{th} harmonic order*: the integrations respond differently depending on the harmonic considered. For the second harmonic, the software integration has a response closer to the reference than the hardware integration; The third and fourth harmonics have a better hardware integration for the currents at *20% I_{pr}*, while the software is better for I_{pr}. For $K{\cdot}I_{pr}$ the answers are almost equal.

- *5^{th} to 11^{th} harmonic order*: software integration produces lower harmonic coefficients than hardware integration and closer to the reference.
- *12^{th} to 23^{th} harmonic order*: software integration lowers harmonic coefficients compared to hardware integration, being further away from the reference.

Table 3.6: Percentage amplitude errors for distorted current as a function of: position, integration technique and current level

Position	**Signal integration**	**Error [%]**		
		20% I_{pr}	**I_{pr}**	**K·I_{pr}**
0	Hardware	-1.3	-1	-0.5
	Software	-1	-0.9	-0.5
1	Hardware	-1	-0.9	-0.4
	Software	-0.8	-0.6	-0.4
45	Hardware	-2	-1.9	-1.5
	Software	-2	-1.8	-1.5

Table 3.7: THD for distorted current as a function of: position, integration technique and current level

Position	**Signal integration**	**THD [%]**			
		Reference	**20% I_{pr}**	**I_{pr}**	**K·I_{pr}**
0	Hardware	2.02	2.35	2.18	2.16
	Software	2.02	2.34	2.18	2.16
1	Hardware	2.02	2.35	2.18	2.16
	Software	2.02	2.33	2.18	2.16
45	Hardware	2.02	2.35	2.18	2.16
	Software	2.02	2.34	2.18	2.16

3.1.4 Conclusions

The analysis that has been carried out in this section is useful for understanding the measurement problems for current that persist in MV/LV transformer rooms with the use of RC. It can be seen from the results obtained, that it is fundamental to respect the correct positioning of the coil inside the cabin, considering the bus bar in which current passes to be as centred as possible with respect to the coil. Fundamental will be the calibration of the signal integration system, whether a hardware

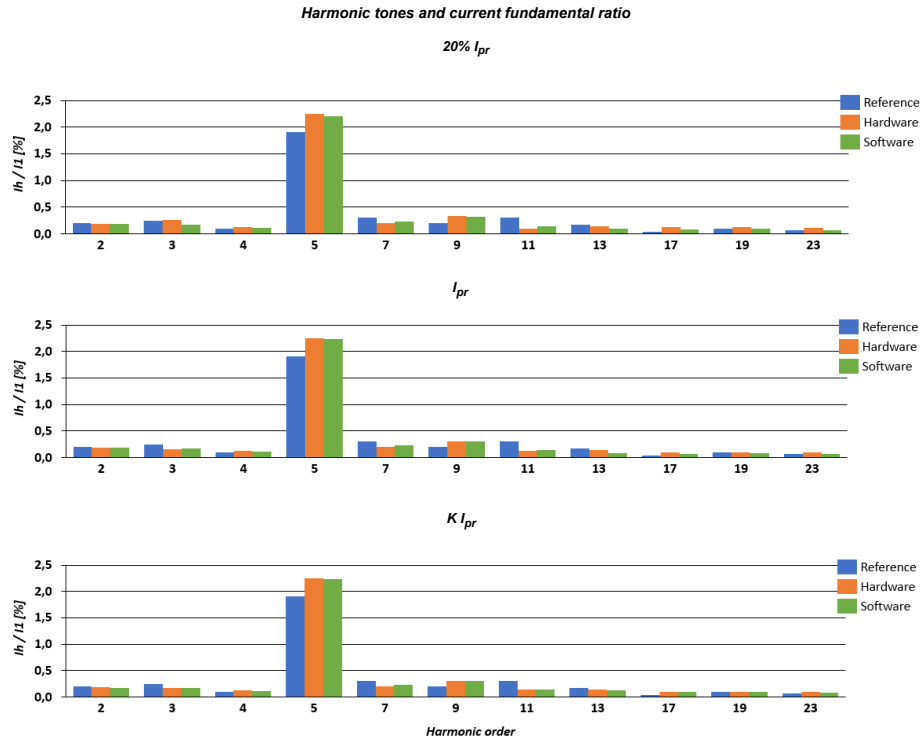


Figure 3.9: Harmonic coefficient for RC under test at PF0

or software integration technique is used, in order to minimise the measurement and reconstruction error of the waveform in question. Faithful reconstruction of the current waveform can be used in smart energy applications in order to modernise the electrical distribution network. Through the use in MV/LV substations of monitoring devices developed by Tesmec, such as the T-PMR, it is possible to exploit not only current measurements but also voltage measurements, useful for example for the implementation of a voltage control algorithm, increasing the number of usable measurements (and therefore coming not only from PMUs but also from T-PMR) and accuracy. It is therefore essential to understand the accuracy of these measurement systems in order to better understand how to calibrate the voltage control algorithm.

3.2 Impact of measurement uncertainty on distributed voltage control

Nowadays, electricity distribution networks around the world are taking on a major change caused by the large presence of renewable resources and new electrical loads to be handled such as charging stations for electric vehicles, heat pumps, etc. The combination of these new resources and electrical loads is named as Distribution Generation (DG). Traditional distribution networks are evolving towards more modern and intelligent smart grids [46]. The massive presence of DG can cause problems to the existing infrastructure, bringing it to the operational limits of correct functioning, causing overloads and voltage problems [47]. Control systems, such as Distribution Management Systems (DMS), rely on knowledge of the state of the grid, in terms of voltage profiles and current or power flows. Hence, it becomes crucial to have a widely spread accurate level of measurements.

However, when measurements are performed on the field, great attention must be paid to sensor-related measurement accuracy, which impacts voltage regulation [48]. For example, in the case of a Distribution System State Estimation (DSSE), the influence of the measurement accuracy in the performance of the estimation algorithm has been widely analyzed [49], in particular considering the measurements acquired through Phasor Measurements Units (PMU) [50]. Similarly, voltage control algorithm can suffer from measurement errors, as described in [51]. However, with respect to the DSSE, an extensive analysis of the effects of the error measurements is still missing, in particular when considering distributed configuration of the control algorithm. For this reason, this research intends to investigate the effects of measurement errors on the distributed voltage regulation algorithm, where the control problem is solved by the coordination of agents of a network. Such implementation has become very appealing in recent years, due to its robustness and flexible structure [52]. The present research aims at analyzing the effect of error of the voltage measurements on a distributed online voltage control using a container-based implementation presented in [53]. Different level of accuracy and reporting rate will considered, taking into account the metrological features of three PMU devices available on the market.

3.2.1 Distributed Online Voltage Control

The distributed voltage control considered in this research refers to formulation described in [53], which is based on the application of the dual ascent steps on the dual variables and the minimization of the primal variable, presented in [52]. As described in [53], a container-based implementation has been considered to replicate a Cyber-Physical System (CPS) where the control are instantiated in the

software containers. The role of the software containers is to replicate the distributed implementation of the voltage control strategy using a flexible solution that sits between running the application in real hardware and implementing it in a virtualized environment. The communication among the software containers is implemented employing a python library, namely Data Management (DMU) [54], which provides a easy to use solution to form peer to peer connection between the control nodes. With the DMU, the user can define a data model where the data elements are defined by the user and can be elaborated by the program. The DMU is also an action-reaction based tool, which means that if an update action is performed on a specific part of the data structure, an event may be triggered. The communication protocol used to interface the software containers is HyperText Transfer Protocol (HTTP), however DMU additionally includes Message Queuing Telemetry Transport (MQTT). The resultingCPS is described in Figure 3.10: it shows how grid topology and the position of the DGs are mapped into a communication graph $\mathcal{G}$, where each control node communicates with its electrically close neighbors.

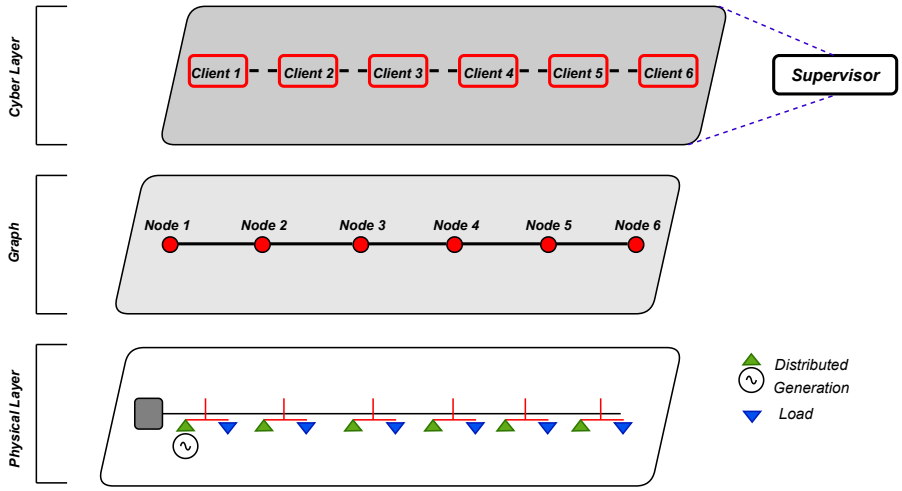


Figure 3.10: Structure of the CPS system

In the proposed approach, the intelligent nodes, defined as *Client*s, implements the distributed control and they are monitored by an external software container, defined as *Supervisor*, which manages the registration of the clients and creates the communication graph. When a new *Client* is instantiated, the *Supervisor* updates the list of the registered *Client*s. Once the list is updated, the *Supervisor* recalculates the control parameters and sends the new values to the *Client*s together

with the address of the neighbors to which each control node should communicate, as described in Figure 3.11.

As described in [53], the only role of the *Supervisor* is to configure the peer to peer communication between the *Client*, therefore it does not perform directly the control algorithm. This allows the privacy of the data exchanged to be preserved within the neighbors and it guarantees the robustness of the distributed implementation. The communication among the *Client*s is triggered by the value of the resulting Lagrangian multipliers calculation. Only when the calculated value is greater than zero, it is transmitted to neighboring nodes. This condition-triggered feature of the algorithm additionally underpins the choice of employing the DMU as a communication tool for the proposed control strategy.

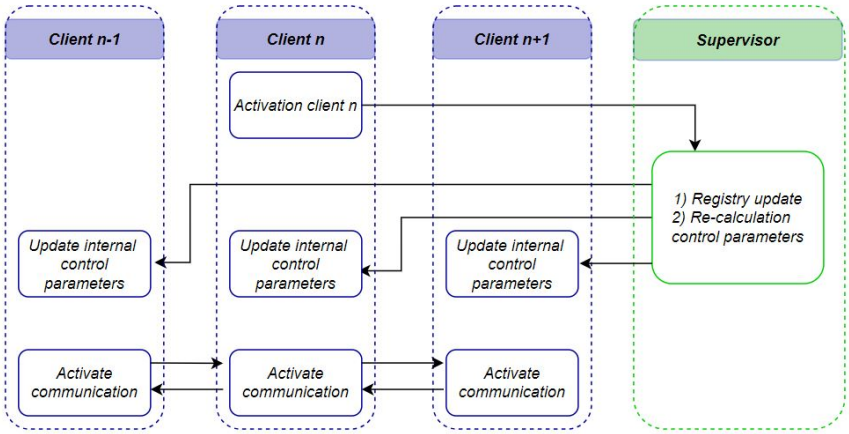


Figure 3.11: Activation of the new *Client*

3.2.2 Simulation Setup

Grid Configuration

The electrical grid that was simulated for the tests carried out is shown in Figure 3.12. In particular, the grid is composed of a single feeder with 6 nodes, where the DG is present only on node 1 and the electrical loads are present in all nodes.

The generation used is formed by a Photovoltaic Panel (PV) with the generation curve shown in Figure 3.13. An example of the absorption profile of the electrical loads used for the test is reported in Fig 3.14.

The electrical parameters of the line used in the simulation phase are summarized in Table 3.8. In particular, this Table reported the ID of the electrical node,

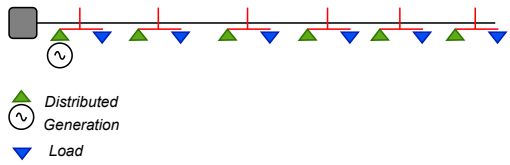


Figure 3.12: Simulation grid

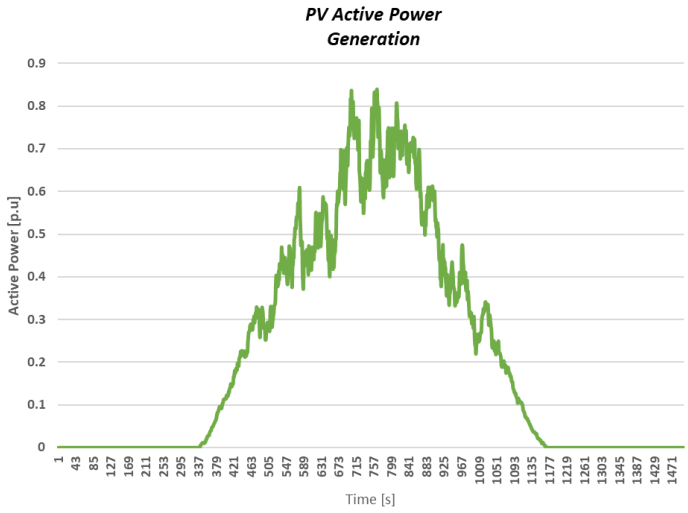


Figure 3.13: PV Active Power Generation

start and end point of the stretch of line in question with the relative values of Resistance (R) and Reactance (X), both reported in p.u..

Table 3.8: Electrical Parameters of the Simulated Grid

Node ID	Start Node	End Node	R [p.u]	X [p.u]
1	1	2	0.00040	0.00317
2	2	3	0.00108	0.00040
3	3	4	0.00042	0.00016
4	4	5	0.00087	0.00033
5	5	6	0.00093	0.00035

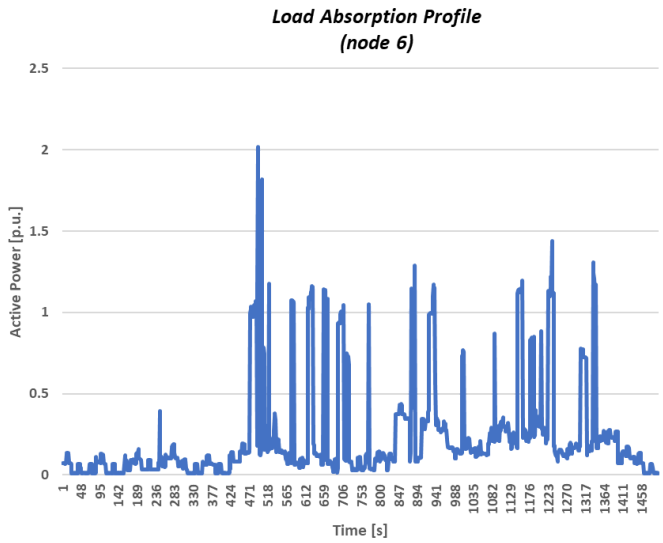


Figure 3.14: Absorption Profile of the Electrical Load at Node 6

PMUs Metrological Features

Nowadays, many PMUs are available on the market which are going to differentiate, for example, in terms of accuracy of the voltage measure, that impact on the voltage control.

In Table 3.9 some main characteristics of the PMUs used for the analyzes carried out in this research are reported, among which the model, the accuracy of the voltage measure and the reporting rate expressed in frame per seconds.

Table 3.9: Main Features of Some Commercial PMUs

Brand	**Model**	**$\mathbf{Acc_V}$%**	**Reporting Rate [fps]**
Nexus[55]	1500+	0.1	10-25-50
Siemens[56]	SIMEAS R-PMU	0.25	10-25-50
ABB[57]	RES670	0.3	10-25-50

Methodology and Simulation Parameters

Considering the Voltage Accuracy (Acc_V) as a noise that is added to the generated voltage, there will be fluctuations of the same within a range determined by the

measurement accuracy in question. In order to reduce these fluctuations, the proposal developed in this paper is to average N values coming from the PMU before sending them to the voltage control, thus allowing to have a more stable voltage, where N is the number of Reporting rate (fps).

The number of fps indicates the data transmission capacity that a given PMU has. The higher the value, the more data will be transmitted every second.

Table 3.10: Simulation Parameters

PMU	**Acc_V%**	**P_{GEN} [p.u]**	**fps**
-	0	1.0	10-25-50
Nexus[55]	0.1	1.0	10-25-50
Siemens[56]	0.25	1.0	10-25-50
ABB[57]	0.3	1.0	10-25-50
-	0	1.1	10-25-50
Nexus[55]	0.1	1.1	10-25-50
Siemens[56]	0.25	1.1	10-25-50
ABB[57]	0.3	1.1	10-25-50

The Table 3.10 shows all the simulations carried out on the basis of the different characteristics analysed. In particular, in this research we simulated different level of Acc_V, different level of generated power and reporting rate.

These simulation parameters have been chosen because they have been studied as they impact on the control:

- Voltage Accuracy (Acc_V);
- Power Generation (P_{GEN});
- Reporting rate (fps).

Evaluation Metrics

In order to be able to evaluate the results obtained, it was decided to evaluate the impact of the voltage measurement uncertainty and of the reporting rate, in terms of total reactive used in the grid to bring the voltage value back to the pre-established value.

In particular, the total Reactive Power (Q) can assume a positive or negative value, based on the value of the voltage assumed in the network. This could cause problems in calculating the total reactive power. To avoid this, it was decided to extrapolate the absolute values of Q at each instant of data transmission. Once this

is obtained, the calculation of the total Q is carried out, as indicated in Equation 3.11.

$$\hat{Q} = \sum_{i,j=1}^{N} |Q_{\mathrm{i,j}}| \tag{3.11}$$

Where N is the total number of transmitting data, i is the number of nodes and j is the number of transmitting data.

This calculation is performed for all levels of $\mathrm{Acc_V}$ and fps reported in Table 3.10. In order to be able to better compare the results obtained, the total reactive power value at the reference level, which $\mathrm{Acc_V}$ is equal to 0%, is removed from the total reactive power of each single level of accuracy analyzed, as reported in Equation 3.12:

$$Q_{\mathrm{TOT}} = \hat{Q}_{\mathrm{Acc}} - \hat{Q}_{0\%} \tag{3.12}$$

Where $\hat{Q}_{Acc}$ is the total reactive power with PMUs non-zero voltage accuracy and $\hat{Q}_{0\%}$ is the total reactive power of ideal PMUs with no voltage measurements error.

3.2.3 Results

In this section, thanks to the Distributed Online Voltage Control [53], the impact of some PMUs voltage accuracy on this control are evaluated, when some parameters are varied, such as:

- Voltage Accuracy ($\mathrm{Acc_V}$);
- Reporting rate (fps).

All achieved results is based on a 5 minute power grid simulation.

In this thesis, the results in which $\mathrm{P_{GEN}}$=1.0 are not shown since, since there are no overvoltages, the control does not intervene and therefore there is no impact on the measurement accuracy.

The Figure 3.15 shows the total reactive power used in the grid by the control to bring the voltage value back to the preset value, at different PMUs accuracy levels. In fact, fixed the fps with which the control sends the data, it is possible to notice how, going to increase the accuracy value of the PMU, the total reactive power increases. For example, set 10 fps, $Q_{0.1\%}$ (Reactive Power with PMU voltage accuracy 0.1%) $\approx$ 6.5 VAr, $Q_{0.25\%}$ (Reactive Power with PMU voltage accuracy 0.25%) $\approx$ 11.5 VAr and $Q_{0.3\%}$ (Reactive Power with PMU voltage accuracy 0.3%) $\approx$ 14 VAr. Instead, set 25 or 50 fps, the trend is identical to the previously analyzed

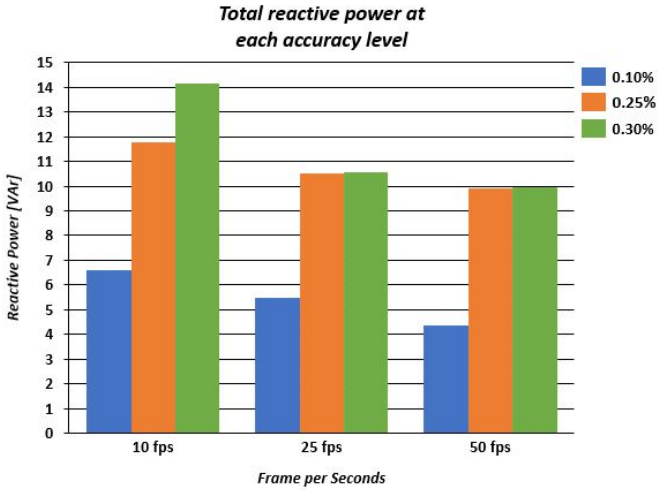


Figure 3.15: Total Reactive Power at each PMUs accuracy level

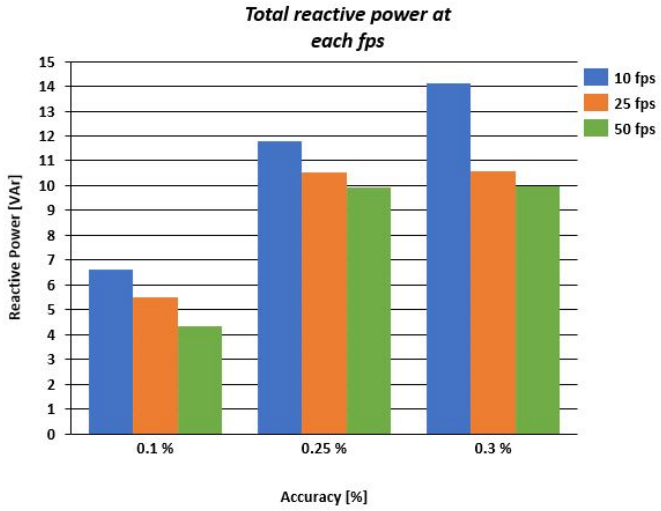


Figure 3.16: Total Reactive Power at each fps

case but less marked for accuracy equal to 0.25% and 0.3%, since by increasing the number of fps and having an uncertainty value so close, the impact of the measurement uncertainty on the control turns out to be the same.

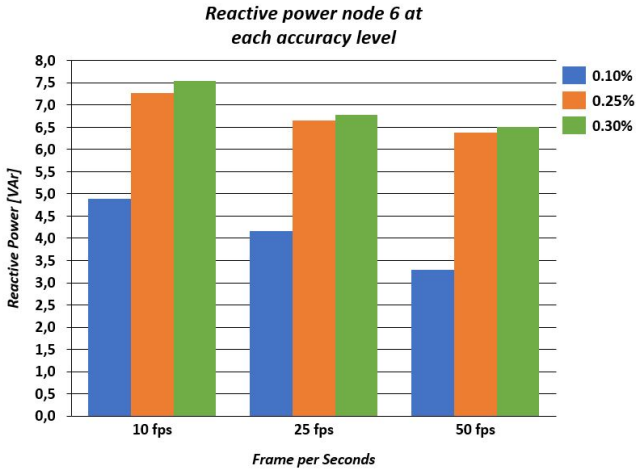


Figure 3.17: Reactive Power (node 6) at each accuracy level

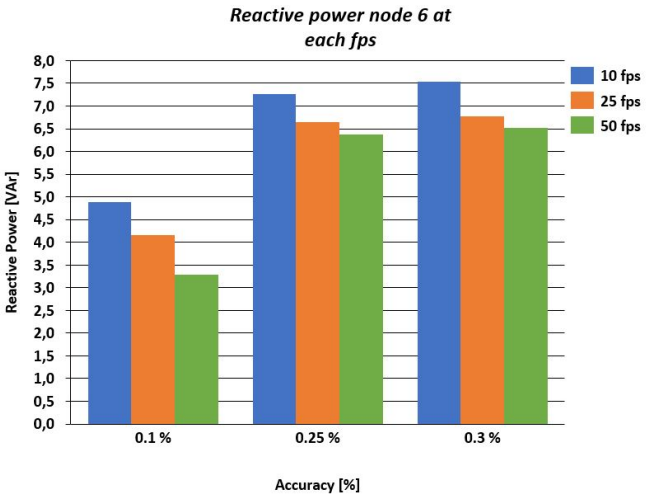


Figure 3.18: Reactive Power (node 6) at each fps

The Figure 3.16 instead shows the effect that the different levels with which the data are transmitted from the PMU to the controller have on the total reactive power used by the controller. It is possible to note that, by setting the uncertainty value and increasing the fps, the total reactive power used by the controller decreases. For example, taking into consideration the case in which the uncertainty

of the PMU is 0.1, at 10 fps the $Q \approx 6.5$ VAr, at 25 fps the $Q \approx 5.5$ VAr, and at 50 fps the $Q \approx 4.2$ VAr. All this translates into a "saving" of reactive power circulating in the grid, both in economic and network loss terms.

In Figure 3.17 shows how node 6, which as shown in the Figure 3.12 is the furthest node from generation, the voltage control must act more massively and therefore requires a quantity of reactive power with respect to node 1 (node in which there is is generation). This means that the behavior, in terms of reactive power at node 6, is the one that influences most of the total reactive power used in the network shown in Figure 3.15. In fact, therefore, the trends analyzed for the different levels of accuracy for the total reactive power are also confirmed on node 6.

In Figure 3.18 the reactive power used by the voltage control in node 6 is analyzed for the different PMUs fps levels. Also in this case, for what has been said above about the node 6 which is the node that most influences the voltage control given the nature of the simulated electrical network, the achieved results and shown in Figure 3.16 are the same.

3.2.4 Conclusions

The sensitivity analysis carried out in this section has allowed us to verify the impact of the PMUs voltage measurement accuracy on the distributed online voltage control. In particular, different measurement accuracies and data rates (fps) were taken into account and varied in values of typical commercially available PMUs.

The achieved show how, for the different levels of accuracy of commercial PMUs analyzed, the choice of the same affects the voltage control algorithm used, the lower the accuracy and the less reactive it will be uselessly used in the network to control the voltage. Similarly, by increasing the quantity of data transmitted to the controller, savings are obtained in terms of the reactive power which circulates in the grid to carry out the voltage control.

Future development will focus on different types of PMUs, micro-PMUs or other voltage sensors installed in the grid which can be exploited for voltage monitoring. Furthermore, other analyzes will be carried out in order to reduce as much as possible the waste of reactive power circulating in the network to control the voltage and optimize it.

Chapter 4

Resilience in Smart Utility Applications

4.1 Preliminary Sensitivity Analysis of Combinatorial Optimization (CO) for NILM Applications: Effect of the Meter Accuracy

Power grid resilience can also impact end-user applications. For example, it is possible to think of reducing the number of smart meters to be used within an environment, whether domestic or industrial, through non-intrusive load monitoring techniques, i.e. the so-called Non Intrusive Load Monitoring (NILM) [58]. This technique aims to detect the energy consumption of individual devices from unique aggregated energy data. In some areas, specifically in industrial ones, monitoring the electrical consumption of each device is necessary to provide information on the energy optimization of the entire system, thus also providing important information on the areas in which to intervene mainly, containing the costs associated with installation of sensors, thanks to the non-intrusive monitoring process, increasing the resilience of the entire industry. The use of a single measuring device placed upstream of the system allows the consumption of individual subsystems to be obtained through mathematical algorithms applied to the overall measurements. The benefits are potentially numerous, including reducing the number of measurement devices, which would otherwise have been necessary to install on the individual subsystems to be monitored, but allowing the possibility of implementing predictive maintenance approaches based on long-term load monitoring analyses, to avoid unexpected breakdowns of production machines and unexpected production stops.

Indeed, it is of fundamental importance to avoid production stops in a sector, but since industrial production is revolutionizing with the creation of new technologies, these changes lead to an increase in the number and variety of failures, which must be foreseen in time to avoid significant economic losses for the company [59]. For this reason, the role of predictive maintenance and fault diagnosis within an industrial plant is becoming increasingly important [60–62].

Nowadays there are several techniques to approach the NILM problem, as algorithms based on: Hidden Markov Model (HMM)[63–66], Combinatorial Optimization (CO) [67], Multi-Objective Optimization (MOO)[68], Graph Signal Processing (GSP)[69, 70] and Deep Learning[71, 72]. NILM algorithms can be divided into 2 classes: supervised and unsupervised algorithms. In supervised techniques, the true state of the load is present and is used for the training phase of the algorithm, information that is not present in unsupervised techniques. Among the supervised techniques, there is a further distinction there are techniques in which it is necessary to carry out a training phase, among which we find FHMM, CO, and Deep Learning, and techniques in which it is not necessary to carry out a test phase but which need apriori information about the nature of the loads, among which we find MOO [68]. Even if many papers related to new NILM techniques or experimental or simulated characterization of these NILM techniques have been proposed in the literature, some issues related to the development of the meter networks are required to perform reliable NILM solutions still require to be investigated. In detail, in many papers proposed in the literature, the accuracy of the electrical energy meters, the number of loads, or the quantities to be measured are fixed at the beginning of the study. On the contrary, the issues that the proposed paper aims at investigating are: i) how the meter accuracy influences the overall performance of the NILM algorithms? ii) if the meter accuracy worsens what happens to the maximum number of loads that can be reliably analyzed? iii) is there any power metrics that are more reliable when the meter accuracy worsens? Thanks to this research, first sensitivity analysis on the performance of one well known NILM technique, i.e. the Combinatorial Optimization algorithm, when the meter accuracy changes according to what is expected when using real meters in real measurement scenarios as described by the EN 50470-1 standard [73].

4.1.1 Notes on the problem of energy disaggregation

The name Energy disaggregation indicates a set of techniques that singularly estimates the energy consumption of many appliances monitored by a single smart meter, instead of N smart meters where N is also the number of appliances. At the residential level, it is a low-cost system because it involves replacing the meter supplied to the individual household, with a new meter of the latest generation

that implements smart functions. A similar argument applies within an industry, where it does not cause particular problems of installation since it is a non-intrusive method, or does not require the implementation of new sensors, indeed it requires a significantly reduced amount, compared to a classic monitoring system. The problem of energy disaggregation can be formulated as follows. Given a sequence of energy consumption data $X = \{x_1, x_2, ..., x_T\}$ from N active appliances at the smart meter input point at $t = \{1, 2, ..., T\}$, the task of the NILM algorithm is to infer the energy contributions y_t^i of the appliances $i \in \{1, 2, .., N\}$ at time t, as at all points at time t, as shown in Equation 4.1:

$$X_t = \sum_{i=1}^{N} y_t^i + \sigma(t) \tag{4.1}$$

where $\sigma(t)$ represents the measured noise or the contributions of the non-justified equipment [74].

4.1.2 Combinatorial optimization

The Combinatorial Optimization (CO) algorithm was introduced by Hart [67] and has served as a foundation in the NILM literature. The main assumption of this algorithm is that each appliance can have multiple states, ranging from 1 to K, where K is a not too large number, and each state is associated with some energy consumption. The goal of the algorithm is to assign the various operating states correctly, such that the difference the aggregate measured power and the sum of the consumption of the various appliances, is minimized, as shown in Equation 4.2.

$$\widehat{x}_t^{(n)} = \underset{x_t^{(n)}}{\operatorname{argmin}} \left| y_t - \sum_{n=1}^{\bar{N}} \widehat{y}_t^{(n)} \right| \tag{4.2}$$

The algorithm performs the following steps, shown in Figure 4.1.

The algorithm is divided in two phases: training phase and test phase. Initially, in the training phase, the algorithm receives the measure of every single appliance power. Subsequently, thanks to k-means clustering algorithm, the load profile is transformed in a sequence of finite state, forming the appliance model. After all appliances is modelled, the CO algorithm, build a lookup table with every combination of operating states. In the test phase, the Combinatorial Optimization receive in input the aggregate power and found the most likely combination of states of appliances based on lookup table.

To perform the Combinatorial Optimization algorithm, the NILMTK toolkit [75, 76], developed in python environment and the most widely used for energy disaggregation problems was used.

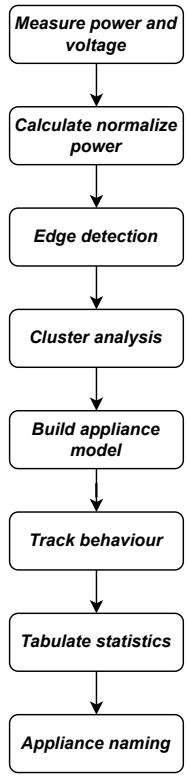


Figure 4.1: CO Flow chart

4.1.3 Simulation setup

Dataset

NILM disaggregation, usually, is performed on real measured data, acquired through an assortment of meters that measure electrical parameters for a long time. The aim is to perform a preliminary analysis about the sensitivity of Combinatorial Optimization on parameters as the number of electrical signature features, the meter accuracy, and the number of loads. To generate the loads' dataset a full experimental approach is not applicable. This is because, from one side, there isn't in literature the availability of an experimental dataset with the properties mentioned above, and, on the other side, the creation of a huge number of real experiments requires a lot of meters with different accuracy and a long observation time. For these reasons, the design an algorithm that simulates the loads' absorption profiling, and give also the aggregate value. This approach allows the creation of a lot

of datasets, with all the required characteristics.

Table 4.1: Loads electrical signature

Loads	$\mathbf{P_{min}}$ **[W]**	$\mathbf{P_{max}}$ **[W]**	$\mathbf{Q_{min}}$ **[VAr]**	$\mathbf{Q_{max}}$ **[VAr]**	**States number [f]**
Load 1	100	500	75	200	4
Load 2	450	500	170	200	4
Load 3	12	20	12	15	3
Load 4	230	260	97	110	4
Load 5	80	130	60	100	4
Load 6	480	480	200	200	2
Load 7	297	300	133	13	3

A Matlab^{TM} script generates the simulated dataset. It takes the active and reactive nominal power of each load and creates a path by selecting a random state. Loads are described as a finite state machine with nominal parameters reported in Table 4.2 (where P_{min} and Q_{min} are the minimum of the *ON* state, P_{max} and Q_{max} are the maximum values also in the *ON* state). The simulated loads are not based on real devices but their values are chosen to stress the classifier.

To evaluate the sensitivity of the disaggregation technique to the meter performance, the generated dataset is organized in five principal sections, each of them has a different value of meters accuracy, as reported in Table 4.1. The simulated meters performances have been chosen according to the EN 50470–1 standard. Different values of accuracy for active and reactive powers are considered.

Table 4.2: Loads electrical signature

Meter Type	$\mathbf{P_{meter}^{Acc}}$ **[%]**	$\mathbf{Q_{meter}^{Acc}}$ **[%]**	**Sigma OFF State**
1	0	0	0
2	1	2	2
3	5	6	6
4	10	10	10
5	15	15	26

The higher values of accuracy are considered by the norm when high or low temperatures and power quality disturbance affects the environment in which the meters operate. Accordingly, with a sampling rate of one measure per minute, an equivalent of three days (4320 samples) sub-datasets are created. Two of the three days (2880 samples) are used to train the NILM algorithm and the remaining day (1440 samples) to test it, as shown in Figure 4.2.

All the sub-datasets include from to Load 1 to Load 3, 5, 7, respectively for

sub-dataset 3, 5, 7. Every sub-dataset has three feature per load: Active power; Reactive power; Apparent power. Apparent power is obtained by the *Boucherot* relation.

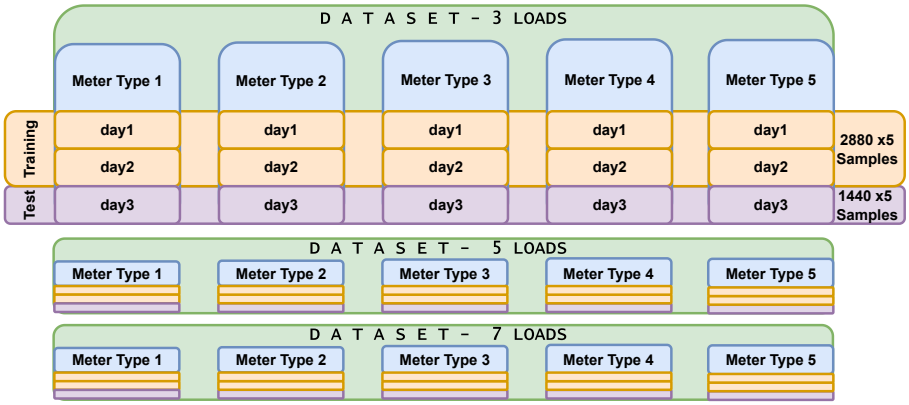


Figure 4.2: Dataset Structure

Evaluation metrics

To evaluate the performance of a NILM algorithm, several metrics can be adopted. They can be classified as event–based or non–event–based. It must be made clear that there is no single metric that is optimal for evaluating all possible cases of load disaggregation, for this reason, different metrics are often compared. Non–event–based metrics analyze how well a load disaggregation algorithm can compute and assign the power consumption of individual devices.

Both these metrics are affected by an important drawback, a mostly powered *OFF* device could increase the algorithm performance, especially for non–event–based metrics. In our case, the simulated dataset is balanced (the number of *ON* and *OFF* status is similar) this characteristic made the dataset proof to the problem described above.

Event–based metrics focus on evaluating the detection of state changes in the operation of appliances, specifically through these metrics, they provide information about the goodness of the algorithm to understand when a device is *ON* or *OFF* [75].

The Combinatorial Optimization algorithm included in NILMTK toolkit, gives the predicted state of each load by only knowing the aggregate power. To evaluate the classification sensitivity two different metrics are selected, both based on the accuracy score.

The *Binary metric* evaluate the CO capability to predict the *ON–OFF* status of an appliance [68]. These metrics are based on four fundamental indices: True Positive (TP), which indicates the correct prediction of the *ON* state, True Negative (TN) which indicates the correct prediction of the *OFF* state, False Positive (FP) which indicates the incorrect prediction of the *ON* state, False Negative (FN) which indicates incorrect prediction of the *OFF* state. Thanks to these characteristic indices, it is possible to derive the Accuracy value, as reported in Equation 4.3, which indicates the ratio of samples that the algorithm has correctly identified, over the total samples.

$$Binary \;\; Accuracy = \frac{TP + TN}{TP + TN + FP + FN} \;\; \in [0, 1] \tag{4.3}$$

The other considered metric is the load state prediction computed when the classifier identified a *ON* status. In this case, the overall accuracy is obtained by the sum of the correct prediction, divided by all predictions, as expressed in Equation 4.4. A correct prediction is considered when the predicted class matches the true class, otherwise, the prediction is un–correct.

$$Multi - class \;\; Accuracy = \frac{Correctly \;\; Predicted}{Total \;\; Prediction} \;\; \in [0, 1] \tag{4.4}$$

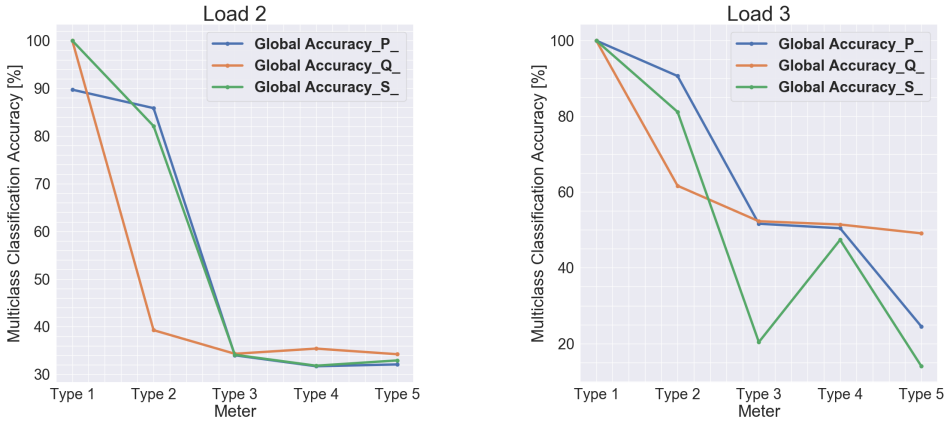
4.1.4 Results

Thanks to the NILMTK tool [75], the performance of the CO algorithm was analyzed when some parameters were varied, such as:

- meter accuracy;
- number of loads;
- type of feature.

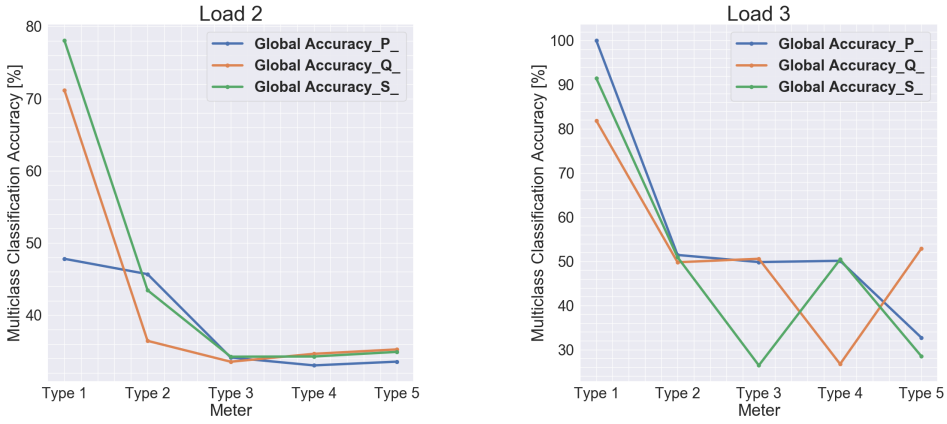
As an example, the results for Load 2 and Load 3 are reported. In particular, the Figure 4.3 represents the trends of multi-class classification accuracy when the total number of loads to disaggregate is 3, Figure 4.4 represents the trends of multi-class classification accuracy when the total number of loads to disaggregate is 5, Figure 4.5 represents the trends of multi-class classification accuracy when the total number of loads to disaggregate is 7, calculated by Equation 4.4, versus the Type of meter (according to the classification given in Table 4.1).

In particular, by analyzing the Figure 4.3(a), 4.4(a), 4.5(a), it's possible to verify how the multi-class classification accuracy depends on the number of loads, both for the Load 2 and for Load 3, Figure 4.3(b), 4.4(b), 4.5(b).



(a) (b)

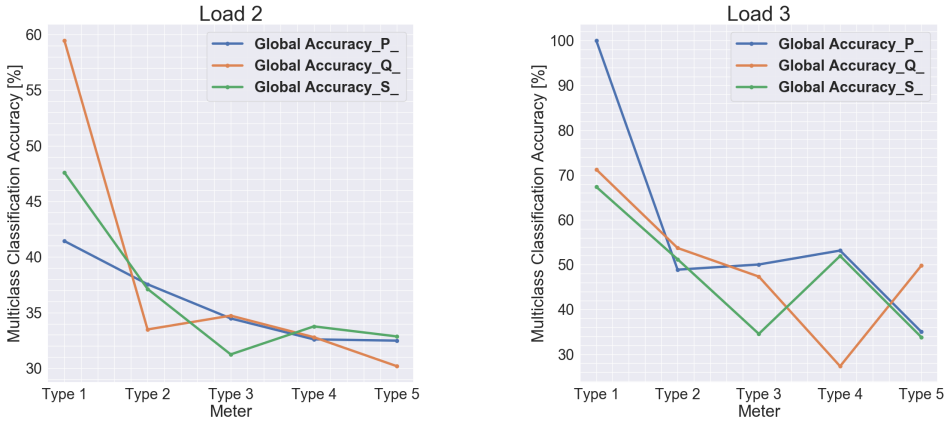
Figure 4.3: Multi–class Classification Accuracy in case of 3 loads to disaggregate



(a) (b)

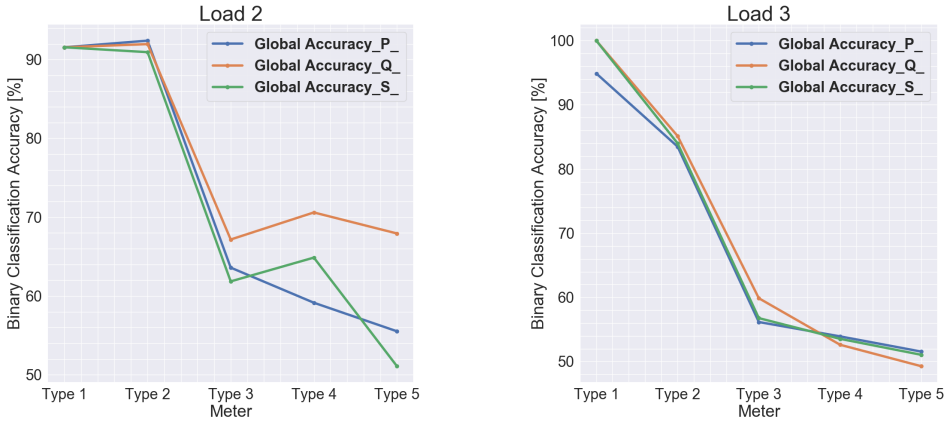
Figure 4.4: Multi–class Classification Accuracy in case of 5 loads to disaggregate

Similarly, Figure 4.6 represents the trends of multi-class classification accuracy when the total number of loads to disaggregate is 3, Figure 4.7 represents the trends of multi-class classification accuracy when the total number of loads to disaggregate is 5, Figure 4.8 represents the trends of multi-class classification accuracy when the total number of loads to disaggregate is 7, calculated by using Equation 4.3, versus



(a) (b)

Figure 4.5: Multi–class Classification Accuracy in case of 7 loads to disagregate



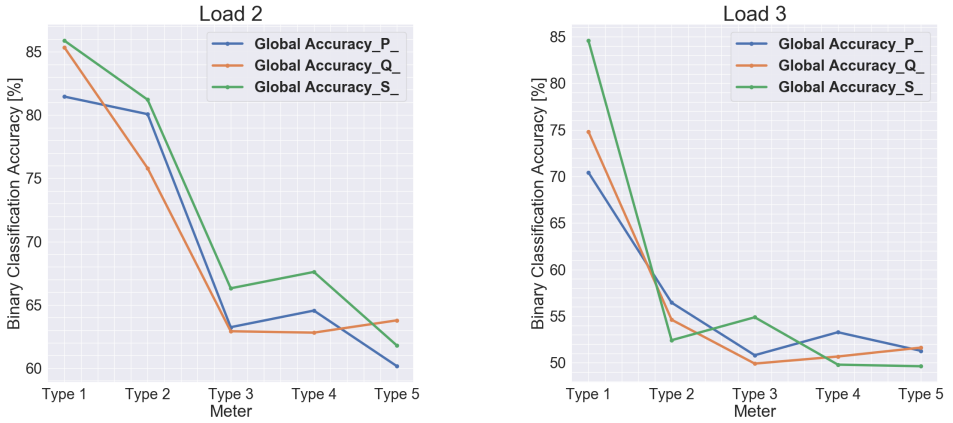
(a) (b)

Figure 4.6: Binary Classification Accuracy in case of 3 loads to disaggregate

the Type of meter. Also in this figure are valid the same considerations made for the multi-class classification

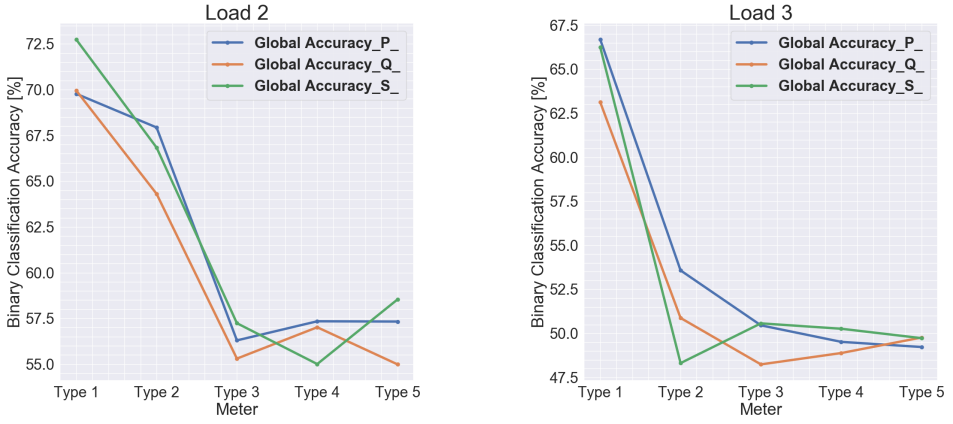
In particular, the following considerations can be made:

- by analyzing, for example for 3 loads to disaggregate, Figure 4.3 and Figure 4.6 it is clear that the classification accuracy, both multi-class and binary,



(a) (b)

Figure 4.7: Binary Classification Accuracy in case of 5 loads to disaggregate



(a) (b)

Figure 4.8: Binary Classification Accuracy in case of 7 loads to disaggregate

deteriorate when the meter metrological performance decreases;

- classification accuracy is sensitive to the increase of the number of loads. In the multi-class case Figure 4.3, for the ideal meter and the apparent power, the performance drops from 100% in 3 load cases, to 79% in 5 loads case in Figure 4.4, and end to 47% with 7 loads in Figure 4.5. With not ideal meter

(i.e. meter Type 2), also for apparent power, only with 3 loads disaggregation problems the performance is still acceptable;

- the same trend could be found in the binary classification as shown in Figure4.6, where disaggregation performance degraded with the increase of disaggregate loads;
- it is not possible to identify a feature that uniquely succeeds in optimizing the classification process, both multi-class and binary, for example, fixed the use of meter type 1, analyzing the Figure4.3 (a) it follows that the best global accuracy is obtained by using the Reactive Power or Apparent Power, but in the Figure 4.5 (a) the best global accuracy is obtained by using only the Reactive Power;
- the same applies to the binary global accuracy, for example, fixed the meter Type 3, from Figure 4.6 (a), 4.7 (a), it is clear that there is no feature that uniquely always returns the highest level of accuracy as the number of loads increases;
- starting from a Type 3 Meter up to Type 5, the performance significantly decrease in both cases and it weakly depends on the meter accuracy;
- in general, with CO classifier, a meter with high metrological performance is required, whatever be the considered feature.

4.1.5 Conclusions

The sensitivity analysis carried out in this paper has allowed us to verify the impact of the meters measurement uncertainty, the number of loads, and the kind of features involved in the performance Combinatorial Optimization, a well–known NILM technique. In particular, several measurement accuracies, power metrics, and the number of loads have been taken into account and ranged in values of typical real applications.

The achieved results prove how the considered quantities of influence generally affect the performance of CO. In particular, the measurement uncertainty due to the non-ideal-meters makes worse the performance of both CO and a binary classifier although such behavior is more significant in the case of a higher number of loads to be disaggregated.

Future developments will focus on the use of more advanced classifiers, capable of better classification performance. In addition, it will be important to evaluate the implementation of the new electrical signature features [77], which will be able to return better disaggregation results, as well as using apparent power S as an

independent rather than dependent variable. Furthermore, through testing on a larger dataset, further analyses could be carried out to refine the NILM algorithm. Unfortunately, it is not easy to find sufficiently consistent datasets in the literature to be able to test the algorithm in the best possible way.

4.2 eLAMI - An Innovative Simulated Dataset of Electrical Loads for Advanced Smart Energy Applications

Nowadays, the smart energy applications are attracting more and more interest, especially due to energy and ecological transitions, whose goals are the reduction of CO_2 emissions and the increase of energy efficiency. As an example, in Europe, the development and use of intelligent measurement systems and techniques has been boosted by European directives in recent years. In 2006, the Directive 2006/32/EC [78] identified the use of intelligent metering systems as one of the tools to improve energy efficiency through suitable algorithms and techniques. In 2009, the Electricity Directive 2009/72/EC [79] declared the obligation for the Member States to ensure the adoption of smart metering systems. Finally, in 2012 the European Energy Efficiency Directive 2012/27/EU [80] reaffirmed the importance of using smart meters, with strict requirements for the Member States regarding both metering and billing.

In this new paradigm, in which energy efficiency and the development of new services based on the measurement of energy parameters are demanding data, the smart meter assumes a key role. On one hand, it accomplishes the primary task of monitoring energy consumption and on the other hand, it could provide new quantities useful for modern smart energy applications. More in-depth, the above-mentioned techniques are generally based on machine learning algorithms or on optimization techniques exploiting electrical parameters related to the electrical signature of a load and/or Power Quality parameters, as for example NILM technique. Whichever approach is followed, all machine learning techniques require the implementation of two fundamental steps to reliably train and tune the algorithms to the case study under consideration: *a)* the accurate measurement of energy consumption and parameters related to power signatures and other parameters that depend on the devices involved, *b)* the monitoring for a sufficiently large time interval to acquire an adequate amount of data. The first phase is crucial as it closely influences the quality and quantity of the information collected. It is very important to have energy measurements characterised by low uncertainties and, at the same time, provide various energy parameters, such as harmonic and

inter-harmonic power, current and voltage values, total harmonic distortion, power factor, etc., that can characterise the way in which a device, or a group of devices, is consuming electrical energy. Since the above-mentioned requirements impose to perform very expensive and time-consuming measurement campaigns, in the last years some datasets have been proposed in the literature with the aim of facilitating the development of new algorithms addressing the cited emerging needs. Many are the papers that propose the use of a dataset to train or tune smart energy algorithms.

In literature two different types of datasets can be found: real and simulated datasets. In particular, real datasets are composed of data, collected on the field, while simulated ones are obtained through suitable software simulators. However, these datasets do not meet all the requirements for effective data usage, i.e. the limited amount of saved electrical parameters, data variability, seasonality, closeness to real scenarios, and definition of the current operating states are just some of the missing or not complete information that makes them poorly suitable for modern Smart Energy Applications.

To overcome these limitations, an innovative energy dataset was developed. The main advantages of the proposal are: *(i)* the variability of the data, in terms of operational states of electrical loads and the adoption of appropriate consumption models; *(ii)* the enormously larger total number of electrical parameters available (433 in our case) compared to the above datasets, such as the complete analysis of frequency behaviour and calculation of harmonics; *(iii)* the seasonality of the data. Furthermore, the presented dataset is a hybrid solution between simulated datasets and those based on real data. Indeed, it is generated through a simulation, starting from real measurements, and customised by means of an effective calculated variability model.

4.2.1 Available electrical energy dataset

The growing demand of new monitoring devices with smart algorithm and technique has led to the development of several dataset capable to tune the performance. In Table 4.3, some examples of public datasets with data collected from the field are shown; they differ for the number of devices, number and type of provided electrical parameters and length. In the following they are briefly described.

- **AMPds** [81] The Almanac of Minutely Power dataset is a public dataset, published in 2013, containing 1 year of collected data of residential appliances from a single household in Canada. This first version contains measurements of electricity, water and natural gas at one-minute intervals, for a total of 525600 readings per year per meter.

Table 4.3: Main characteristics of some public dataset based on real data

Name	Number Appliances	Parameters	Period
AMPds[81]	20	P,Q,S,V,I	1 year
AMPds2[82]	20	P,Q,S,V,I	2 years
BLUED[83]	50	P,Q,V,I	1 week
Dataport[84]	8598	P,S	4 years
DRED[85]	12	P	6 months
ECO[86]	45	P,V,I	8 months
ENERTALK[87]	75	P,Q	1714 days
iAWE[88]	63	P,Q,S,V,I	73 days
REDD[89]	92	P,V,I	119 days
REFIT[90]	20	P	2 years
UK-DALE[91]	109	P,Q,S,V,I	2247 days

- **AMPds2** [82] This second version of the AMPds dataset differs from the previous one only in the number of total readings, 1051200, corresponding to 2 years of acquisition.
- **BLUED** [83] The Building-level fully labeled dataset for electricity disaggregation was released in 2012 by 1 week electricity data from 1 building in the USA. This dataset contains not only the steady-state, but also the state transition of each appliance.
- **Dataport** [84] The Dataport database was created by Pecan Street Inc and published in 2015. It contains electricity data from 722 houses and commercial buildings across different cities in the USA. As it has a sampling period of 1 min for aggregate and appliance signal, this is considered a low frequency dataset.
- **DRED** [85] The Dutch Residential Energy Dataset was released in 2015 and contains energy consumption data from a household in Netherlands, with a total duration over six months. It includes electricity measurements for the aggregate and submetered signal of each device.
- **ECO** [86] Electricity Consumption and Occupancy dataset was collected in 6 Swiss households over a period of 8 months. It contains data recordings of active power, voltage and current at low frequency sampling rate.
- **ENERTALK** [87] The ENERTALK dataset was created in Korea from 22 houses with a total period of 1714 days and it was published in 2019. It

provides active and reactive power measurements (both aggregate and each device), with a sampling frequency of 15 Hz.

- **iAWE** [88] Indian Dataset for Ambient Water and Energy was released in 2013, from recordings electricity, water and ambient data in a house in New Delhi, for a total duration of 73 days. The electrical data were recorded with a sampling period from 1 to 6 seconds over 63 electrical appliances.

- **REDD** [89] Reference Energy Disaggregation Dataset has been published in 2011. It contains 119 days of collected data from 6 households in the USA and includes both high and low frequency recordings.

- **REFIT** [90] The REFIT Electrical Load Measurements dataset includes cleaned electrical consumption data from 20 households in the UK from 2 years of recordings in 2016. It contains electrical data with a sampling period of 8 s and active power as only parameter.

- **UK-DALE** [91] UK-Domestic Appliance Level Electricity was published in 2015 and it contains 2247 days of data by 5 residential buildings in the UK. Just like REDD, it reports high and low-frequency data and all appliances are sub-metered.

Collecting data to build a dataset is a fairly complex process. As long measurement campaigns have to be carried out, the process requires a considerable amount of time, effort, and instrumentation to measure and record data. One of the main limitations of the real datasets in the literature today is the small number of reported electrical parameters (at most P, Q, S, V, I).

This could represent a limitation for algorithms in the field of Smart Energy. In particular, considering methods for load profiling, NILM and fault or predictive diagnosis, the optimal choice of needed parameters is still a research topic: therefore the availability of a large number of electrical quantities, able to define the complete "electrical signature of the load", could help in performing an accurate selection.

Furthermore, real datasets are often characterized by missing data due to several problems that may occur during the measurement campaigns, time mismatching between individual load data and aggregate data or possible errors due to malfunctioning and inaccuracy of the adopted instrumentation.

The absence of information about current operating states of each device can also be a limitation for these datasets, e.g. in the case of supervised artificial intelligence algorithm training or in the definition of consumption quality as well as system efficiency indices. A solution to the aforementioned problems could be the simulation of data.

A simulated dataset does not require lengthy monitoring campaigns, saving time, costs, and instrumentation. All these advantages are provided as long as the simulation process is correctly implemented, which is not trivial in terms of suitable modeling and computational costs.

In literature, some simulated datasets are presented as reported in Table 4.4 and discussed below.

Table 4.4: Main characteristics of some public dataset based on simulated data

Name	Number Appliances	Parameters	Period
AMBAL[92]	14	-	1 days
SHED[93]	66	P, S, V, I	14 days
SmartSim[94]	25	P	7 days
SynD[95]	21	P, S, V, I	180 days

- **AMBAL** [92] Automated model builder for appliance load dataset was published in 2017 and it comprises 14 domestic loads at a sampling rate of 1 Hz for a time duration of one day. The AMBAL dataset allows the user to build models using real energy consumption data, based on parameterised signature sequences. The main operational phase of the AMBAL dataset includes preprocessing, extraction of active segments, segmentation, and model fitting.
- **SHED** [93] Simulated high-frequency energy disaggregation dataset, released in 2018. It is a commercial dataset containing the power consumption of 66 buildings at a sampling frequency of 1/30 Hz. The data is generated synthetically and based on modeling the current flowing through an electrical device and is matched with the real model of electrical devices.
- **SynD** [95] SynD is a synthetic dataset that was published in 2020 and simulates readings of electricity consumption for a house for 180 days. The measurements campaign was based on the monitoring of 21 different residential devices from 2 households in Austria. In particular, the consumption patterns were observed, the absorption profiles of each device were then extracted and finally the dataset was generated.
- **SmartSim** [94] A Device Accurate Smart Home Simulator for Energy Analytics was released in 2016 and is a simulated dataset of 1 week total duration. It uses the energy modelling of individual devices to build the final dataset with the aim of generating accurate domestic energy traces that are qualitatively and quantitatively similar to real energy data traces.

Despite the large amount of simulated datasets in the literature, most of them still suffer some of the aforementioned problems, as limited number of saved electrical parameters, absence of harmonic and power quality information of seasonality, monthly, daily variability, as well as variability of operating states; furthermore, they often provide a low likelihood value with respect to real scenario profiles.

4.2.2 Design of dataset generation

In this section, the design process of the electrical Loads Acquisition for Monitoring Instruments (eLAMI) dataset and its implementation is described. At first, main requirements that a modern energy dataset must have are discussed. Issues related to the the choice of a simulator and possible solution are then faced. Chosen electrical loads, along with consumption patterns and the simulator description close the section.

Requirements

A modern energy dataset for monitoring and investigating consumers' energy behaviors must have specific characteristics. The main requirements are:

1) High number of saved electrical parameters, both in time and frequency domain;

2) High likelihood to real scenario profiles;

3) Faithful representation of the devices;

4) Considering the metrological performance of commonly used energy smart meters;

5) Presence of Power Quality and harmonic data;

6) Appropriate observation times congruent with the objectives;

7) Current operating state of the monitored device.

As regards *1)* having a large number of electrical parameters allows for a better representation of the electrical signature of the load. In this way, for example, as also proved in Section IV, energy efficiency algorithms can drastically increase their performance. Therefore, in the eLAMI dataset, 433 electrical parameters are calculated at each measurement interval. Furthermore, in our simulated dataset we try to represent an electrical scenario as faithful as possible to reality. Specifically, reported consumptions are related to a 2–person–household.

Having a good match between the simulated scenario and the real one, simply summarized as likelihood, is crucial as it offers the possibility, for instance, of training AI algorithms on consistent data, as mentioned in *2)*. This avoids possible mismatches between performance obtained in simulation and real scenarios.

As said in *3)* it is necessary to take into account both how the electrical energy is consumed, but also how the individual load behaves in terms of electrical operation in reality. In particular, in our case we have chosen to represent equipment as 'state machines', simulating the corresponding nominal operating states. We consider this choice to be valid, having chosen to simulate the assumed scenario under permanent regime. Of course, in reality, between different 'operating states' there are transients that can lead to more or less marked variations in electrical quantities. As regards *4)*, furthermore, these variations can also be related to the natural duty cycle of the equipment or be due to the uncertainty of the monitoring system used [96]. eLAMI reports this variability thanks to the mathematical model for generating absorption profiles implemented.

As said in *5)* today, given the widespread use of electronic equipment, we consider the study of the harmonic behavior of electrical loads to be of great interest. For example, the analysis of the frequency spectra of voltage and current absorption of devices can provide useful information on the health of loads and in general of the entire system, also in terms of the quality of the power supply system (Power Quality). eLAMI in this case reports a considerable amount of harmonic and quality parameters.

With regard to the observation time of the monitored system *6)*, it must be chosen in such a way as to meet the objectives of the applications for which it was hypothesized. Classification, clustering, NILM, Load Profiling, and energy retrofit algorithms in most cases aim at analyzing the system over sufficiently long time horizons. In our case, eLAMI refers to a time horizon of one year. As regards, *7)*, an operating state of the monitored device can be defined as a steady-state voltage and current joint profile, whose availability allows the dataset user to evaluate the proper load working cycle and extract electrical signature quality indices and detecting possible incoming anomalies.

Indeed, referring to "electrical signature", it not only deals with the typical quantities (P, Q, I_{RMS}, etc.) but with the entire frequency spectrum of voltage and current profiles absorbed by the electrical load. Such information are therefore also state-related, i.e. they can change for each operating state of the load.

Therefore, the proposed simulator must be designed to generate voltage and current profiles under all possible load states tested and for a predefined simulated time, in order to get the spectrum information.

An issue raised at this stage is related to the way the frequency spectrum could

be faithfully simulated. The approach here followed is to make measurements on real loads under different tested operating states and adopt acquired information as a basis to generate simulated profiles.

Based on the knowledge of these quantities and the known usage habits of the electrical loads, it is possible to create the dataset by using the acquired information.

Any accidental failures or malfunctions that might occur in the real electrical system are neglected in the current status of the simulator. This is reasonable as these are very rare events in reality that, when compared with the simulation time frame, can be neglected. The simulator modular structure would eventually permit to add such situations in a fairly easy fashion.

Electrical load description

According to the aforementioned requirements of a new simulated energy consumption dataset for the residential appliances with innovative saved electrical parameters, namely eLAMI, has been developed. The choice of simulating a residential building consumption profile has the aim to provide a means with innovative characteristics compared to the datasets currently present in the literature for the evaluation of new techniques and algorithms in the field of Smart Energy, including NILM, Load profiling, Management Systems, and Energy Efficiency algorithms.

eLAMI refers to 360 days of simulation of a house having 36 connected appliances, as described in Table 4.5. But in the future other years will be added. The "ID" is the appliance identifier, N_S is the overall discrete number of tested operating states (including the OFF state) and the P_{Nom} is the upper bound each appliance can absorb, according to the manufacturer's indications. At each measurement interval, 433 electrical parameters are computed, whose details are reported in Subsection 4.2.2. In addition to the information on the individual load, the same parameters are also calculated for the total aggregate and three partial sub-aggregates consisting of subsets of loads. In addition to the calculated quantities, current operating state is also provided.

The partial aggregates are provided for the three different identified zones of the virtual house. For each zone, a subset of loads was defined. The combination of loads for each sub-group was chosen to obtain aggregates with a progressive number of loads, as shown in Figure 4.9. This is an important feature for the structure of eLAMI as it offers researchers the possibility to test the algorithms on an increasing number of loads, therefore on an increasing complexity level.

Although all loads are connected in parallel, their supply is carried out by means of radial lines. Therefore, in eLAMI, the voltage at the terminals of each load is not the same but depends on the load conditions.

Table 4.5: Electrical loads specifications. Returns the appliance identifier (ID), the name of the loads (Appliance), the number of states tested (N_S) and and the maximum active power that each load can absorb (P_{Nom})

ID	Appliance	N_S	P_{Nom} [W]
1	Beard Trimmer	2	4
2	Blender	2	60
3	Boiler	2	220
4	Coffee Machine	2	1200
5	Dehumidifier	2	190
6	Desk Lamp	4	10
7	Electrical Oven	3	2400
8	Electric Toothbrush	2	5
9	Fan	4	40
10	Fan Heater	4	1900
11	Fridge	2	140
12	Hair Clipper	2	6
13	Hair Dryer	3	420
14	Hair Straightener	2	65
15	Headphones Charger	2	5
16	Hoover	3	600
17	Infrared Heater	2	1350
18	Iron	2	1300
19	Kettle	2	2000
20	Lamps Bathroom	2	30
21	Lamps Bedroom	2	90
22	Lamps Closet	2	75
23	Lamps Corridor	2	55
24	Lamps Entrance	2	65
25	Lamps Kitchen	2	125
26	Lamps Livingroom	2	145
27	Microwave	2	1300
28	Notebook	2	60
29	PC-Desktop	2	300
30	Printer	2	750
31	Router	1	5
32	Smart TV	2	105
33	Smartphone Charger	2	25
34	Toaster	2	640
35	TV	2	85
36	Washing Machine	4	800

Moreover, the reported OFF state, for some devices, is an indication of a standby state. Therefore, the absorbed current is slightly different than zero.

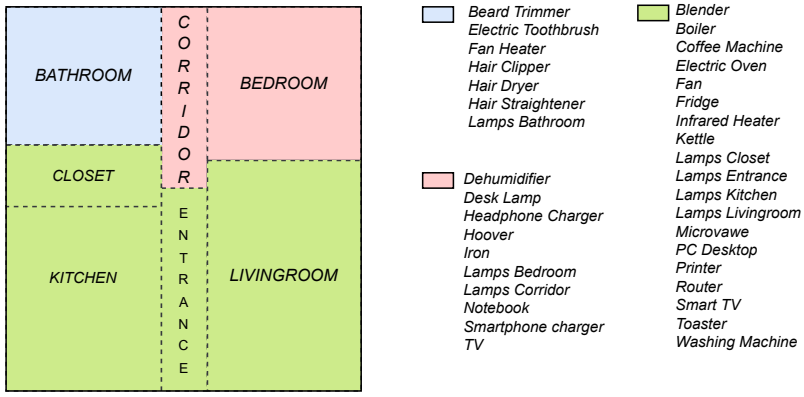


Figure 4.9: House scheme and electrical loads distribution. The blue zone represents the *"Partial 1"* with 7 electric loads; the pink zone represents the *"Partial 2"* with 10 electric loads; the green zone represents the *"Partial 3"* with 19 electric loads

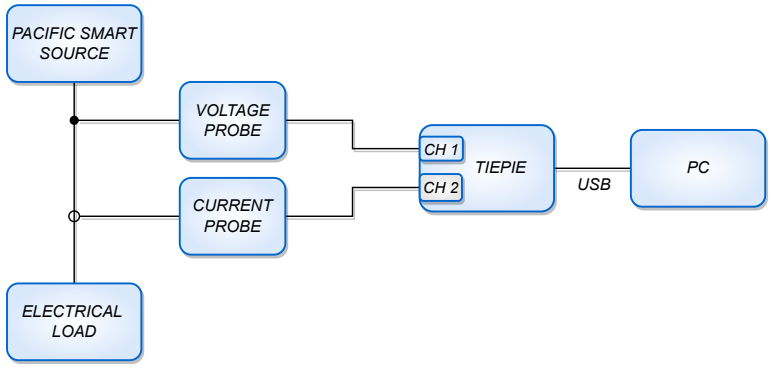


Figure 4.10: Block diagram of data acquisition setup

Simulation basis: data acquisition

In order to define the frequency spectrum of a load, as mentioned above, it is necessary to experimentally acquire its absorption profile. Through a measurement campaign in Industrial Measurement Laboratory (LAMI) in the University of Cassino and Southern Lazio, 36 residential typical electric loads (Table 4.5) have been acquired. Current and voltage waveforms for each devices has been recorded and get the corresponding reference profiles for use in data generation software. The block diagram of the experimental setup for data acquisition is shown in Fig-

ure 4.10.

The adopted power supply system is a Pacific Smart Source, an electrical network emulator which allows reproducing any mains profile both in terms of amplitude and harmonic content [42]. In particular, it has been used as arbitrary voltage generator to supply the electric loads.

In order to emulate real working conditions, the power grid voltage was first acquired and the corresponding harmonic characteristics were calculated up to the 50th harmonic order. The harmonic coefficients obtained, in terms of amplitude and phase, are used as an input for the Pacific Power Source.

The emulated mains voltage profiles both with and without load, are shown in Figure 4.11, 4.12 along with the harmonic contents. For clarity we report the distribution of the percentages harmonic coefficients from the 2th to the 13th order. The harmonic coefficients shown in Figure 4.12 were obtained by extrapolating the characteristics of the harmonics of the voltage signals and evaluating the amplitudes in percentage terms with respect to the corresponding fundamental tones.

Furthermore, it can be seen from the figures that there are differences between the voltages in different load conditions. In particular, the voltage under load is lower and has a slightly different distribution of harmonic coefficients. As expected, the voltage profiles of Figure 4.11 do not reproduce a perfect sinewave, since it contains the harmonics contributions.

Table 4.6: Comparison of some characteristics of the voltages: Acquired Main Voltage, Emulated Voltage With Load and Emulated Voltage Without Load

	V_{RMS} [V]	V_{RMS} Fund [V]	V_{DC} [V]	V_{PK} [V]	THD_V [%]
Acquired Main V	231.35	230.82	12.79	326.27	3.94
Emulated V With Load	232.27	231.99	10.06	327.31	4.85
Emulated V Without Load	226.89	226.39	10.07	317.86	4.72

Through the use of a Tektronix P202A Hall effect probe [97], powered by a Tektronix 1103 power supply [98], with a transformation ratio of 100 mV/A, the electrical current flowing in the circuit was measured.

Using a Tektronix P5200 differential probe [99], with a transformation ratio of 1:500, the voltage supplied by the Pacific to the electrical loads was measured.

A TiePie HS5 [44] was used to acquire the measurements through a customized software developed in Matlab^{TM} environment.

30 repeated measurements (N_{ACQ}) were performed for each operating state tested. The iterated procedure allowed obtaining the corresponding average absorption profiles and the associated standard deviations for voltage and current waveforms.

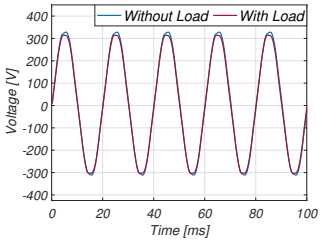


Figure 4.11: Emulated Voltage profiles with load and without load

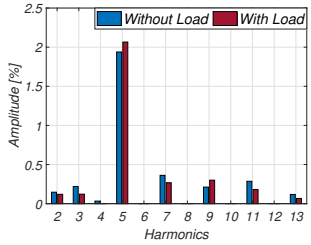


Figure 4.12: Percentage harmonic coefficients normalized with respect to the fundamental frequency

The sampling frequency (F_s) used for profile acquisition is 5 kHz. For each acquisition (of each load state) 25000 points (N_P) were acquired.

The amplitude resolution of the acquisition system, through the TiePie Hs5, was set to 14 bits per channel, with a full scale of 0.8 for the voltage channel and 2 V for the current channel. Considering the conversion factors of the probes used, therefore (1:500 and 100 mV/A) this gives 400 V for the voltage channel and 20 A for the current channel. Values are chosen in relation to the electrical systems considered. All the sampling characteristics are summarized in Table 4.7.

Simulator description

The purpose of this section is to provide a general description of some of the fundamental parts that make up the innovative simulator created for the realisation of eLAMI, highlighting the procedures followed in the simulation. All processing operations were performed in Matlab^{TM} environment.

The simulator consists of three sections: (1) Input, (2) Processing and (3) Output.

For each section, the chronological flow and the main operations are described.

1) The *Input* section consists of 4 macro blocks:

Table 4.7: Sampling characteristics used for the acquisition of electrical load profiles

Specifications	Descriptions
F_s	5 kHz
N_P	25000
T_{OSS}	5 s
N_{ACQ}	30
A/D converter resolution	14 bit
Full scale of the voltage channel	0.8 V
Full scale of the Current channel	2 V
Voltage probe conversion factor	1:500
Current probe conversion factor	100 mV/A

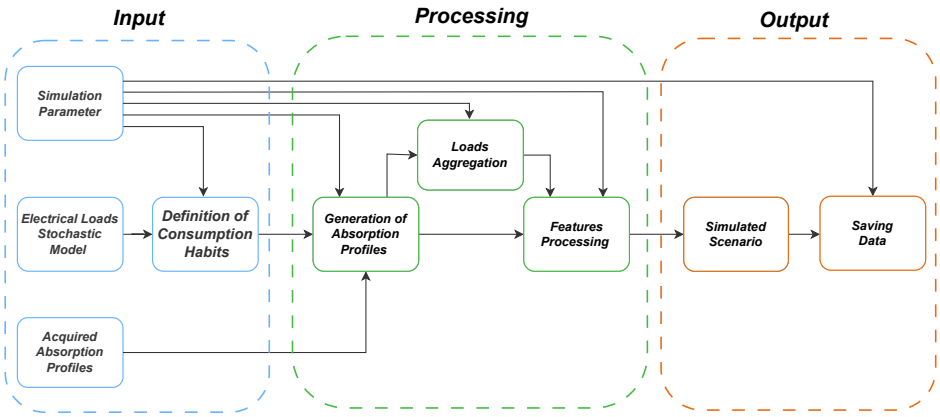


Figure 4.13: Block diagram of the simulator composed of three sections: Input, Processing and Output

1.1) In *Simulation Parameter* block, specifications for the simulation are defined, e.g. simulation interval (1 year), measurement time (5 s), and aggregation criteria, just to cite a few. The content in round brackets is the assignment of possible parameter values. They are sent to the following blocks, defining the characteristics of the electrical scenario to be simulated.

1.2) In *Electrical Loads Stochastic Model*, mathematical relations about operating state changes are defined according to output got by previous surveys performed by the authors in residential buildings.

1.3) In *Definition of Consumption Habits*, taking into account the many fac-

tors influencing the electric consumption and adopting the mathematical models defined in the previous block, along with the hypothesized simulation interval, typical consumption habits, or patterns, are defined and used as input to generate faithful absorption profiles. The behavioural consumption patterns, defined for each load, take into account daily variability and seasonality. This is made possible by the implementation of a stochastic process, studied ad-hoc for the assumed dynamic system. To explain the suitability of the implemented stochastic model to avoid a mismatch with real scenarios, in our simulation framework it is absolutely unlikely that the blender or hoover will switch on during the night as well as lighting or heating during winter periods for consecutive days is more likely than in summer times. In eLAMI, the defined stochastic model also considers all these factors. In this way, for each load, the days turn out to be dependent.

1.4) In *Acquired Absorption Profiles* contain the reference absorption profiles obtained as described in Section 4.2.2.

2) The *Processing* section is composed of:

2.1) *Generation of Absorption Profiles* is a block that, taking inputs as described before, generates the voltage and current waveforms related to the conditions to be simulated. Such signals are simultaneously sent to both "Loads Aggregation" and "Features Processing" to perform different operations, as described below. Such waveforms are referred to the i-th iteration for a specific instant of a simulated day and condition of each considered appliance. The compounded values define the "Current Operating State" of each load.

2.2) The *Loads Aggregation* block receives the output of *Generation of Absorption Profiles* and *Simulation Parameter* and aggregates individual loads in a macro-load condition, i.e. considers all appliances belonging to a specific category (e.g. bathroom) as they were one only aggregated load.

2.3) In *Features Processing*, all electrical quantities assumed for individual loads and aggregates are calculated. For electrical parameters calculations, our simulator implements the definitions of Power in IEEE-1459, especially referring to single-phase non-sinusoidal case. The calculated electrical parameters refer to: $V_{RMS}{}^{TOT}$ and $I_{RMS}{}^{TOT}$, V_{RMS} and I_{RMS} at the fundamental, of harmonics and DC components alone; active, apparent, non-active and distorted power; power factor and harmonics

distorted parameters, for a total of 26 electrical parameters. Furthermore, for better identification of electrical loads signature, the simulator also implements the definitions of measurements in IEC 61000-4-7 Standard [100], regarding harmonics and interharmonics, including the rms values of voltage and current groups up to the 50th harmonic order are calculated, including harmonic sub-groups ($SubG_rV$, $G_rV_1...G_rV_{50}$; $SubG_rI$, $G_rI_1...G_rI_{50}$) and the corresponding phase values of each group calculated for a total of 202 parameters. In addition, the harmonic index of the maximum amplitude tones of voltage/current in each group is also provided, the phase of each harmonic group and the current operating state, to achieve further 205 parameters. Considering the overall processing, the total number of electrical parameters reported in eLAMI is 433.

3) The *Output* section is composed of:

   3.1) In *Simulated scenario*, the computed electrical parameters are packed considering the "simulation interval" (e.g. 1 day, 1 month, 1 year) parameter and their size also depends on the measurement time (e.g. 5 s), which is the time resolution over which the 433 parameters are computed. Future simulated years of eLAMI will be added to the main folder.

   3.2) In *Saving Data* block, a hierarchical structure is created for saving the dataset, as illustrated in Figure 4.14. The latter was created to make the data as much usable as possible for the end user. From a hierarchical point of view, eLAMI is divided into a first level "by months", then "by loads" and finally "by calculated electrical parameters". All information are stored in granular ".csv" files, one for each basic condition (day of the month).

4.2.3 Results

The aim of our work is to provide a dataset with innovative features compared to datasets currently found in the scientific literature, for the evaluation and development of new techniques and algorithms in the field of Smart Energy Applications. Of course, it is of paramount importance that the dataset is physically consistent with real case scenarios.

To this end, first of all there is a validation of dataset simulator; then, some dataset peculiarities are highlighted, and finally some examples of eLAMI applica-

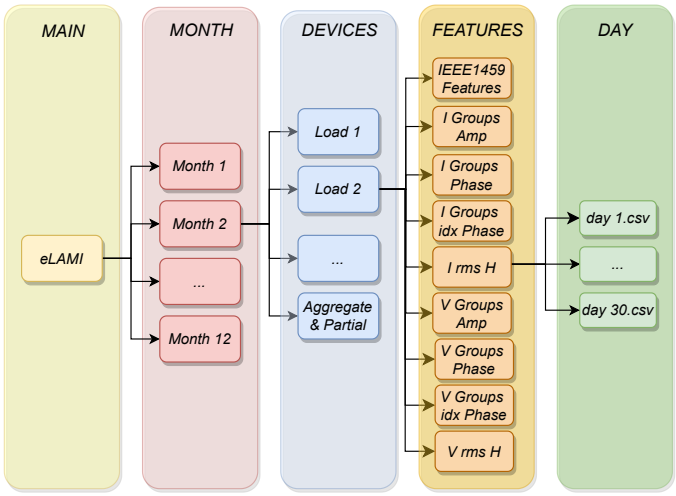


Figure 4.14: Saving eLAMI structure

tions in the field of Smart Energy, in particular Load Profiling, NILM, and Energy Management systems, are proposed, as reported in [101].

Validation of dataset generation

For the technical validation of the simulator and the corresponding consistency of the generated data, a comparison between the measurements obtained from a real test and a simulated one has been carried out, by assessing their metrological compatibility. In particular, the electrical scenario assumed for the test, is composed of 3 real loads of eLAMI with different electrical characteristics, namely *Fan*, *Fan Heater* and *Smart TV*. They have been connected to the Pacific network emulator [42], then fed in parallel with the same voltage signal used for the creation of eLAMI reference profiles 4.2.2. At the same time, the absorption profiles, at the ends of every single load and the *Aggregate*, were monitored using a laboratory wattmeter, the Precision Power Analyzer WT3000 [102]. The same scenario, without WT3000 measurement instrument, has been replayed in the simulation environment, by starting from the reference profiles previously acquired. Test set-up settings are total test duration (1 hour), measurement time (5 s), and the total number of measurement points (720).

At the end of the test, a comparison was made between the results obtained in the two cases, with the aim of showing: *i)* a comparison between variability ranges in the case of real and simulated data; *ii)* the metrological compatibility of

the simulated measurements, and thus of eLAMI, with real acquired values; the combination of *i)* and *ii)* leads to state the validity of the simulator implementation.

Starting from *(i)*, a comparison between the values obtained in the real and simulated cases is shown in Figure 4.15, in terms of variability ranges. In this figure, the behaviour of V_{RMS} (4.15.(a), I_{RMS} (4.15.(b), P (4.15.(c) and S (4.15.d) are reported, for each individual considered load and its corresponding aggregate.

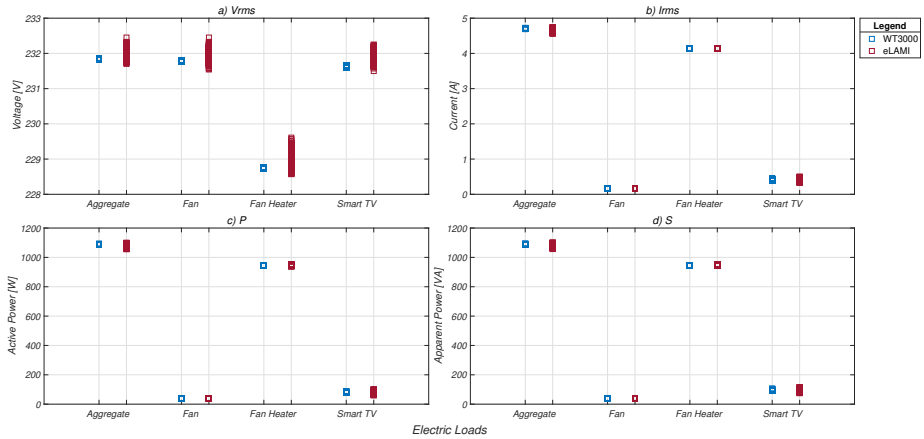


Figure 4.15: Comparison between WT3000 and eLAMI for devices: *Fan*, *Fan Heater*, *Smart TV* and *Aggregate*. Comparison made in terms of features: (a) Voltage RMS (b) Current RMS (c) Active Power (d) Apparent Power

In this case, the variability ranges are overlapped, although WT3000's related range is almost always narrower than the simulated one. This is because the WT3000 has a higher accuracy level than what can be obtained by adopting the set-up used in the acquired reference profiles for simulation. In any case, since WT3000 has been chosen as a reference instrument, it is expected that it can exhibit a far better metrological performance. Furthermore, the reference profiles for the generation of eLAMI were constructed to take into account the variability of the data over a time horizon longer than 1 hour (total test duration). Of course, increasing the acquisition time would tend to increase the variation intervals of the WT3000 distributions, due to measurand variability.

An interesting aspect, that can be seen in this figure looking at the WT3000 measured values, is the behaviour of the V_{RMS} (Figure 4.15(a)). The 3 loads are simultaneously supplied by the same power source, each through its own power line: such a setting can cause a potential voltage drop. As reported in Figure

4.15(c), the *Fan Heater* is the load with the highest absorption: consequently, the V_{RMS} at its ends is the lowest (Figure 4.15(a)). Conversely, the WT3000 records the highest voltage at the ends of the *"Fan"*, which is the closest to the aggregate's one, i.e. the power source. Looking at the voltage behavior of eLAMI, the same trend can be observed.

To demonstrate *(ii)*, only the mean value and standard deviation of a few monitored Features for the *Fan* load are reported, for sake of brevity, in Table 4.8. In particular, the considered features are: V_{rms}, I_{rms}, P and S.

The standard deviation values of the measurements recorded by the WT3000, as we expected, are much smaller than those related to eLAMI, due to the simulator design parameters, which had the purpose to replicate a typical commercial smart meter less accurate than the adopted reference (WT3000). Nevertheless, from a measurement point of view, the intervals (μ-σ, μ-σ) belonging to WT3000 and eLAMI are generally overlapped, demonstrating the validity of the generated dataset.

Table 4.8: Comparison of mean and standard deviation values obtained from WT3000 and eLAMI for the electrical load *Fan*. Considered features: V_{rms}, I_{rms}, P and S

Feature		**WT3000**	**eLAMI**
V_{rms} [V]	μ	231.68	231.94
	σ	0.13	0.59
I_{rms} [mA]	μ	159.90	161.30
	σ	0.58	1.40
P [W]	μ	36.38	37.12
	σ	0.22	0.37
S [VA]	μ	36.82	37.63
	σ	0.31	0.32

The validity of the algorithms implemented in the simulator for the generation of eLAMI is evident when analyzing the values and behaviors obtained from the features analyzed in Figure 4.15 and Table 4.8. Furthermore, the similarity between the behaviors of the *Aggregate* highlights the consistency of the process implemented in the simulator.

Descriptions of the general characteristics of eLAMI

As highlighted above, one of the peculiarities of eLAMI is the variability of the data, both in terms of operating states of the monitored devices and consumption habits. Figure 4.16 shows the average monthly active energy consumption profiles of the aggregate load, for the 24 hours of the day (x-axis), for each month. In particular, in terms of active energy consumption (y-axis), the curves show: in green, the average trend, in red the maximum reached for each hourly interval of the month considered, and similarly in blue the minimum. First of all, when analyzing the individual month, we can see the variability of the absorption curve during the 24 hours of the day, consistent with what happens in the residential area. In particular, the curve shows an increase in the early morning hours followed by a rapid decrease until midday when the second absorption peak occurs. A further decrease follows this in consumption before arriving at the evening hours characterized by the highest energy absorption.

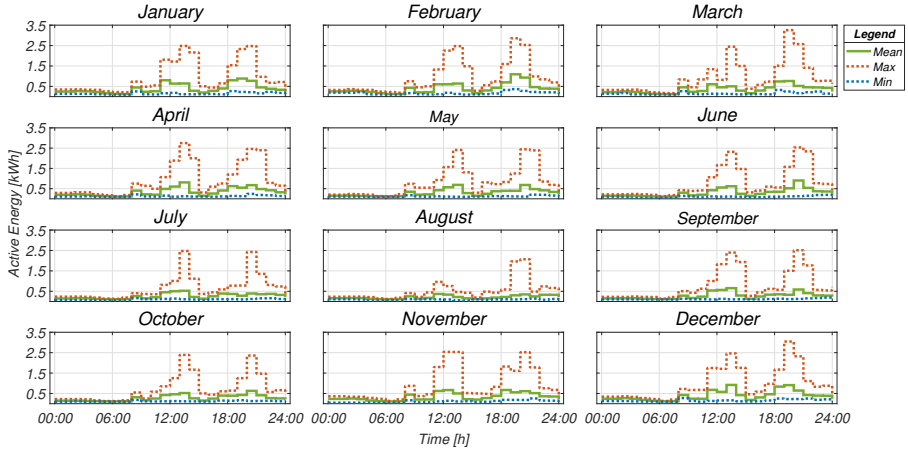


Figure 4.16: Average monthly active energy consumption profiles of the aggregate load

In addition to the variability during the day, by comparing the different months, we can value the seasonality of consumption and thus the variation in electrical-behavioral habits. In particular, consumption is higher during the winter months than in the summer months, which is particularly evident when comparing August and December. This is because in the winter months, according to defined habits, there is greater use of certain high-consumption devices, such as *Boiler*, *Electric Oven* and *Microwave*. Furthermore, it should be noted that during the winter

months lamp utilization is higher than in the summer months, which has an impact on the consumption peaks mentioned above.

A further interesting aspect is a non-zero consumption during nighttime hours present in all months, due to the presence of some devices in standby mode, characterized by minimal but not zero power consumption. This ceiling does not show much variability in terms of consumption, as the devices on stand-by during the night are almost always the same, so the 3 curves (average, minimum and maximum) almost overlap, with a consumption of less than 0.5 kWh.

In Figure 4.17 the total electricity consumption for each month of the simulated year is shown. In this case, the seasonality of consumption and thus the variation of the energy absorbed in the different months is particularly evident. Since there is no cooling system, total consumption is higher in autumn and winter than in spring and summer. In particular, starting the year in January, electricity consumption is high and remains more or less constant until March, and then begins to decrease in April with the arrival of spring. The lowest peak is reached in August and then starts to rise again from September forward. The highest electricity consumption is recorded in December, while the lowest is recorded in August in perfect analogy with what is shown in Figure 4.16.

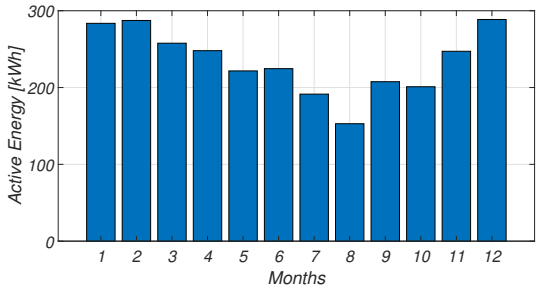


Figure 4.17: Aggregate active energy load curve per months

In Figure 4.18 are reported the average daily consumption of 4 electrical loads for each month of eLAMI (in terms of average, maximum and minimum daily consumption), taken as an example, to show the variation in consumption patterns in eLAMI. Specifically, the devices are: *Boiler* (4.18(a), *Smartphone Charger* (4.18(b), *Fan* (4.18.(c), *Fan Heater* (4.18(d). Analyzing *Boiler* consumption (4.18(a), it can be seen that the average consumption in winter is higher than in summer, where it is used only for hot water and not for heating. In contrast, the *Fan Heater* (4.18(d) is only used in winter, from October to April, peaking in February. The opposite behavior is obtained by analyzing the *Fan* (**??**(c), which is only used in the summer

months, from June to September, with a peak in August. Unlike the others, the *Smartphone Charger* (4.18(b) does not show substantial variations in consumption between months. This is because it is used on average every day of the year in the same way.

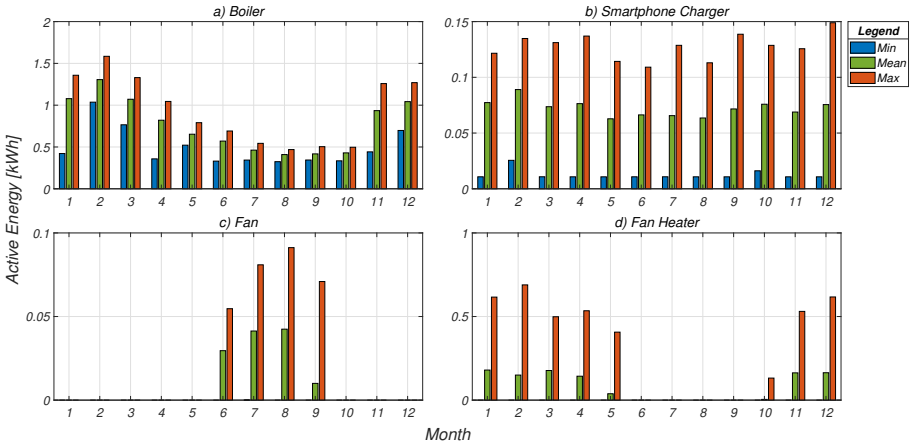


Figure 4.18: Seasonality example of some different electrical loads

Smart energy application examples: load profiling

Machine Learning and Artificial Intelligence techniques, in general, are based on the use of large amounts of input data. However, if these techniques have input data that do not correctly describe the phenomenon to be studied, the output may be far from the desired result. This is why feature selection algorithms are very often used to find the best set of features to build useful and robust models of the phenomena studied [103].

In Figure 4.19(a) the active power absorbed by the *Desk Lamp* in January eLAMI is reported as a function of the corresponding assumed states. As previously verified, state variability is present. Consequently, the active power P alone is not able to discriminate the 4 different load operating state because states 1 and 2, and similarly 3 and 4, overlap in terms of P. Therefore, in terms of load profiling, other features must be found for the correct identification of operating states. For example, the active power P as a function of the power factor at fundamental is reported in Figure 4.19(b). This feature is able to discriminate states 1 and 2 better than P alone, while states 3 and 4 still remain indistinguishable. Conversely, in Figure 4.19(c) we see the phase of the 6th harmonic voltage group identify states

3 and 4 well but not the first two. Combining the two features identified, power factor at fundamental and phase of the 6th harmonic voltage group, Figure 4.19(d) shows an optimal situation where 4 operating states of the load (cluster) considered are clearly visible. It is therefore very clear how the greater number of electrical parameters in eLAMI results in a better representation and distinction between the different electrical signatures of the individual load.

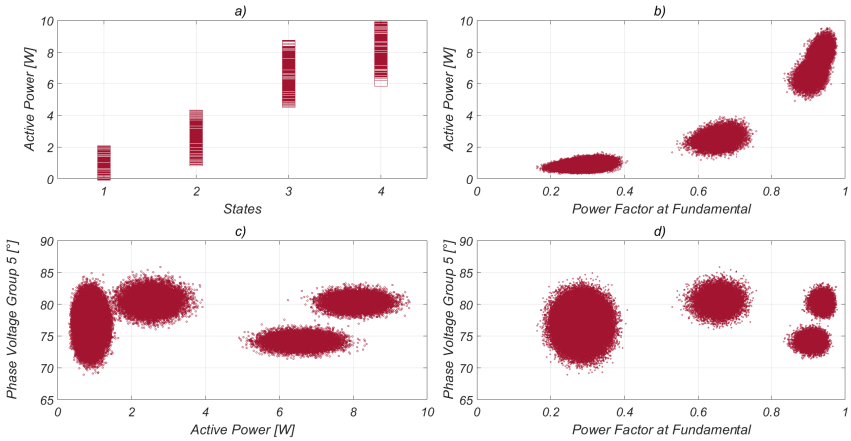


Figure 4.19: Example of load profiling application for desk lamp - (a) Power consumption per state (b) Active power as a function of power factor at 50 Hz (c) Phase of 5th voltage harmonic group as a function of active power (d) Phase of 5th voltage harmonic group as a function of power factor at 50 Hz

Smart energy application examples: NILM

In this section is reported an example of application in the NILM (Non-intrusive Load Monitoring) field. NILM is presented as a time series classification problem where the objective is to detect which appliances are active at a given instant and how much each of them contributes to the total percentage of consumption. Due to their advantages, techniques based on the analysis of steady-state features are the most widely used, typically referring to active power only [67]. This feature, however, is not always able to distinguish devices that absorb similar power or have similar operating principles.

In Figure 4.20(a) are reported the total active power obtained from an aggregation of 3 loads present in eLAMI and in Figure 4.20(b) the individual active powers absorbed by the 3 considered loads, are reported. In particular, in Figure 4.20(a)

and Figure 4.20(b) the active power in time, both for aggregate and some example of single load, are reported. Conversely, Figure 4.21(a) and Figure 4.21(b) show the RMS values of the 6th harmonic current group in time, both for the individual loads considered above and for the corresponding aggregate.

It is evident when analyzing the aggregate active power in Figure 4.20(a) and the single active power in Figure 4.21(b), that the 3 loads are indistinguishable due to the problems mentioned above. This represents a critical case for NILM algorithms. Instead, analyzing the current harmonics of 6th group in Figure 4.21(a) for the aggregate and in Figure 4.21(b) for every single load, three different levels of absorption are present, allowing for correct identification of the active loads.

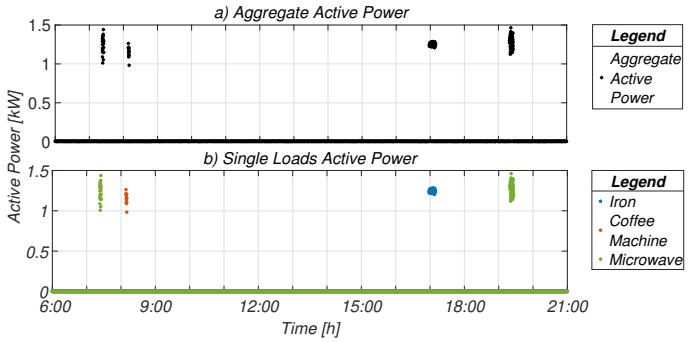


Figure 4.20: Active power in time: (a) Aggregate (b) Single Loads

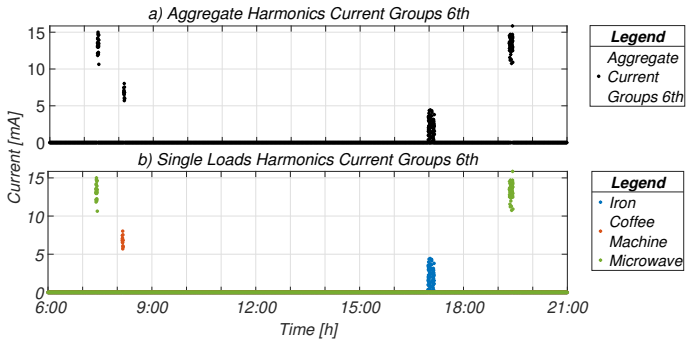


Figure 4.21: Current harmonics of 6th group in time: (a) Aggregate (b) Single Loads

Smart energy application examples: forecasting

In the world of Smart Energy, statistical and forecasting analyses based on time series are often carried out. In particular, one of the goals of an Energy Management System is to create mathematical models that can simulate trends in electricity consumption as a function of various factors. Furthermore, through statistical analysis, it is possible to define statistical and/or performance indices of the analyzed system. Some of the benefits of modeling analyzed electricity consumption are: *i)* construction of past seasonal trends and consequently of future ones, *ii)* definition of energy efficiency and optimization plans, *iii)* forecast balancing of electricity networks and performance verification.

To this end, eLAMI also offers the possibility of testing forecasting and modeling algorithms for electrical systems. For example, in Figure 4.22 based on the knowledge of the first 10 months of the year (300 days) relating to the power consumption trend of the total aggregate, a consumption forecast was made for the last two months of the year. The mathematical model derived is based on a fitting of the input data. Using the mathematical model, a band (*2*DevStd* width) was derived within which the consumption for the 60 forecast days is estimated. As can be seen from this figure, the real data falls within the obtained forecast band with an error of approximately 6.6 %, i.e. 56 days out of 60 estimated correctly.

Furthermore, in diagnostic and predictive terms, thanks to the analysis of time series of data, it is possible to estimate the operating ranges of electrical loads in order to assess and/or predict any decay in their performance and any drift towards fault states.

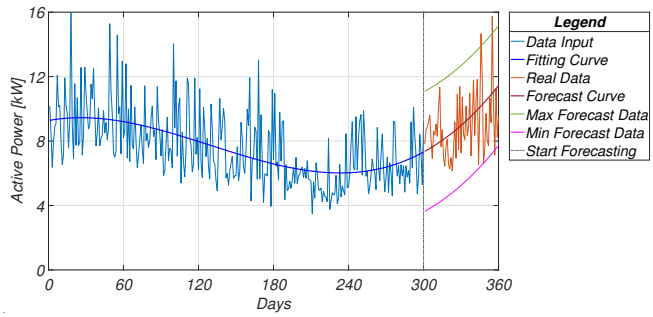


Figure 4.22: Example of forecasting for electric consumption with eLAMI

4.2.4 Conclusions

A novel approach to provide a simulated electrical energy dataset, from the reference signal acquisition to the data validation has been reported. To enforce motivations leading to its building and to prove its suitability for Smart Energy applications, a final section regarding examples of Smart Energy profiling and management is also discussed. The output data, composed of more than 400 electrical parameters and reporting one-year period energy profile simulation of a residential building, are made available for download to enhance research in Smart Energy sector with novel, detailed, validated and wide-applicable data. The acquisition setup has been chosen according to typical metering capabilities of currently adopted home smart meters. Voltage and Current signals, produced for 36 home appliances, have been processed both in time and frequency domain, to provide a comprehensive set of electrical parameters composing the electrical signature of each considered appliance. To be as close as possible to the real scenario, stochastic models have been also implemented to obtain consumption habits to manage state transitions for each load. In its current status, only nominal operating conditions have been considered, i.e. no failures have been hypothesized during the simulation interval.

Conclusions and future developments

The process of assessing resilience in the Italian electricity grid involved all the actors that are part of the grid, starting from the energy transmission network, up to the electricity distribution network and the end users, such as industries and households. Ongoing climate change means that resilience is the cornerstone of the new electricity grid, which is evolving into a much more complex system than its predecessor. From a scientific point of view, and not only that, these issues are of great interest, given the common challenge that awaits us in the coming years, to leave future generations an electricity system that is increasingly able to cope with the current climate change and to evolve more and more, integrating renewable and green energy sources. In this thesis, new methodologies have been proposed and developed for assessing the resilience of electricity grid planning, starting from transmission, to the resilience of smart appliances in homes through diagnostics, and ending with the assessment of the change that is affecting the grid with the integration of renewable sources causing operational resilience issues such as voltage stability and secondary substation diagnostics.

In a first phase, the work is focused on the resilience of smart appliances in the home, with the aim of diagnosing possible new operating states that would indicate a possible impending equipment failure. In order to carry out evaluations on large datasets, given the lack of a large datasets in the literature, a simulator was developed that could simulate the electrical signature of a large number of loads, in order to then be able to analyze their diagnostics with evolutionary algorithms. The future development of this topic includes the extension of these analyses to the industrial environment, which is certainly prone to many faults and where production downtimes cause huge amounts of economic losses for companies.

Diagnostics is not only important from a domestic or industrial point of view, but also in the power grid. For this reason, the impacts of disturbance phenomena, such as stray magnetic fields, within MV/LV substations that can distort current

measurement and lead to incorrect monitoring of the electrical distribution network were analyzed. In fact, depending on the accuracy of the sensor used and its installation in terms of positioning inside the cabin, the measurement will be more or less impacted by external phenomena such as magnetic fields created by the busbars adjacent to the one to be monitored, altering the measurement. The device used for monitoring is a Rogowski coil, which, in combination with the T-PMR, allows the cabin to be monitored.

In a future perspective, the T-PMR could have a dual function, in addition to monitoring the substation and the portion of the grid to which it belongs, it could also implement voltage control algorithms. For example, the distributed online algorithm for voltage control is affected by different responses if the accuracy of the voltage measurement changes, requiring the injection of more or less reactive into the network depending on the accuracy of the measurement. By exploiting the T-PMR, which has a very good accuracy for voltage measurement, we could increase the number of devices in the network from which the measurements come (not only from PMUs) but also increase the accuracy in certain cases. The problem of voltage regulation will be increasingly important in the electricity grid of the future, given the large penetration of renewable energy sources, which will cause more voltage instability. It therefore becomes essential to address the issue of quality of service.

The grid penetration of renewable energy sources will continue to grow as it will lower CO_2 emissions caused by electricity production and combat climate change. In fact, climate change is affecting the whole world, also affecting the electricity transmission grid infrastructure. It is therefore crucial to have a grid that is as resilient as possible and ready to deal with increasingly frequent threats such as high winds and the formation of snow-ice sleeves. With this in mind, the work carried out focused on mapping tree interference with the transmission grid, proposing not an approach based on databases using land-use information but one based on LiDar surveys. This made it possible to have a more precise and timely mapping, which would allow effective action to be taken where, outside the subdivision zone, vegetation would create problems of tipping over the power line due to strong winds. With regard to ice-sleeve formation, a new device has been proposed to prevent the sleeve formation from decreasing the dielectric distance between conductors and thus the fault on that line. Thanks to this device, the conductors will not sag under the weight of the sleeve but will remain stationary in their position, thus avoiding the reduction in dielectric distance. Furthermore, ongoing climate change is causing problems with floods and landslides, in a future perspective the Resilience 2.0 model could be extended to assess threats impacting primary cabin floods or landslides.

Bibliography

[1] Mathaios Panteli and Pierluigi Mancarella. "Influence of extreme weather and climate change on the resilience of power systems: Impacts and possible mitigation strategies". In: *Electric Power Systems Research* 127 (2015), pp. 259–270.

[2] E. Ciapessoni et al. "A methodology to compute resilience indicators for the Italian Transmission System". In: *Proc. of CIGRE 2021 Centennial Session.* 2021, pp. 1–11.

[3] E. Ciapessoni et al. "Validation and application of the methodology to compute resilience indicators in the Italian EHV Transmission System". In: *Proc. of 2022 CIGRE Session.* 2022, pp. 1–14.

[4] ARERA. *Deliberation 9/2022/R/EEL.* Verifica di conformità del codice di trasmissione, dispacciamento, sviluppo e sicurezza della rete, in materia di valutazione dell'incremento di resilienza di progetti di sviluppo della rete.

[5] Paola Faggian and Goffredo Decimi. "An updated investigation about climate-change hazards that might impact electric infrastructures". In: *2019 AEIT International Annual Conference (AEIT).* IEEE. 2019, pp. 1–5.

[6] Jennifer E Kay et al. "The Community Earth System Model (CESM) large ensemble project: A community resource for studying climate change in the presence of internal climate variability". In: *Bulletin of the American Meteorological Society* 96.8 (2015), pp. 1333–1349.

[7] Daniela Jacob et al. "EURO-CORDEX: new high-resolution climate change projections for European impact research". In: *Regional environmental change* 14 (2014), pp. 563–578.

[8] Riccardo Bonanno, Matteo Lacavalla, and Simone Sperati. "A new high-resolution meteorological reanalysis Italian dataset: MERIDA". In: *Quarterly Journal of the Royal Meteorological Society* 145.721 (2019), pp. 1756–1779.

[9] CEI. *CEI 64-8.* `https://mycatalogo.ceinorme.it/book/item/00M000229?sso=y`. Online; Accessed:08.03.2022. 2022.

[10] CEI. *Std 11-4*. Norme tecniche per la costruzione di linee elettriche aeree esterne.

[11] E Ciapessoni et al. "Modeling the overhead line vulnerability to combined wind and snow loads for resilience assessment studies". In: *2021 IEEE Madrid PowerTech*. IEEE. 2021, pp. 1–6.

[12] Emanuele Ciapessoni et al. "Modelling the vulnerability of overhead lines against tree contacts for resilience assessment". In: *2020 International Conference on Probabilistic Methods Applied to Power Systems (PMAPS)*. IEEE. 2020, pp. 1–6.

[13] CORINE. *CORINE Database*. `https://land.copernicus.eu/pan-european/CORINE-land-cover/`.

[14] DW Wanik et al. "Using vegetation management and LiDAR-derived tree height data to improve outage predictions for electric utilities". In: *Electric Power Systems Research* 146 (2017), pp. 236–245.

[15] Jupiter. *Jupiter Intelligence website*. `https://jupiterintel.com`.

[16] IEC. *Std. IEC 60826*. Overhead transmission lines – Design criteria", Edition no. 4,

[17] Roger B Nelsen. "Archimedean copulas". In: *An introduction to copulas* (2006), pp. 109–155.

[18] ENTOS-E. *Std. IEC 60826*. Winter Outlook 2022-2023.

[19] Tatjana Dokic and Mladen Kezunovic. "Predictive risk management for dynamic tree trimming scheduling for distribution networks". In: *IEEE Transactions on Smart Grid* 10.5 (2018), pp. 4776–4785.

[20] Copernicus. *Copernicus project website*. `https://land.copernicus.eu/`.

[21] Emanuele Ciapessoni et al. "An Innovative Tree Interference Mapping With LiDar for Overhead Lines Vulnerability Assessment in the Italian Power System". In: *2023 AEIT International Annual Conference (AEIT)*. 2023, pp. 1–6. DOI: `10.23919/AEIT60520.2023.10330326`.

[22] Andrea Pitto et al. "Comprehensive risk based methodology and tool for a quantitative resilience assessment of distribution and transmission systems". In: (2019).

[23] Jingwei Xu et al. "Wet snow flashover characteristics of the insulator strings in "Λ "Shape on 500 kV transmission lines". In: *2018 12th International Conference on the Properties and Applications of Dielectric Materials (ICPADM)*. IEEE. 2018, pp. 1131–1134.

[24] László E Kollár, Masoud Farzaneh, and Pierre Van Dyke. "Modeling ice shedding propagation on transmission lines with or without interphase spacers". In: *IEEE Transactions on Power Delivery* 28.1 (2012), pp. 261–267.

[25] Fujiang Cui et al. "Study on the influence of interphase spacers on ice shedding of three-phase iced eight-bundled transmission lines". In: *Cold Regions Science and Technology* 174 (2020), p. 103043.

[26] International Organization for Standardization. *Atmospheric icing of structures*. ISO, 2017.

[27] SCB Cigre and Task Force. "State of the art of conductor galloping". In: *Electra* 322 (2007).

[28] Overhead Electrical Lines Exceeding AC. "kV–Part 1: General requirements–Common Specifications". In: *DS/EN* (2013), pp. 50341–1.

[29] Hisato Matsumiya et al. "Field observation of wet snow accretion and galloping on a single conductor transmission line". In: *Proceedings of International workshop on Atmospheric Icing of Structures. Reykjavik, Iceland*. 2019.

[30] E. Ciapessoni, D. Cirio, A. Pitto, S. Casulli, F. Falorni, F. Scavo. *Assessing the vulnerability of overhead line wires to flashovers due to reduced insulation distances for power system resilience studies*. accepted at IEEE ISGT EU Conference, Grenoble, Oct 2023, pp. 1-5.

[31] Chuan Wu et al. "A method to calculate jump height of iced transmission lines after ice-shedding". In: *Cold Regions Science and Technology* 125 (2016), pp. 40–47.

[32] Xiaoming Rui et al. "Dynamic response of overhead transmission lines with eccentric ice deposits following shock loads". In: *IEEE Transactions on Power Delivery* 32.3 (2015), pp. 1287–1294.

[33] Emanuele Ciapessoni et al. "An analytical model to quantify the technical benefits of interphase spacers to increase power system resilience against wet snow: the Italian case". In: *2023 AEIT International Annual Conference (AEIT)*. 2023, pp. 1–6. DOI: 10.23919/AEIT60520.2023.10330309.

[34] Emanuele Ciapessoni et al. "A capital light solution to increase power system resilience against wet snow: the Italian experience with anti-torsional devices". In: *2022 AEIT International Annual Conference (AEIT)*. IEEE. 2022, pp. 1–6.

[35] Mohammad Hamed Samimi et al. "The Rogowski coil principles and applications: A review". In: *IEEE Sensors Journal* 15.2 (2014), pp. 651–658.

[36] Zhenhua Li et al. "An improved digital integral algorithm to enhance the measurement accuracy of Rogowski coil-based electronic transformers". In: *International Journal of Electrical Power & Energy Systems* 118 (2020), p. 105806.

[37] John P Barber. "The use of rogowski coils in current measurement". In: *2014 17th International Symposium on Electromagnetic Launch Technology*. IEEE. 2014, pp. 1–4.

[38] William H Raymond and Arthur Garder. "A review of recursive and implicit filters". In: *Monthly weather review* 119.2 (1991), pp. 477–495.

[39] *T-PMR*. URL: https://www.tesmec.com/it/automation/prodotti/protection-monitoring/t-pmr-rele-di-protezione-e-misura.

[40] *IEC 61869-10*. URL: https://webstore.iec.ch/publication/27276.

[41] *IEC 61869-6*. URL: https://webstore.iec.ch/publication/24662.

[42] *Pacific*. URL: https://pacificpower.com/.

[43] *Tektronix A621*. URL: https://www.tek.com/en/datasheet/current-probes.

[44] *TiePie HS5*. URL: https://www.tiepie.com/en/usb-oscilloscope/handyscope-hs5.

[45] Carlo Masetti. "Revision of European Standard EN 50160 on power quality: Reasons and solutions". In: *Proceedings of 14th International Conference on Harmonics and Quality of Power-ICHQP 2010*. IEEE. 2010, pp. 1–7.

[46] Cheng Gao and MA Redfern. "A review of voltage control in smart grid and smart metering technologies on distribution networks". In: *2011 46th International Universities' Power Engineering Conference (UPEC)*. VDE. 2011, pp. 1–5.

[47] P Raghavendra and DN Gaonkar. "Online voltage estimation and control for smart distribution networks". In: *Journal of Modern Power Systems and Clean Energy* 4.1 (2016), pp. 40–46.

[48] Urban Kuhar et al. "The impact of model and measurement uncertainties on a state estimation in three-phase distribution networks". In: *IEEE Transactions on Smart Grid* 10.3 (2018), pp. 3301–3310.

[49] Carlo Muscas et al. "Effects of measurements and pseudomeasurements correlation in distribution system state estimation". In: *IEEE Transactions on Instrumentation and Measurement* 63.12 (2014), pp. 2813–2823.

[50] Carlo Muscas et al. "Uncertainty of voltage profile in PMU-based distribution system state estimation". In: *IEEE Transactions on Instrumentation and Measurement* 65.5 (2015), pp. 988–998.

[51] Marco Pau et al. "Impact of uncertainty sources on the voltage control of active distribution grids". In: *2021 International Conference on Smart Energy Systems and Technologies (SEST)*. IEEE. 2021, pp. 1–6.

[52] Saverio Bolognani et al. "On the need for communication for voltage regulation of power distribution grids". In: *IEEE Transactions on Control of Network Systems* 6.3 (2019), pp. 1111–1123.

[53] Edoardo De Din et al. "Implementation of the online distributed voltage control based on containers". In: *2022 International Conference on Smart Energy Systems and Technologies (SEST)*. IEEE. 2022, pp. 1–6.

[54] *DMU*. URL: https://git.rwth-aachen.de/acs/public/automation/modules/dmu.git.

[55] Nexus. *Nexus 1500+ Datasheet*. https://www.electroind.com/products/nexus-1500-power-quality-meter-with-phasor-measurement-unit/.

[56] Siemens. *Siemens SIMEAS R-PMU Datasheet*. https://www.manualslib.com/manual/2375089/Siemens-Simeas-R-Pmu.html.

[57] ABB. *ABB RES70 Datasheet*. https://library.e.abb.com/public/f1431c491f6c4826bbf1ebb709534a4a/1MRK511317-UEN_B_en_Technical_manual__Phasor_measurement_unit_RES670_2.0__IEC.pdf.

[58] Christoph Klemenjak and Peter Goldsborough. "Non-intrusive load monitoring: A review and outlook". In: *arXiv preprint arXiv:1610.01191* (2016).

[59] Marcantonio Catelani et al. "Optimizing maintenance policies for a yaw system using reliability-centered maintenance and data-driven condition monitoring". In: *IEEE Transactions on Instrumentation and Measurement* 69.9 (2020), pp. 6241–6249.

[60] Domenico Capriglione et al. "Real-time implementation of an IFD scheme for motorcycle sensors". In: *2018 IEEE International Instrumentation and Measurement Technology Conference (I2MTC)*. IEEE. 2018, pp. 1–6.

[61] Domenico Capriglione et al. "Online fault detection of rear stroke suspension sensor in motorcycle". In: *IEEE Transactions on Instrumentation and Measurement* 68.5 (2019), pp. 1362–1372.

[62] Domenico Capriglione et al. "Soft Sensors for Instrument Fault Accommodation in Semiactive Motorcycle Suspension Systems". In: *IEEE Transactions on Instrumentation and Measurement* 69.5 (2020), pp. 2367–2376.

[63] Hyungsul Kim et al. "Unsupervised disaggregation of low frequency power measurements". In: *Proceedings of the 2011 SIAM international conference on data mining*. SIAM. 2011, pp. 747–758.

[64] J Zico Kolter and Tommi Jaakkola. "Approximate inference in additive factorial hmms with application to energy disaggregation". In: *Artificial intelligence and statistics*. PMLR. 2012, pp. 1472–1482.

[65] Stephen Makonin et al. "Exploiting HMM sparsity to perform online real-time nonintrusive load monitoring". In: *IEEE Transactions on smart grid* 7.6 (2015), pp. 2575–2585.

[66] Oliver Parson et al. "Non-intrusive load monitoring using prior models of general appliance types". In: *Proceedings of the AAAI Conference on Artificial Intelligence*. Vol. 26. 1. 2012.

[67] George William Hart. "Nonintrusive appliance load monitoring". In: *Proceedings of the IEEE* 80.12 (1992), pp. 1870–1891.

[68] Ram Machlev et al. "MO-NILM: A multi-objective evolutionary algorithm for NILM classification". In: *Energy and Buildings* 199 (2019), pp. 134–144.

[69] Vladimir Stankovic, Jing Liao, and Lina Stankovic. "A graph-based signal processing approach for low-rate energy disaggregation". In: *2014 IEEE symposium on computational intelligence for engineering solutions (CIES)*. IEEE. 2014, pp. 81–87.

[70] Bochao Zhao, Lina Stankovic, and Vladimir Stankovic. "On a training-less solution for non-intrusive appliance load monitoring using graph signal processing". In: *IEEE Access* 4 (2016), pp. 1784–1799.

[71] Pedro Paulo Marques do Nascimento. "Applications of deep learning techniques on NILM". In: *Diss. Universidade Federal do Rio de Janeiro* (2016).

[72] Jack Kelly and William Knottenbelt. "Neural nilm: Deep neural networks applied to energy disaggregation". In: *Proceedings of the 2nd ACM international conference on embedded systems for energy-efficient built environments*. 2015, pp. 55–64.

[73] CENELEC. *CENELEC EN 50470-1 : Electricity metering equipment (a.c.) Part 1: General requirements, tests and test conditions - Metering equipment (class indexes A, B and C)*. Oct. 2006.

[74] Anthony Faustine et al. "A survey on non-intrusive load monitoring methodies and techniques for energy disaggregation problem". In: *arXiv preprint arXiv:1703.00785* (2017).

[75] Nipun Batra et al. "NILMTK: An open source toolkit for non-intrusive load monitoring". In: *Proceedings of the 5th international conference on Future energy systems*. 2014, pp. 265–276.

[76] Jack Kelly et al. "Nilmtk v0. 2: a non-intrusive load monitoring toolkit for large scale data sets: demo abstract". In: *Proceedings of the 1st ACM Conference on Embedded Systems for Energy-efficient Buildings*. 2014, pp. 182–183.

[77] Barbara Cannas et al. "NILM techniques applied to a real-time monitoring system of the electricity consumption". In: *ACTA IMEKO* 10.2 (2021), pp. 139–146.

[78] CE. *Directive 2006/32/EC of the European Parliament And of the Council*. `https://eur-lex.europa.eu/legal-content/IT/TXT/PDF/?uri=CELEX:32006L0032&from=LV`. Online; Accessed:14.03.2022. 2022.

[79] CE. *Directive 2009/72/EC of the European Parliament And of the Council*. `https://eur-lex.europa.eu/legal-content/EN/TXT/PDF/?uri=CELEX:32009L0072&from=EN`. Online; Accessed:14.03.2022. 2022.

[80] CE. *Directive 2012/27/CE of the European Parliament And of the Council*. `https://eur-lex.europa.eu/legal-content/EN/TXT/PDF/?uri=CELEX:32012L0027&from=IT`. Online; Accessed:14.03.2022. 2022.

[81] Stephen Makonin et al. "AMPds: A public dataset for load disaggregation and eco-feedback research". In: *2013 IEEE electrical power & energy conference*. IEEE. 2013, pp. 1–6.

[82] Stephen Makonin et al. "Electricity, water, and natural gas consumption of a residential house in Canada from 2012 to 2014". In: *Scientific data* 3.1 (2016), pp. 1–12.

[83] Adrian Filip et al. "Blued: A fully labeled public dataset for event-based nonintrusive load monitoring research". In: *2nd workshop on data mining applications in sustainability (SustKDD)*. Vol. 2012. 2011.

[84] Oliver Parson et al. "Dataport and NILMTK: A building data set designed for non-intrusive load monitoring". In: *2015 ieee global conference on signal and information processing (globalsip)*. IEEE. 2015, pp. 210–214.

[85] Akshay SN Uttama Nambi, Antonio Reyes Lua, and Venkatesha R Prasad. "Loced: Location-aware energy disaggregation framework". In: *Proceedings of the 2nd acm international conference on embedded systems for energy-efficient built environments*. 2015, pp. 45–54.

[86] Christian Beckel et al. "The ECO data set and the performance of non-intrusive load monitoring algorithms". In: *Proceedings of the 1st ACM conference on embedded systems for energy-efficient buildings*. 2014, pp. 80–89.

[87] Changho Shin et al. "The ENERTALK dataset, 15 Hz electricity consumption data from 22 houses in Korea". In: *Scientific data* 6.1 (2019), pp. 1–13.

[88] Nipun Batra et al. "It's Different: Insights into home energy consumption in India". In: *Proceedings of the 5th ACM Workshop on Embedded Systems For Energy-Efficient Buildings*. 2013, pp. 1–8.

[89] J Zico Kolter and Matthew J Johnson. "REDD: A public data set for energy disaggregation research". In: *Workshop on data mining applications in sustainability (SIGKDD), San Diego, CA*. Vol. 25. Citeseer. 2011, pp. 59–62.

[90] David Murray, Lina Stankovic, and Vladimir Stankovic. "An electrical load measurements dataset of United Kingdom households from a two-year longitudinal study". In: *Scientific data* 4.1 (2017), pp. 1–12.

[91] Jack Kelly and William Knottenbelt. "The UK-DALE dataset, domestic appliance-level electricity demand and whole-house demand from five UK homes". In: *Scientific data* 2.1 (2015), pp. 1–14.

[92] Nadezda Buneeva and Andreas Reinhardt. "AMBAL: Realistic load signature generation for load disaggregation performance evaluation". In: *2017 ieee international conference on smart grid communications (smartgridcomm)*. IEEE. 2017, pp. 443–448.

[93] Simon Henriet et al. “A generative model for non-intrusive load monitoring in commercial buildings”. In: *Energy and Buildings* 177 (2018), pp. 268–278.

[94] Dong Chen, David Irwin, and Prashant Shenoy. “Smartsim: A device-accurate smart home simulator for energy analytics”. In: *2016 IEEE International Conference on Smart Grid Communications (SmartGridComm)*. IEEE. 2016, pp. 686–692.

[95] Christoph Klemenjak et al. “A synthetic energy dataset for non-intrusive load monitoring in households”. In: *Scientific Data* 7.1 (2020), pp. 1–17.

[96] G Berrettoni et al. “Preliminary Sensitivity Analysis of Combinatorial Optimization (CO) for NILM Applications: Effect of the Meter Accuracy”. In: *2021 IEEE 6th International Forum on Research and Technology for Society and Industry (RTSI)*. IEEE. 2021, pp. 486–490.

[97] Tektronix. *TCP202 DC Coupled Current Probe*. `https://download.tek.com/datasheet/TCP202_Current_Probe_Datasheet_51W-10736-7.pdf`. Online; Accessed:02.02.2022. 2022.

[98] Tektronix. *Probe Power Supply 1103*. `https://download.tek.com/datasheet/1103_Probe_Power_Supply_Datasheet_60W-14843-1_2.pdf`. Online; Accessed:02.02.2022. 2022.

[99] Tektronix. *High Voltage Differential Probes*. `https://download.tek.com/manual/P5200A-High-Voltage-Differential-Probe-Instruction-Manual-077053602.pdf`. Online; Accessed:02.02.2022. 2022.

[100] IEC. *IEC 61000-4-7*. `https://webstore.iec.ch/publication/4228`. Online; Accessed:07.02.2022. 2022.

[101] Tari Luca et al. “elami—an innovative simulated dataset of electrical loads for advanced smart energy applications”. In: *IEEE Access* 10 (2022), pp. 91177–91191.

[102] Yokogawwa. *WT3000 Yokogawa*. `https://tmi.yokogawa.com/solutions/discontinued/wt3000-precision-power-analyzer/`.

[103] Jiliang Tang, Salem Alelyani, and Huan Liu. “Feature selection for classification: A review”. English (US). In: *Data Classification*. Publisher Copyright: © 2015 by Taylor & Francis Group, LLC. CRC Press, Jan. 2014, pp. 37–64. ISBN: 9781466586741. DOI: `10.1201/b17320`.